**The Pennsylvania State University
APPLIED RESEARCH LABORATORY
P. O. Box 30
State College, PA 16804**

A 1:8.7 SCALE WATER TUNNEL VERIFICATION & VALIDATION TEST OF AN AXIAL FLOW WATER TURBINE

By

Arnold A. Fontaine, William A. Straka, Richard S. Meyer, and Michael L. Jonson

Technical Report No. TR 13-002
August 2013

Distribution Statement A: Approved for public release; distribution unlimited

REPORT DOCUMENTATION PAGE

The public reporting burden for this collection of information is estimated to average 1 hour per response, including the time for reviewing instructions, searching existing data sources, gathering and maintaining the data needed, and completing and reviewing the collection of information. Send comments regarding this burden estimate or any other aspect of this collection of information, including suggestions for reducing the burden, to Department of Defense, Washington Headquarters Services, Directorate for Information Operations and Reports (0704-0188), 1215 Jefferson Davis Highway, Suite 1204, Arlington, VA 22202-4302. Respondents should be aware that notwithstanding any other provision of law, no person shall be subject to any penalty for failing to comply with a collection of information if it does not display a currently valid OMB control number. **PLEASE DO NOT RETURN YOUR FORM TO THE ABOVE ADDRESS.**

1. REPORT DATE (DD-MM-YYYY)	2. REPORT TYPE	3. DATES COVERED (From - To)
01/08/2013	Technical Report	17/02/2010 - 16/02/2013

4. TITLE AND SUBTITLE	5a. CONTRACT NUMBER
A 1:8.7 Scale Water Tunnel Verification & Validation Test of an Axial Flow Water Turbine	DE-AC04-94AL85000/Agreement 992687

5b. GRANT NUMBER

5c. PROGRAM ELEMENT NUMBER

6. AUTHOR(S)	5d. PROJECT NUMBER
Fontaine, Arnold A.	16987
Straka, William A.	**5e. TASK NUMBER**
Meyer, Richard S.	
Jonson, Michael L.	**5f. WORK UNIT NUMBER**

7. PERFORMING ORGANIZATION NAME(S) AND ADDRESS(ES)	8. PERFORMING ORGANIZATION REPORT NUMBER
Applied Research Laboratory PO Box 30 State College, PA 16804	TR 13-002

9. SPONSORING/MONITORING AGENCY NAME(S) AND ADDRESS(ES)	10. SPONSOR/MONITOR'S ACRONYM(S)
Sandia National Laboratories Wind Energy Technology Department Albuquerque, NM 87185-1124	
	11. SPONSOR/MONITOR'S REPORT NUMBER(S)

12. DISTRIBUTION/AVAILABILITY STATEMENT

Distribution Statement A: Approved for public release, distribution unlimited.

13. SUPPLEMENTARY NOTES

14. ABSTRACT

A new marine hydrokinetic turbine rotor was designed, in collaboration with Sandia National Laboratories and the University of California – Davis. A 1:8.7-scale model was fabricated and experimentally tested to provide an open platform dataset for further study and computational model validation. The water tunnel test of this three-bladed, horizontal-axis rotor quantified power production, blade loading, near-device flow-field characterization, cavitation performance, and noise generation. This report documents the small-scale model test in detail, provides a brief discussion of the rotor design and comparison against low-order modeling tools.

15. SUBJECT TERMS

Renewable Energy
Marine Hydrokinetic Turbines

16. SECURITY CLASSIFICATION OF:			17. LIMITATION OF ABSTRACT	18. NUMBER OF PAGES	19a. NAME OF RESPONSIBLE PERSON
a. REPORT	b. ABSTRACT	c. THIS PAGE			Arnold Fontaine
					19b. TELEPHONE NUMBER (Include area code)
U	U	U	UU	110	814-865-1741

ABSTRACT

As interest in waterpower technologies has increased over the last few years, there has been a growing need for a public database of measured data for these devices. This would provide a basic understanding of the technology and means to validate analytic and numerical models. Through collaboration between Sandia National Laboratories, Penn State University Applied Research Laboratory, and University of California, Davis, a new marine hydrokinetic turbine rotor was designed, fabricated at 1:8.7-scale, and experimentally tested to provide an open platform and dataset for further study and development. The water tunnel test of this three-bladed, horizontal-axis rotor recorded power production, blade loading, near-wake characterization, cavitation effects, and noise generation. This report documents the small-scale model test in detail and provides a brief discussion of the rotor design and an initial look at the results with comparison against low-order modeling tools. Detailed geometry and experimental measurements are released to Sandia National Laboratories as a data report addendum.

TABLE OF CONTENTS

LIST OF FIGURES

LIST OF TABLES

NOMENCLATURE

Alpha $\rightarrow \tan^{-1}(Z/Y)$

A_r Rotor swept area $\rightarrow \pi r^2/4$

B   Bias errors

c   local blade chord

$C_{0,1,2}$ Calibration equation constants

C_P Coefficient of Power $\rightarrow P/(0.5 \bullet \rho \bullet U^3 \bullet A_r)$

$c_{p,min}$ minimum pressure coefficient $\rightarrow (p-p_\infty)/(0.5 \bullet \rho_\infty \bullet U_\infty^2)$

C_Q Coefficient of Torque $\rightarrow Q/(0.25 \bullet \rho \bullet U^2 \bullet A_r \bullet D_r)$

C_T Coefficient of Thrust $\rightarrow T/(0.5 \bullet \rho \bullet U^2 \bullet A_r)$

d   blade drag

D_f LDV fringe spacing

D_r Rotor Diameter

E   Young's modulus

FFT   Fast Fourier transform

F, F_{corr} strain gage "gage factor" and "gage factor" correction

f_d LDV measured Doppler frequency

Fs   sampling frequency

l   blade lift

L_o, L_i object calibration length and image calibration length

M   image magnification

N   rotation rate of the turbine (rev/min), # of samples in uncertainty analysis

p   local static pressure

p_v, p_∞ vapor pressure of fluid, reference pressure @ infinity

P   Power: directly measured with dynamometer P_D, estimated from torque$\bullet$rpm P_Q, Random errors in Uncertainty analysis

PL   Peak locking level

ppm   parts per million

Q   Torque

Radius $\rightarrow \sqrt{(Y^2 + Z^2)}$

Re_c Chord based Reynolds number $\rightarrow Uc/\nu$

$R_{g,L}$ Gage resistance or lead wire resistance

rpm   shaft speed in revolutions per minute

ΔS_i particle displacement in PIV

S_{WH} Radiated sound calibration curve

T   Thrust

ΔT laser pulse delay in PIV

TI   velocity turbulence intensity $\rightarrow TI = \sigma_{ui}/V_{mag}$ where V is local mean velocity magnitude

TSR   Tip speed ratio $\rightarrow \pi ND_r/(60 \bullet U_\infty)$

TVR   transmit voltage response

U, U_∞ Axial Reference velocity, free stream Axial Velocity. U component aligned with X

U_0 Reference velocity used in scaling

V	Velocity component aligned with the Y direction, or voltage depending on context.
V_{exc}	strain gage bridge excitation voltage
V_n	measured strain gage signal
V_r	Post processed velocity component in radial direction measured from rotor axis positive outward. Components transformed into cylindrical coordinates (X, Radius, Alpha)
V_S	voltage autospectrum of source
V_T	Post processed velocity component in the circumferential or tangential direction Alpha. Components transformed into cylindrical coordinates (X, Radius, Alpha)
V_{Tunnel}	Reference velocity at X=0.254 m (10")
V_{WH}	voltage autospectrum of window hydrophone
V_X	Post processed velocity component in axial direction X
V_Y	Post processed velocity component in cross-flow direction Y
V_Z	Post processed velocity component in cross-flow direction Z
V_{zero}	zero voltage
V_∞	Reference velocity at X=1.68 m (66")
W	Velocity component aligned with the Z direction
X	Axial or streamwise location measured in the tunnel. Origin at the leading edge of the rotor hub
Y	Cross flow component measured in the direction aligned with the tower of the model. Positive in direction from rotor hub along the tower
Z	Cross flow component measured in the direction normal to the X-Y plane defined positive with a right hand rule.
α	tunnel water gas content
ε_n	measured strain
$\varepsilon_{p,q}$	P and Q principal strains
κ	Half angle between the LDV transmitting beams
λ	laser wavelength nm
ν	kinematic viscosity of the fluid, or Poisson's ratio depending on context
$\Phi_{p,q}$	principal strain axis angle
π	3.1415927
ρ	Density of water
σ	Cavitation number $\rightarrow$ $(p-p_v)/(0.5 \bullet \rho \bullet U^2)$, rms or uncertainty depending on context
$\sigma_{p,q}$	principal stresses
θ	Sensitivity coef. in uncertainty analysis

Measured and processed analog signal, LDV and PIV variable names are listed in Table 12- 16.

INTRODUCTION[1]

To improve national security through an increasingly broad energy portfolio and to aid in reducing deleterious effects of commonly used energy sources (*e.g.*, coal, natural gas and nuclear), marine hydrokinetic turbines are being developed for power generation from river, tidal, and ocean currents. Flow and wave energy converters (FECs and WECs, respectively) have seen advances toward commercial deployment in recent years. As a subset of marine hydrokinetic (MHK) devices, FECs are able to leverage the large technological history of wind energy in order to speed development; a number of prototypes have already been deployed within the waterways of the United States and internationally [2]. Their use broadens energy portfolios and, as carbon or nuclear alternative energy generators, FECs and WECs have no fuel waste and avoid perennial and fluctuating fuel costs. The latter implies that the levelized cost of energy (LCOE) is determined only by the manufacture of individual devices, the site resource, and the infrastructure and operations/maintenance (IOM) costs.

Horizontal-axis (axial flow) turbines have been viewed as the simplest and best understood investment for initial deployment and generation of power from water flow. This is because the three-bladed, horizontal-axis turbine has been the workhorse of the wind industry over the last few decades and significant advances have been made that presently allow for multi-megawatt machines and large wind farms. As a result, this conceivably removes power production research from being the priority and allows developers to focus on IOM cost reductions. However, due to the infancy of this technology for MHK applications, there are still number of hurdles to be overcome.

Cavitation, erosion, and soiling/bio-fouling will each impact performance, loading, and operations in magnitudes and time-scales not seen for wind turbines. This warrants new design considerations [3] and material/coating choices [4,5]. Noise generation and propagation may have a greater impact on organisms and the environment fostering broader turbine-species interaction than seen on land [6-8]. Survivability, reliability, and the associated operational and maintenance expenses remain a large unknown [9,10]. The experience in wind [11-15] has shown that unsteady hydrodynamic forcing due to blade-tower interactions and non-uniform inflow characteristics, mean flow gradients and turbulence, can have a significant impact on the survivability , reliability and maintenance costs of the turbine and it's sub-components, such as the drive train. To positively impact these cost drivers, the design of marine renewable energy devices will need to consider the increased steady and unsteady hydrodynamic loading due to the higher density fluid mass loading in the marine environment.

Existing research efforts have explored a variety of turbine configurations including cross-flow rotors [16,17], a mechanism based on vortex-induced vibration [18], and others [19]. Underwater installation increases the choices for mounting from solely a tower support to floating platforms and neutrally buoyant devices held in place through mooring cables [20].

Bahaj, et al. [21] recently completed a study with a horizontal axis, axial flow, 0.8-m diameter rotor tested in both a towing tank and cavitation tunnel. Their rotor used NACA 63-8xx foils and blades with adjustable pitch. Flow velocity in the experiments was limited to a maximum of 2 m/s, corresponding to a maximum mean-chord Reynolds number of less than 300,000. In these tests, they investigated the power and loading of the turbine as a function of yaw and the depth

from the free surface. Both contributed to a high variation in extracted power and applied thrust and will significantly impact design and deployment. Cavitation was investigated, with an appropriate pitch appearing to mitigate tip cavitation. A dual rotor configuration was also studied which showed the second rotor having little impact on performance.

In our investigation presented herein, a new MHK rotor was designed and fabricated at 1:8.7-scale. Water tunnel tests were conducted to measure performance, cavitation, and acoustics. In the long term, one of our explicit goals is to provide an open, validation-quality dataset suitable for formal verification and validation (V&V) studies to the MHK industry and research community. Currently, due to the proprietary nature of any individual deployments, no such publicly available data exist that the MHK industry and research community can use to benchmark and validate design tools. This paper presents an overview of the rotor design, the model test and preliminary results with comparison against low-order modeling tools. Details of the rotor geometry and experimental measurements will be released at a later date.

TEST OBJECTIVES

The objectives of the Sandia turbine test program were to provide DoE with a small-scale Verification and Validation (V&V) quality assessment of the turbine design under sufficiently high chord Reynolds number (Re_c) scaling with proper turbine loading. This V&V quality database could then be used for low-, mid-, and high-fidelity code validation. The test was designed to not only provide powering performance and flow field characterization, but to also provide unsteady data that could be used to validate design code models for the prediction of structural response to unsteady loading for dynamic load and fatigue evaluation of components and the drivetrain.

The V&V data set included:
- Turbine flow field quantification– detailed flow mapping of the turbine inflow and outflow field including blade wakes, inflow and outflow turbulence, inflow velocity spectra, tip – vortex characterization and device near-field wake characteristics.
- Turbine performance characterization – power generation relative to design point (below, on and above design), turbine-to-drive shaft loading synchronized with turbine circumferential phase.
- Turbine cavitation inception performance.
- Tower /nacelle vibration and blade strain quantification relative to blade tower interaction.
- Turbine acoustics performance: a) turbine broadband vibration noise (BBVN), b) unsteady dynamics of the turbine shaft, c) unsteady pressures on the tower, tunnel wall, and d) tower vibration levels.

The focus of the effort was to develop a database on the MHKF1 geometry of sufficient fidelity that a "model-the-model" computational study could be conducted. These computational models can then, once validated, be used to predict full scale performance with increased confidence.

ROTOR DESIGN

Erick Johnson (Sandia National Laboratories), and Henry Shiu and Case van Dam (Univ. CA, Davis) led the rotor design effort for this program. A three-bladed, axial-flow, horizontal-axis rotor was

chosen for this study. Such a turbine could be deployed in river, tidal, or ocean currents. It could be tower mounted from a river/sea-bed, suspended from a surface platform, or moored. In this study, we assume simple tower mounting in a river current and employ such in the validation experiments.

MHK hydrofoil design is a compromise of many objectives. Many are identical with those of wind turbine airfoils, as presented in previous works [22-24]. These factors include:

- Lift to drag ratio (l/d) is the most basic metric for MHK hydrodynamic performance; in general, higher l/d yields higher power production.
- Thickness is required for stiffness to counter bending moments from thrust loads. This structural requirement becomes more dominant toward inboard blade stations and is greater in MHK applications than in air because of the high density of water.
- Wind turbine airfoils are typically designed to have low sensitivity to surface roughness that can be caused by erosion from airborne particulates and accumulation of insects and other contaminants. Soiling is considered an even greater concern in MHK applications because of the likelihood of biofouling and the anticipated difficulties and high costs of access and maintenance.
- Stall should be well defined, but not too abrupt.

Waterborne operation also bears additional considerations. Cavitation is the formation of vapor cavities (bubbles) in a fluid. Its fundamentals are described in various works [25]. Cavitation can have numerous detrimental effects including degraded hydrodynamic performance, vibration, noise, and erosion of impinged surfaces. Its quantitative characteristic is the cavitation number σ:

$$\sigma = \frac{p - p_v}{\frac{1}{2}\rho U_o^2}$$

where p and U_o are a reference pressure and velocity, and p_v and ρ are the fluid vapor pressure and density. As pressure in the flow drops towards the vapor pressure as a result of decrease in operating depth or increase in localized velocity, the likelihood of cavitation increases. By definition, the lowest pressure on a hydrofoil surface or flow field (in non-dimensional form) is:

$$c_{p,min} = \frac{p_{min} - p_\infty}{\frac{1}{2}\rho_\infty V_\infty^2}$$

where $c_{p,min}$ is the minimum surface pressure. p_∞, ρ_∞, and V_∞ are freestream pressure, density, and velocity respectively. Under a given set of conditions, a hydrofoil with higher $c_{p,min}$ values is therefore less likely to incur cavitation. The local $c_{p,min}$ typically occurs at the suction peak of a foil, near its leading edge. However for many lifting foils, cavitation may first occur off body in areas such as the tip vortex.

Singing is a hydroacoustic, hydroelastic phenomenon typically associated with ship propellers. Vortex shedding from either sharp or blunt trailing edges can induce audible harmonic tones or trailing edge vibration [26]. It is a complex phenomenon that appears to be affected by hydrofoil

geometry, rotor geometry (three-dimensional effects), blade material and structure, surface roughness, and inflow turbulence levels. Almost all studies have been empirical. The occurrence of singing is difficult to predict and there have been cases of propellers of identical design where some propellers sang and others did not. This suggests that singing is sensitive to otherwise acceptable manufacturing tolerances [27]. Singing is commonly treated a posteriori by beveling the suction side trailing edge surface via grinding. Increasing trailing edge thickness can reduce the likelihood of singing a priori. Additionally, certain trailing edge geometries are less susceptible to singing [28]. Many of these "anti-singing" geometries are highly asymmetric with the intent of inducing separation and vortex shedding slightly forward of the trailing edge on one surface (typically the suction side) while maintaining smooth flow off the other. The vortices are then expected to dissipate shortly downstream within a fraction of a chord length, avoiding the formation of a coherent vortex street.

The initial foil analysis and design were conducted with XFOIL [29]. For analysis, XFOIL couples the integral boundary layer equations with a potential flow solver. Corrections for compressibility and blunt trailing edges are included. Transition is modeled with the en method. XFOIL has an inverse foil design routine via classical conformal mapping. As with other such codes, a specified surface velocity distribution can be transformed into a foil geometry. A number of minor modifications were made to XFOIL including: (1) import and export of velocity distributions in the inverse design module, (2) parameterized specification of various velocity distribution segments in the inverse design module, including extents of constant velocity, concavity of the pressure recovery, and splicing with Bezier curves, and (3) additional options for maximum and trailing edge thickness in the foil geometry module. Additionally, a set of wrapper scripts was developed to automate runs and a number of external, GUI-based routines were written to manipulate airfoil geometries and velocity distributions.

OVERFLOW is a 2-D/3-D viscous, unsteady Reynolds-averaged Navier Stokes (RANS) computation fluid dynamics (CFD) solver [30]. It includes numerous options for turbulence models and boundary conditions, dual time stepping for time accurate calculations, and supports overset (Chimera) grids. OVERFLOW was used for more detailed study of later design iterations. While computationally much more expensive than XFOIL, it can provide higher fidelity and was essential for more complex foil geometries such as the anti-singing trailing edge profiles.

This program focused on designing a family of hydrofoils, MHKF1, specifically for MHK power applications [31,32]. The foils were designed to minimize performance losses from soiling/bio-fouling and reduce the likelihood of cavitation. In addition, the outboard and mid-span hydrofoils incorporated trailing edge geometries that were designed to minimize singing, a coupled hydroacoustic-hydroelastic phenomenon in which thin, sharp trailing edges produce significant high-frequency noise due to a resonant vibration [28, 33]. The "anti-singing" trailing edges were applied to the outboard 50% span. Flatback foil geometries [34] were used on the inboard 50% span. Flatback foils have significant trailing edge thickness, which increase blade strength while promoting flow attachment on large thickness-ratio foils. Finally, the root shape of the blade remained a flatback foil instead of transitioning to a cylinder. This allowed a high sectional twist to be maintained to the hub and also provided a further increase in blade strength at the root. The non-circular root does complicate blade integration with a pitch drive. While the rotor was designed to leverage existing technology already designed and deployed, we wanted to

4

investigate advances that could maintain performance while providing increased reliability, reduced fatigue, cavitation, and soiling, and reducing environmental impacts (*e.g.*, noise pollution).

Shiu et. al. [31] describe the hydrofoil design in detail with computed performance predictions. The design process is summarized here. The reader is referred to Shiu et. al. [31] for details on the performance predictions. Figure 1 illustrates the MHKF1 family of hydrofoils. The foil nomenclature used herein consists of two tuples. The first indicates the family. The second tuple is the maximum thickness, followed by optional characters that indicate a variant of the nominal foil. For example, MHKF1-180s is a foil of the MHKF1 family with 18.0% maximum thickness; it is the "s" variant of the foil. Note that the variant designations are not assigned in alphabetical order; variants "a" through "r" do not necessarily exist in the example.
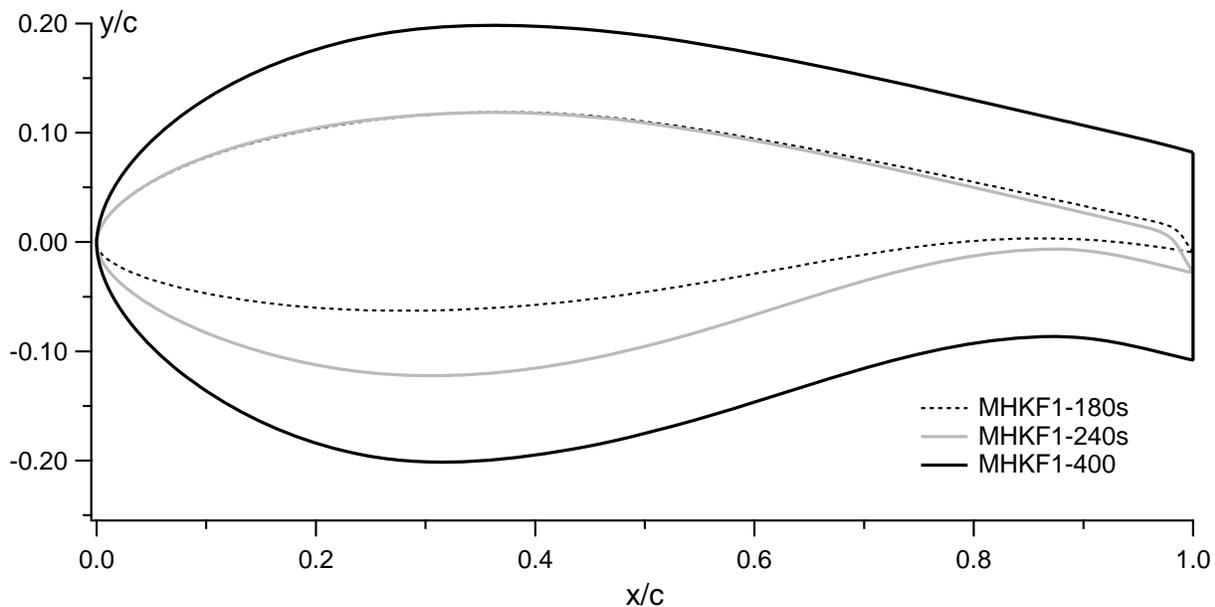
Figure 1. MHKF1-family of hydrofoils with anti-singing and flatback trailing edge geometries.

The MHKF1-180 is a tip hydrofoil designed for the tip or outboard section of a rotor, from approximately the 75% radial station (0.75R) to the blade tip. Because of the high local velocity and low ambient pressure (as a blade rotates to its zenith, the tip reaches the shallowest depths across the entire rotor), cavitation concerns are greatest at the tip. MHKF1-180 has a maximum thickness (tmax) of 18.0% of chord (0.180c). This selection was based on a survey of existing wind turbine tip airfoils. Greater thickness could offer better structural efficiency, but also incurs a larger drag penalty.

Based on a preliminary MHK rotor design [35], a full-scale design chord Reynolds number of 1.5×10^6 was selected. To achieve high l/d, we extended laminar flow on the suction surface was employed by specifying a long, constant segment in the velocity distribution [36] in inverse design. As discussed in a number of airfoil design works [37,38], this results in a favorable pressure gradient that, when coupled with a transition ramp to a concave, Stratford-like pressure recovery, is resistant to laminar separation even with an overall steep pressure recovery. The three features above – the length of the constant velocity segment, the geometry of the

transition ramp, and the concavity of the pressure recovery – were parametrically varied to maximize l/d. To maintain more favorable pressure gradients that are more resistant to premature tripping from surface roughness, the thickness of the suction side surface was limited [39].

Cavitation risk on hydrofoils is often discussed in terms of airfoil geometry. Conceptually, increasing leading edge radius reduces the flow acceleration around the leading edge, thereby reducing the suction peak and $-c_{p,min}$. However, $c_{p,min}$ can be directly manipulated in inverse design. The suction peak was softened by varying amounts to find a balance between improvement in $c_{p,min}$ and impact on lift. The "chin" of the hydrofoil – the forward section of the high pressure side – was then parametrically adjusted with a Bezier curve to provide a cleaner stall.

To address concerns about singing, the relatively thin trailing edge was thickened. Because this has a detrimental impact on drag and l/d, the thickness addition was limited. The trailing edge thickness was increased matching the thickness of the NACA 4412 at approximately 0.85c. Although this cannot ensure that singing will not occur, singing of the NACA 4412 has not been noted in prior water tunnel tests [40,41]. To preserve the design of the suction surface, thickness was added almost exclusively to the pressure surface. This increased the aft camber, providing a benefit in increased lift. The increase in trailing edge thickness from 0.0037c to 0.0192c reduced $(l/d)_{max}$ by 17 (XFOIL, free transition). To further mitigate the risk of singing, anti-singing trailing edge geometries were applied. MHKF1-180s has a sheepsfoot profile devised from the studies of Heskestad and Olberts [28]. The profile starts at approximately 0.97c and the trailing edge angle is 45°. The resulting hydrofoil is the MHKF1-180s, shown in Figure 1. Details of the MHKF1-180s trailing edge are provided in Shiu et. al. [31].

The mid-station hydrofoil, MHKF1-240, is designed for the mid-section of a rotor blade, from approximately 0.40R to 0.75R. Greater thickness is necessary to counter increasing structural loads. However, hydrodynamic performance remains very important over this portion of the blade. The full-scale chord design Reynolds number (Re_c) was maintained at roughly $1.5x10^6$. Although the local flow velocity is lower at more inboard radial stations of the blade, the Re_c is maintained by increasing chord lengths. MHKF1-240 was developed directly from the MHKF1-180 design. The thickness distribution of MHKF1-180 was linearly scaled to a maximum thickness of 0.240c. As is common practice with wind turbine airfoil families, the thickness was added only to the high pressure surface, preserving the laminar flow and roughness insensitivity of the suction surface. This, however, de-cambered the foil, shifting its lift curve slope down. As on MHKF1-180, thickness was added to the aft portion of the foil as an anti-singing measure. The ratio of the nominal trailing edge thickness to the maximum hydrofoil thickness was approximately matched with that of the MHKF1-180, providing a somewhat equivalent degree of singing resistance to both hydrofoils [33]. Again, the addition was applied only to the high pressure surface, restoring some of the foil's camber.

The "undercut" at the aft portion of the hydrofoil high pressure surface was further adjusted to recover lift. This can be likened to sizing a trailing edge split flap. The aft suction surface was also slightly adjusted. As with the MHKF1-180, the hydrofoil chin was modified to provide a cleaner stall. In general, cavitation was a lesser concern with this mid-station hydrofoil than on the

MHKF1-180 tip hydrofoils because of the reduced local dynamic pressure further inboard. The final hydrofoil, MHKF1-240s in Figure 1, has a maximum thickness of 0.240c. The MHKF1-180s and MHKF1-240s exhibit almost identical suction surfaces. A sheep's-foot anti-singing trailing edge profile was applied.

MHKF1-400, shown in Figure 1, is a root hydrofoil for application on the inboard portion of a blade. Structural requirements dominate these inboard stations, resulting in very high maximum thickness values. MHKF1-400 was developed directly from the other MHKF1 hydrofoils. The forward portion was linearly scaled from MHKF1-240 to a maximum thickness of 0.400c. The trailing edge is blunt with a very large thickness, sometimes referred to as a flatback geometry. Compared to traditional trailing edges with limited thickness, flatbacks can offer better structural and lift characteristics with a relatively modest compromise in drag [42,43]. Significantly, they can also limit inboard separation on a rotor [44]. There are numerous methods for developing flatback geometries including truncation; logarithmic, polynomial, and other splining functions; and numerical optimization [45]. On MHKF1-400, the aft suction and pressure surfaces were each taken directly from MHKF1-240 aft of the points of maximum thickness on each side. This resulted in a 0.191c thick trailing edge and ensured good geometric compatibility with the other MHKF1 hydrofoils.

Based on operation in a relatively energetic river site such as the Mississippi River, a 2 m/s mean inflow was specified as a design condition. A rotor diameter of 5 m was selected, which could achieve reasonable energy capture while avoiding significant bathymetric, navigational, and recreational restrictions. The blade geometry was optimized for hydrodynamic efficiency using an inverse blade-element-momentum (BEM) code, which included Prandtl corrections for tip and root losses [46]. The final TSR was selected to be 4 (30.6 rpm full-scale), which provided a balance between power performance and loading limitations. The angle of twist at the root was modified slightly from the ideal twist to provide a compromise between the chord length, hub size, and bending loads.

To provide confidence in the final design prior to fabrication, a finite element analysis (FEA) and unsteady Reynolds-averaged Navier Stokes (URANS) simulation were performed under the largest expected loading condition at the on-design conditions. The URANS simulation under zero-yaw conditions validated the spanwise loading calculated through the BEM code, which was used to determine the bending load and deflection of the blade. This single blade simulation with periodic boundary conditions applied in the circumferential direction did not include tower-loading effects. A comparison of the spanwise torque for the full scale rotor can be seen in Figure 2. The FEA validated the cantilever beam approximation and incorporated the full blade geometry and Coriolis effects. The maximum stress from the FEA was 16.8 MPa and compared well to the maximum stress of 23.0 MPa from the cantilever beam approximation.

Table 1 shows the spanwise distribution of the twist, chord, and maximum thickness of the 1:8.7 scale turbine. The overall tip diameter is 574.2 mm and the hub diameter is 47.1 mm.

Table 1. Spanwise distribution of the twist, chord, and maximum thickness of the 1:8.7 Scale Turbine.			
Radius (mm)	Twist (degrees)	Chord (mm)	Max. Thickness (mm)
16.09	50.79	40.23	16.13
42.82	39	64.83	24.49
56.03	32.6193	77.01	28.25
69.25	28.6489	74.14	26.38
82.47	25.1206	70.11	24.17
95.69	22.042	65.86	21.99
108.91	19.3559	61.61	19.89
122.13	16.9914	56.82	17.72
135.34	14.8943	52.55	15.82
148.56	13.1494	48.77	14.14
161.78	11.8782	45.41	12.67
175	10.7512	42.41	11.37
188.22	9.7429	39.71	10.21
201.44	8.8282	37.24	9.16
214.66	7.9828	34.94	8.21
227.87	7.1841	32.72	7.33
241.09	6.3984	30.46	6.48
254.31	5.5894	27.9	5.63
267.53	4.7073	24.39	4.66
280.75	3.5408	14.31	2.6
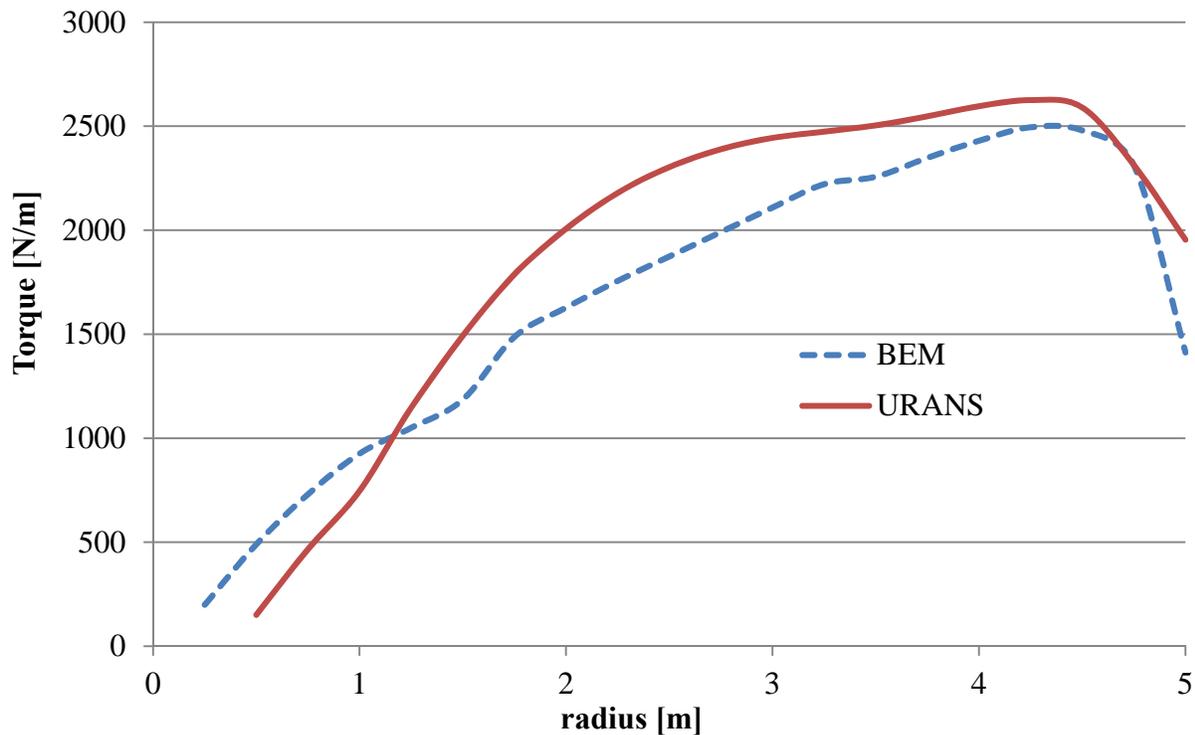
Figure 2. Comparison between BEM and URANS torque of the full scale turbine.

1:8.7 SCALE WATER TUNNEL TEST

The goal of this small-scale turbine test was to characterize the hydrodynamic and structural performance of the three-bladed MHKF1 turbine under realistically loaded operating conditions.

Test Methodology

Model

A 1:8.7 scale model of the 5 m diameter MHKF1 rotor was tested in the Penn State University/Applied Research Laboratory (ARL) Garfield Thomas Water Tunnel (GTWT). The scale factor was chosen as a compromise between tunnel blockage effects (favoring a smaller scale) and Reynolds number effects (favoring a larger scale). The GTWT is a high-speed, high Reynolds number, closed-loop water tunnel used for research of cavitation, acoustics, and advanced rotating machinery design. The tunnel test section is 1.22 m in diameter by 4.27 m long. A variable pitch impeller produces test section velocities from 0 to 16 m/s. Freestream turbulence is controlled by a honeycomb and screens upstream of a 16:1 contraction ratio nozzle feeding the test section. The tunnel can accurately control test section static pressure (20.7 kPa to 413.7 kPa) and water dissolved air content (1 to ~20 molar ppm).

The model consists of a 1:8.7 scale model of the MHKF1 turbine mounted to a scaled 76.2 mm diameter nacelle and 76.2 mm diameter tower and connected to the downstream dynamometer assembly as illustrated in Figure 3. The unit was located in the middle window assembly of the

9

tunnel test section. A long 63.5 mm diameter by approximately 2 m long drive shaft connected the tower/nacelle/turbine assembly to the downstream dynamometer housing containing a motor/generator in a direct drive configuration where power generated by the turbine could be measured and extracted. The test-scale rotor was fabricated out of 17-4 PH stainless steel in order to maximize strength and minimize deflections. A monoblock design was chosen over a separate blade–hub design for increased control over dimensional tolerances to maintain scaled geometry and increase structural integrity. The blade bending stress, which served as the primary structural design constraint, was determined by approximating the blade as a cantilevered beam and an iterative approach was used with the BEM code to solve for the final chord, twist, and tip speed ratio (TSR). Tip deflection under load was estimated to be negligible under the current test conditions based on measurement accuracy of tip deflection. A load safety factor of 1.5 and material safety factor of 2.5 were used. A CAD rendering and the fabricated scaled rotor are shown in Figure 4. The assembly drawing with call-outs for the individual parts is given in the ARL drawing number 146451.

The monoblock rotor Model was fabricated by NuCon Corporation. The manufactured model was laser scanned by Exact Metrology. The results of the laser scan are provided in Appendix 2.

One blade of the three blade rotor, blade 2 in Figure 3, was instrumented with strain gage rosettes located at the 25% and 50% span locations on the blade labeled in Figure 3. Each rosette comprised three strain gage bridges (Omega model #SGD-2/350-RY61) aligned to provide the full-strain field at the mounting location. Blade 2 was modified to include strain gage pockets and wire passages on the pressure side of the blade. The wire passages continued through ~3 mm diameter holes drilled into the hub allowing the wires to enter a pocket at the center of the hub. A compliant urethane epoxy was used to fill all cavities and water proof the mounted strain gage rosettes and wires within the passages. Once cured, the epoxy resin was hand finished to smoothly blend the epoxy into the blade contour. All modifications were applied to the pressure side of the blade to minimize impact of surface discontinuities on blade performance, hydro and cavitation. The rotor was laser scanned by Exact Metrology Inc. (www.exactmetrology.com) after instrumentation was completed to provide an accurate measure of the as-built geometry with instrumentation. The inspection report is included in the appendix of the report.
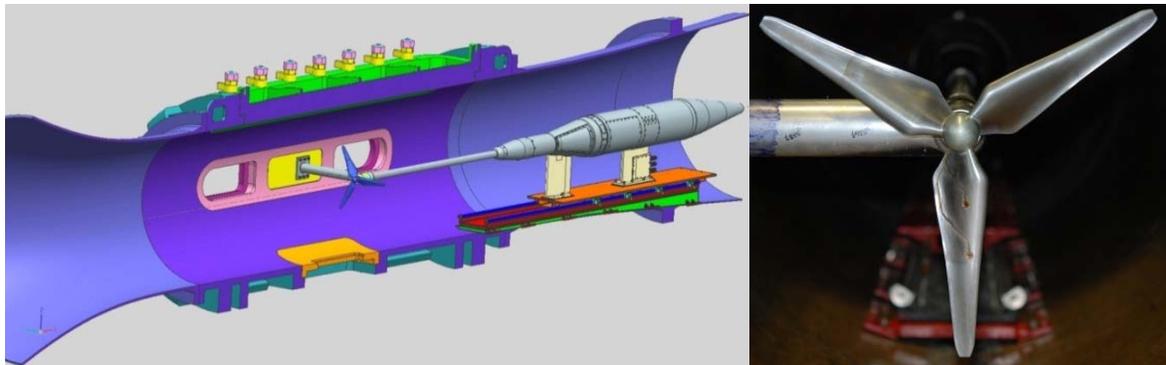
Figure 3. (Left) CAD drawing of The ARL Penn State 1.22 m water tunnel with the turbine and dynamometer installed and (right) installation of the 1:8.7 scale rotor.
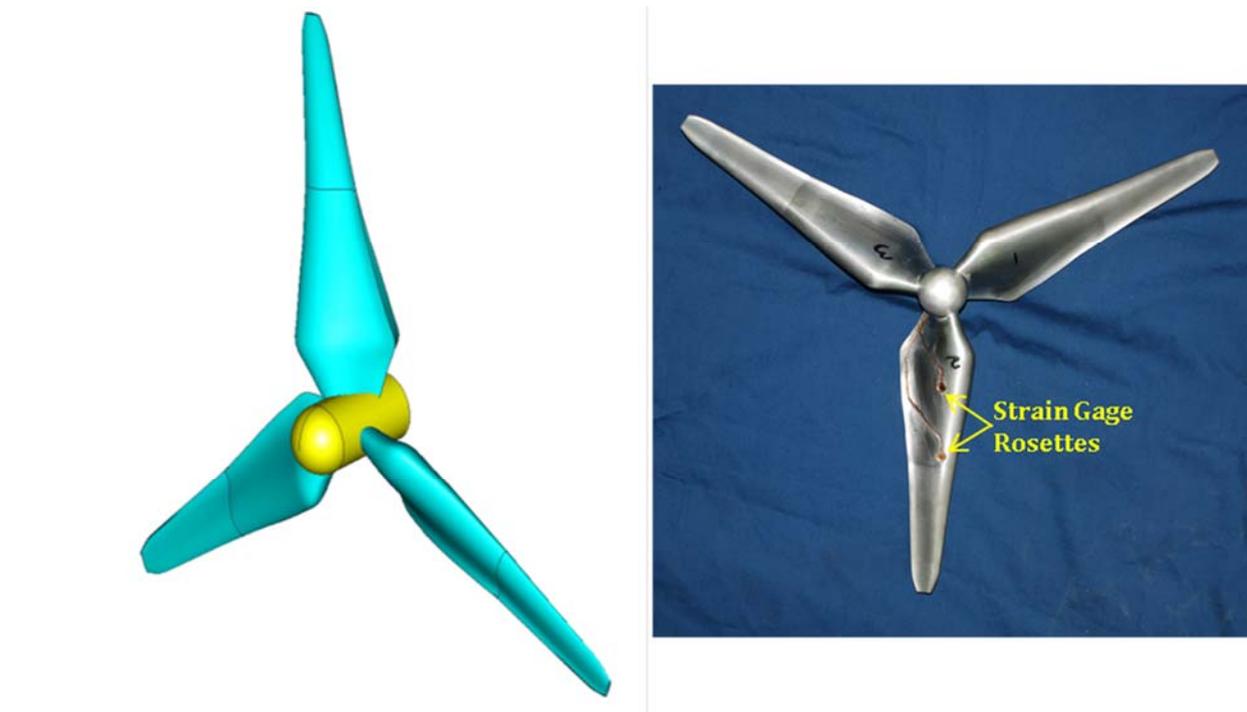
Figure 4. The (left) CAD and (right) fabricated scaled rotor.

The nacelle/tower configuration provided the primary support for the upstream drive shaft bearing. A two-component bending moment cell was located immediately downstream of the rotor at the rotor hub to drive shaft attachment as shown in Figure 5. The load cell provided unsteady bending moments transmitted to the upstream end of the drive shaft by the rotor plane during rotation. The blade strain gage wires and the bending moment wires were mounted to a water proof connector shown in pink at the on the end of the drive shaft at the shaft coupler at the end of the nacelle. Unsteady pressure was measured on the tower face at four spanwise locations (42%, 74%, 106% and 117% span) on the upstream face of the tower to measure blade tower induced unsteady pressure.
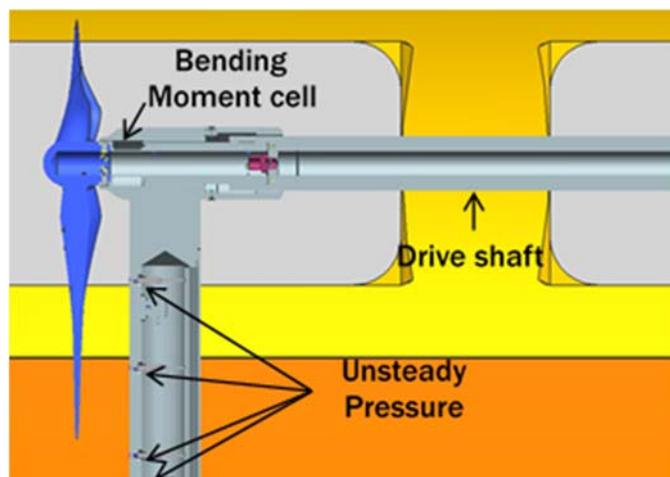
Figure 5. Close-up view of the turbine/nacelle/tower/driveshaft assembly.

Measurements and Test Conditions

The following list summarizes the measurements obtained during this test program for a given tunnel velocity and pressure.

1. Power data including direct power generation (generator output), measured torque-rpm calculation, and measured shaft thrust and torque.
2. Blade loading: root and mid-span blade strain using multi-component strain gage rosettes.
3. Dynamic loads: unsteady shaft torque, thrust, and rotor-to-shaft bending moments at the rotor hub to drive shaft attachment.
4. Unsteady tower pressures.
5. Cavitation performance: cavitation inception and breakdown.
6. Radiated sound: Mid to high frequency using hydrophones.
7. Detailed flowfield measurements: laser Doppler velocimetry (LDV) and particle image velocimetry (PIV).
8. Flow visualization: Blade oil-paint surface application, tower mini-tuft application and high-speed video.

Operating conditions ranged from an inflow of 2-7 m/s and corresponding TSR ranging from approximately 1 to 10. Data for powering, blade and dynamic loading, and unsteady tower pressures were recorded at a rate of 4 kHz for all operating conditions. LDV and PIV flow measurements were recorded at the on-design operating conditions. Axial and transect planes of measurement were taken at multiple locations both upstream and downstream of the turbine. Cavitation tests for inception and torque/thrust breakdown were conducted at the design TSR of 4 at a velocity of 4 m/s. Acoustic measurements were recorded at three locations in the tunnel (2 hydrophones mounted externally to the test-section wall and 1 hydrophone array in a submerged cavity above the rotor) under both bare nacelle and powered turbine conditions. The lower flow speed for the acoustic measurements was selected to minimize tip vortex cavitation noise at the 5 m/s design condition. Blade-synchronized video and high-speed video were used to record tip vortex and blade cavitation as well as surface paint and mini-tuft flow visualization.

A range of conditions was run to fill the operational space above and below the design conditions, where the chosen on-design condition was a 5 m/s inflow. This resulted in a rotational speed of approximately 660 RPM at TSR = 4. The chord Reynolds number for these conditions was nearly 500,000 at about 95% of the span, where the full-scale rotor would be approximately 2,000,000. The maximum Reynolds number for this experiment was 700,000. The tunnel inlet velocity had a measured turbulence intensity level of less than 0.3%. Figure 6 shows the test setup within the tunnel.

Instrumentation

The experiment instrumentation included the following:
- A DynaTec Inter-Loc V modular digital multi-loop, motor/generator dynamometer for direct power measurements.
- A shaft-mounted BNI rotational speed encoder for RPM with a resolution of 3600 counts.

- An ARL manufactured shaft-mounted, two-component, thrust and torque cell mounted inside the dynamometer, ARL part numbers 116625-3 (thrust) and 117386 (torque).
- Independent measurement of torque from an Interface T6-500-A6A rotary torque transducer that was part of the DynaTec Inter-Loc V control system.
- An ARL manufactured two-component, custom shaft bending moment cell, ARL part No. D146556, mounted at the rotor-to-drive shaft connection in the nacelle shown in Figure 5.
- Three-component, strain gage rosettes (Omega SGD - 2/350 - RY61) at two (2) locations (25% and 50% span) on a single blade, ARL drawing No. D146552, shown in Figure 4.
- Four (4) PCB 105M147 unsteady pressure transducers mounted in the tower at locations coincident with 42, 74, 106, and 117% of the turbine blade span, shown in Figure 5.
- Triaxial accelerometer, PCB model J356B07, mounted at the top of the tower adjacent to the nacelle attachment for separating mechanical vibration from unsteady pressure.
- Static pressure measurements on the tunnel wall at axial locations relative to the upstream end of the 14-foot tunnel test section: 0.254 m, 0.762 m, 1.37 m, 1.68 m, 2.03 m, 2.235 m, 2.82 m (10", 30", 54", 66"x2, 80", 88", and 111"). The 1.68 m (66") location near the plane of the rotor (situated approximately 1.9 m (76") downstream of the test section upstream end) included two transducers at opposite sides of the tunnel to account for the effects of the horizontally mounted tower. These measurements used Heise DXD-100 digital absolute pressure transducers. Figure 6 graphically illustrates the locations of the pressure measurements.
- Total pressure via Kiel probe mounted upstream of the test section nozzle, shown in Figure 6. Total pressure was measured with a Heise-150 transducer and was used to provide axial velocity measurements along the test section using the difference between the Kiel measured total and the local wall-measured static pressure.
- A reference velocity Pitot-static probe was located at the 0.254 m (10") location shown in Figure 6. The differential pressure was measured with a 68.95 kPa_d (10 psid) transducer (Sensotech SN995617).
- Atmospheric pressure was measured via a Setra Model No. 370 pressure transducer.
- Water temperature was measured with a StoLab RTD temperature transmitter model # 911PL/FC.
- Dynamometer internal pressure measured using a Sensotec differential transducer.
- Detailed flow field mapping using two-component laser Doppler velocimetry (LDV), two-component planar particle image velocimetry (PIV), and three-component stereo PIV.

The individual measurement systems will be described in detail in the following sub-sections.
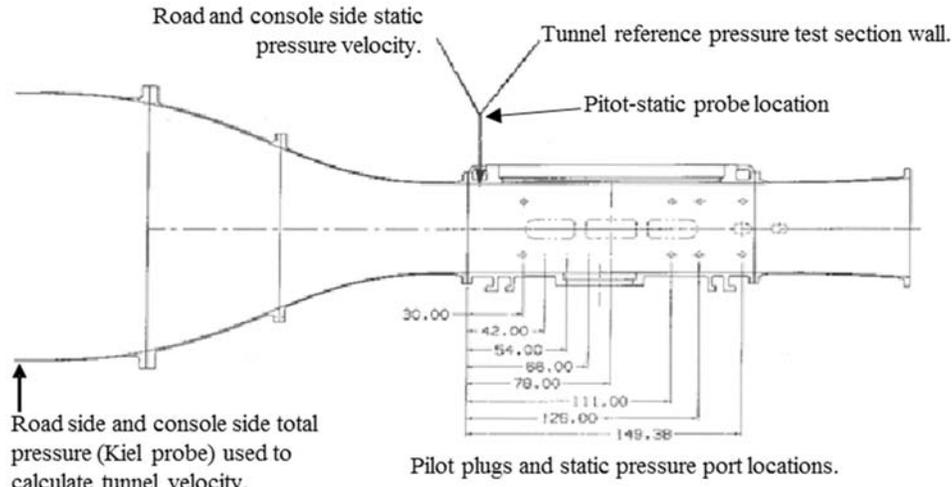
Figure 6. Standard pressure probe locations in the GTWT tunnel test section.

Data Acquisition

Data acquisition was performed using National Instruments (NI) data acquisition hardware and software. The data acquisition hardware was based on NI compactDAQ chassis instrumented with a variety of acquisition modules. These modules are summarized in Table 2.

Two compactDAQ chassis were used to acquire the data. Chassis 1 acquired the data at a 2000 Hz sample rate with exception of the NI9219 module which sampled the data at 0.5 Hz. Chassis 2 acquired the data at 4096 Hz. Sensor voltage signals were connected to the modules as shown in Table 3. In addition to the voltage data acquisition, an NI9214 6 channel digital IO module was used to acquire angular position and shaft RPM.

The data acquisition software was a custom LabView based application written in-house. This software package controls the multiple chassis and modules to acquire the voltage and RPM data. In addition to acquiring the raw voltages, the software takes and applies zero data as well as calibration coefficients. It also is able to apply user defined reduction formulas to the acquired data. Voltage data is converted to engineering units by applying the zeros and calibration coefficients.

$$EU = C_0 + C_1 \cdot (V - V_{zero}) + C_2 \cdot (V - V_{zero})^2$$

Where EU is the result in engineering units, C_0, C_1 and C_2 are the calibration coefficients, V is the signal voltage and V_{zero} is the zero condition voltage.

Table 2. Data acquisition hardware and specifications.			
Module	Fs (Hz)	Resolution (bits)	# Chans
NI9205	250000	16	32
NI9219	100 (0.5)	24	4
NI9229	10000	24	4

14

Table 3. Data acquisition module assignments for sensors.				
Chassis 1	F_s=2000 Hz (0.5 Hz)		Chassis 2	F_s=4096 Hz
Module	Sensor		Module	Sensor
NI9205	WaterTemperature		NI9229	PTower40
	DyneSpeed			PTower70
	DyneTorque			PTower100
	DynePower			PTower110
NI9219	D117386		NI9229	TAccel_x
	D116625_3			TAccel_y
	ShaftTorqueThrust_sens			TAccel_z
	P_delta		NI9229	BldRosMid1
NI9229	ShaftMom_sens			BldRosMid2
	BldRosMid_sens			BldRosMid3
	BldRosHub_sens			ShaftMom1
			NI9229	BldRosHub1
				BldRosHub2
				BldRosHub3
				ShaftMom2
			NI9229	OnePerRev
				ARL Torque Cell D117386
				ARL Thrust Cell D116625_3

The NI data, shown in Table 3, were recorded for every run during the test including the long duration runs involving the detailed flow mapping with LDV and PIV. Multiple repeat acquisitions were obtained during the flow mapping components of the test. During the duration of the test program, some of the sensors failed and therefore became unusable. The Gage 2 component of the 25% span rosette failed after the first day of testing. Gage 1 and Gage3 remained functional through remainder of the period of testing. Gage 1 in the mid span rosette failed on Nov 13th, test 3494 run 5. The epoxy potting failed in the mid span rosette on Nov 30th. The bending moment load cell, moment A, failed due to either water-proofing failure at the bridge or a leak in the cell water proof connector. This occurred on Nov 19th. A test matrix schedule will be presented later in the report. Although we were not able to maintain function in all sensors through the duration of the test, enough repeat conditions during the powering, cavitation and flow mapping tests were acquired to fill the V&V test matrix with the exception of the 25% span blade strain.

Powering and Dynamometry

Turbine powering performance tests were conducted in the ARL Penn State 48-inch water tunnel facility. Tests were conducted at a variety of tip speed ratios (TSR) at discrete tunnel velocities. The tunnel velocity was fixed during any particular test in order to eliminate Reynolds number effects. The tunnel static pressure was also held fixed at 310 kPa (45 psia), the maximum

15

allowable pressure for this test configuration, in order to eliminate or at least minimize cavitation effects.

The Tip Speed Ratio, *TSR* is given by

$$TSR = \frac{\pi N D_r}{60 V_\infty}$$

Where N is shaft rotation speed in RPM, D is the overall rotor diameter 574.7 mm (1.886 ft), and V_∞ is the tunnel freestream velocity.

Power coefficient is given by

$$C_P = \frac{P}{\frac{1}{2}\rho A V_\infty^3}$$

where P is the measured power output, and A is the turbine projected area given by $A=\pi D^2/4$.

Similarly, thrust coefficient is given by

$$C_T = \frac{T}{\frac{1}{2}\rho A V_\infty^2}$$

where T is the measured thrust, and torque coefficient is given by

$$C_Q = \frac{Q}{\frac{1}{4}\rho A D V_\infty^2}$$

where D is the turbine diameter, and Q is the measured torque.

The water tunnel tests were conducted at discrete freestream velocities from 2 to 7 m/s (6.56 to 22.97 ft/sec) in 1m/s increments. Tests were also conducted at the maximum allowable tunnel pressure of 310 kPa (45 psia), limited by the optical windows used in the test, to maximize the cavitation index, σ, and thereby minimize the effects of cavitation on blade loading (torque breakdown) or turbine performance. Turbine RPM was varied systematically in small increments throughout its range subject to the maximum motor torque limitation of 237 N-m (175 ft-lb), and the motor controller's ability to maintain very low RPM while steady-state data were collected at each point.

Because the walls of the water tunnel constrained the streamlines and thereby imposed a blockage effect on the flow around the turbine, it was necessary to correct the powering results for that blockage effect. The blockage correction methodology from Appendix A of Bahaj et al [21] was incorporated, based on an actuator disc model of the flow through the turbine. The flow was presumed to be uniform across any cross-section of the stream tube enclosing the turbine disc. Thus, a discontinuity of pressure was presumed across the disc, directly related to the turbine thrust load. Corrections were applied to dimensionless coefficients, *TSR, C_P,* and *C_T* and

results were compared to predictions. The detailed measurement suite obtained in this test, axial pressure gradient along test section and radial velocity profiles upstream and downstream of the turbine, allowed more accurate application of the Bahaj et al correction to the data. Note that no correction was found for the torque coefficient C_Q, and rationale will be given later for the use of measured values.

The motor-generator system used in this test program was based on an existing 56 kW/235 N-m induction motor custom made for ARL Penn State. The motor was mounted in a watertight dynamometer housing and the assembly was mounted far downstream of the turbine assembly, connected via the long driveshaft shown in Figure 3.

An ABB Motor/Generator Controller controlled powering and braking capability up to the full 235 N-m capability of the motor. The system provided stable motor operating speeds from approximately 100 RPM to 1800 RPM. The system had two modes of operation, powering and braking, and featured load stabilization throughout the range and power settings to maintain a requested RPM. Generated power was measured directly with the DynaTec dynamometer (P_D) and estimated indirectly from the product of the measured shaft torque and rpm. The two measures provide a direct estimate of the generator/control efficiency.

Powering data is reported as normalized coefficients in the form of thrust coefficient C_T, torque coefficient C_Q, and power coefficient C_P.

Flow Field Quantification

Detailed flow field quantification comprised bare hub and turbine inlet and outlet velocity field characterization including mean flow and turbulence, and near field turbine wake development. Flow field quantification was performed with phase locked two-component LDV and phase-locked planar and stereo PIV. Figure 7 graphically illustrates the locations of the flow field quantification and Table 4 lists the locations measured from the leading edge (LE) of the rotor hub.
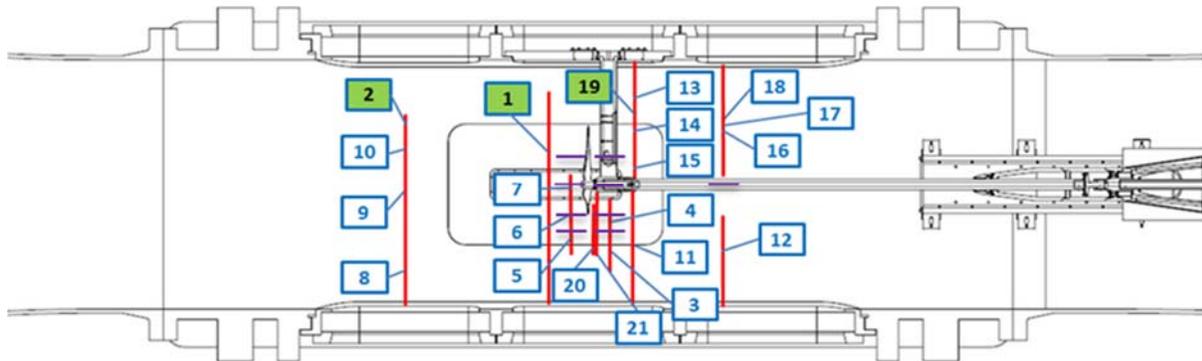
Figure 7. Graphical illustration of flow field quantification.

Table 4. Flow field mapping locations.		
LDV Survey No.	Axial Loc rel. to Nose Cone LE (cm)	Notes
1	-5.1	Bare Hub Inflow Survey
2	-80	Bare Hub Inflow Survey

3	13.5	
4	13.5	
5	-1.7	
6	-1.7	
7	-1.7	
8	-80	No Encoder Data
9	-80	No Encoder Data
10	-80	No Encoder Data
11	21.6	
12	574	Coinc. w/ PIV meas.
13	24.8	
14	24.8	No Encoder Data
15	24.8	
16	574	Centerline Height
17	574	1.9 cm above Centerline
18	574	1.9 cm below Centerline
19	24.8	Bare Hub Surv. DS of Tower
20	6.4	Coinc. w/ SPIV meas.
21	8.9	Coinc. W/ SPIV meas.
Planar PIV Meas.	(Purple Hor. Lines)	
upstream	-100mm < X < 0mm	Y = 0, 38,-38, -75 mm; Z=0 mm
upstream	-100mm < X < 0mm	Y = 0, 38,-38, -75 mm; Z>0 mm
Downstream	0 < X < 200mm	Y = 0, 38,-38, -75 mm, Z=0 mm
Downstream	0 < X < 200mm	Y = 0, 38,-38, -75 mm, Z>0 mm
Downstream	X > 570 mm	Y=0 mm, Z > 0 mm
Stereo PIV		
Downstream	Survey Locs 21 & 22	Same as LDV locations

X is the axial location with the origin at the leading edge of the rotor hub. Positive X indicates downstream direction. The distance from the stack-up line, center of the blade chord, to the leading edge of the rotor nose cone is 3.4 cm. Y is the transverse coordinate going across the tunnel test section at centerline height. The Y origin is the tunnel centerline. Positive Y is towards the road on the side of the side aligned with the tower. The numbers in the flow field map of Figure 7 correspond to the survey numbers given in Column 1 of Table 4. The boxes highlighted in green indicate bare-hub surveys conducted to determine the flowfield independent of the rotor. All other surveys were conducted with the rotor spinning at 664 RPM with a tunnel velocity of 5 m/s to yield a TSR of 4. The Z direction is the spanwise coordinate defined perpendicular to the x-y plane and defined positive using a right hand rule.

Laser Doppler Velocimetry (LDV)

A TSI Inc. fiber-optic, two-component, laser Doppler velocimeter was used in these measurements. The output of a Coherent Innova-70 5 Watt Argon-Ion laser was transmitted

through a TSI Inc. color separator / frequency shift unit (Fiber-Light Model FBL-3). The Fiber-Light splits the incoming multi-mode laser beam exiting the laser into two beams of equal intensity and then separates each beam into three single-mode wavelengths of light (476.5, 488 and 514.5 nm). A Bragg cell incorporated into the beam path within the fiber-light adds a 40 MHz frequency shift to one beam in each single-mode beam pair. The 514.5 nm wavelength beam pairs were coupled to a TSI 83 mm, two-component fiber-optic transceiver probe (model 9832. A 610 or 902.7 mm focal length lens was used to transmit and focus the laser beams into the tunnel. Table 5 lists the measurement volume characteristics for this optical setup. Each individual LDV data point was tagged with the instantaneous angular position of the rotor at the time of its arrival with the use of a TSI EIC multichannel interface to provide correlation of the rotor position with the instantaneous velocity measurement. The TSI EIC has a 3600 count resolution using a once per rev pulse from the shaft encoder.

Table 5. Measurement volume characteristics of the optical setup.								
Beam Diameter (mm)	Focal Length, f_l (mm)	beam spacing (mm)	½ angle (deg in H_2O)	Wave-length (nm)	Fringe Spacing (µm)	Measurement Volume Diameter (µm)	Measurement Volume Length (mm)	Number of Fringes
2.8	610	50	2.34°	488	5.95	135	4.4	22
2.8	610	50	2.34°	514.5	6.27	143	4.6	22
2.8	902.7	50	1.19°	488	8.79	200	9.6	22
2.8	902.7	50	1.19°	514.5	9.27	211	10.1	22

The LDV system was operated in the backscatter mode collecting scattered light from 10 µm hollow glass spheres (Potters Industries–Spherocel 110P8) used as seed. The scattered light was received by the transceiver probe through the transmitting lens system, and fiber-optically transmitted to a TSI PDM 1000 photo-multiplier system. The PDM 1000 converted the scattered light into a frequency modulated analog signal at a frequency of oscillation proportional to the speed of a seed particle traversing the measurement volume. This signal was processed using a TSI FSA3500 Doppler signal processor to calculate the signal frequency, correct for downmixing and convert the measured frequency to the particle velocity. The axial component was downmixed at a frequency of 2-3 MHz to eliminate directional ambiguity and reduce fringe bias. The vertical or tangential component was frequency shifted at 4-5 MHz. Flowsizer software v.2.0.2.0 (TSI Inc.) was used to control the FSA3500 processor. A notional illustration of the LDV set-up is shown in Figure 8. The two components of velocity captured in this test were axial and vertical which corresponds to the tangential velocity component with respect to the turbine rotor.

Velocity data were post processed using ARL developed in-house Matlab-based routines used to perform: 1) noise filtering, 2) velocity bias correction, 3) statistics up through 4th order including cross-correlations, 4) velocity spectra and 5) phase window averaging. Noise filtering is performed either by 1-D rms histogram filtering or 2-D/3-D elliptical/ellipsoidal filtering based on the measured velocity principal stresses [47]. Transit time weighting is used to correct for velocity

bias [48,49]. Velocity spectra are computed using the time-window slotting technique [50] necessary for random arrival data common in LDV. The spectra routines employ noise filtering techniques to reduce the spectral noise floor that can be high in LDV acquired data. All phase window averaging was performed using 1° phase windows.
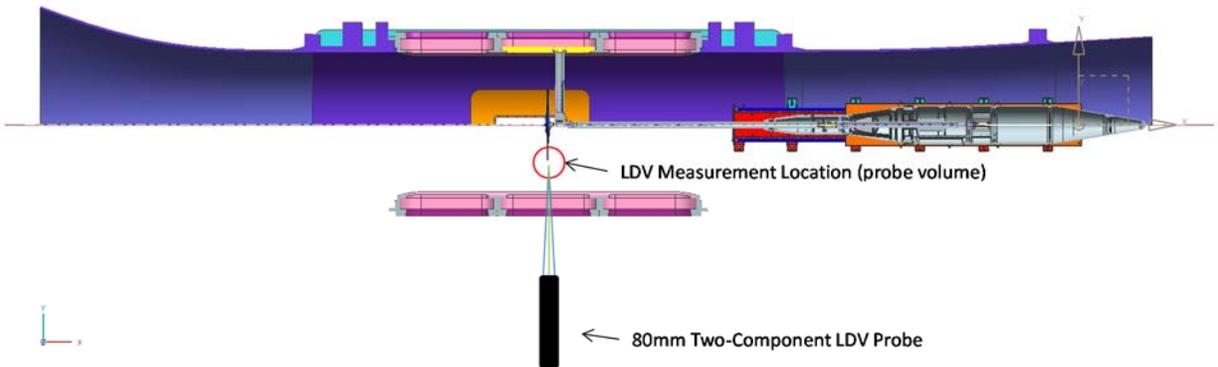
Figure 8. Notional diagram of the two-component LDV set-up.

<u>Planar and Stereo Particle Image Velocimetry</u>

Planar Particle Image Velocimetry (PIV) and Stereo Particle Image Velocimetry (SPIV) were used to measure the flowfield at prescribed locations around the turbine. The laser light sheet, which defined the measurement plane, was oriented parallel to the camera imaging planes in the planar setup. The laser light sheet was produced from the beams of a pair of pulsed Nd-YAG lasers (Gemini PIV, New Wave Research) operating at the 532 nm wavelength. A thin, planar laser light sheet was generated using high energy cylindrical and spherical lens arranged in a cylindrical than spherical configuration. The nominal laser sheet thickness was less than 0.5 mm at the imaging plane. For the planar measurements, the illuminated plane was imaged with a single PCO 1600c, 1600×1200 pixel, 14-bit CCD camera. Spatial image calibrations were performed by imaging a calibration target (TSI Inc., 203.2 mm (8") Dual sided, Dual plane PIV Target) placed in the flow tunnel at the desired plane of measurement. All calibration images were acquired with water in the tunnel to properly account for refractive index effects. The image resolution will vary with the specific measurement location, image magnification and field view. The calibrated image resolution varied from ~50 μm /pixel to ~180 μm /pixel for the stereo and planar data sets.

The cameras and lasers were synchronized with a LaVision PTU-9 laser-pulse synchronizer. The tunnel water was seeded with hollow glass spheres (Spherocel 110P8, Potters Industries), which had a nominal diameter of 10 μm and are near neutrally buoyant with a specific gravity of ~1.1. The images were collected using LaVision DaVis software v8.1.4. All images were acquired phase encoded with the rotor.

Data processing was performed using LaVision's DaVis v8.14 data processing software. This software generates the image calibrations that are applied to the raw camera images to calibrate for image magnification and correct for optical distortions that can occur when imaging through windows or due to misalignment of the optical system (camera and laser sheet). In this study, polynomial calibrations were used for most of the image set. The large field of view (FoV) planar

20

image sets used the pin-hole calibration due to the image FoV being larger than the target. Polynomial extrapolation beyond the target edges can at times introduce more error than the bi-linear calibration. Once calibrated, velocity vector maps are computed as follows:

1) image calibration is applied to the raw images,

2) image processing/filtering is performed to enhance the particle images and improve the contrast ratio,

3) velocity vectors are computed using the standard DaVis fast fourier transform (FFT) spatial correlation technique used to estimate the statistical particle displacement in a sub-region defined by the user,

4) noise filtering techniques are applied to the processed velocities both during the FFT process and post-FFT,

5) velocity is computed by normalizing the measured displacement by the known laser pulse time delay, and

6) the instantaneous vector maps are stored for later processing and statistics.

In this study, a typical image field of view ranged from ~60 mm x ~100 mm to ~140 mm x ~240mm. Laser pulse time delays were 100 microseconds for the planar mappings and 50 μs for the stereo mappings. The following processing parameters were used:

1) Sub-region multi-pass windowing from 128 x 128 down to 64 x 64 or 96 x 96 to 48 x 48 with 50% overlap providing a spatial resolution in the velocity map ranging from 3 to 8 mm.

2) Image processing included a time series background subtraction time filter. Typically a minimum intensity filter was used with a variable filter length. The value of the filter length varied according to the image signal to noise (S/N) and whether blade or hub background shadows appeared in the images.

3) Vector processing was performed with a multi-pass, decreasing interrogation window size in a two pass iteration scheme. An adaptive weighting with a 50% overlap was used. Image correction was used to apply the image calibrations. The high accuracy mode for final processing was selected.

4) Vector post processing, performed in Davis, included peak ratio filtering with default filter cutoff values. A two pass median filter was used with strongly remove and iteratively replace using a 2 rms remove and 3 rms replace setting. Finally a remove groups < 5 vectors was selected.

Velocity statistics were computed using ARL developed in-house Matlab-based post processing routines enabling noise filtering similar to that available for LDV processing. Statistics up to 4th order including cross-correlations and estimated uncertainties in the statistics up to 2nd order are computed.

For the stereo measurements, the illuminated plane was imaged with a pair of Sensicam (Cooke Corporation) cameras with a resolution of 1280x1024 pixels at 12-bits. Each camera was mounted to a LaVision remote Scheimpflug camera mount to allow the non-parallel object and image planes to be properly focused. Both cameras were equipped with 105mm Nikon Nikkor lenses. The laser light sheet was positioned between the two cameras with one camera imaging the light sheet from one side and the other from the opposite side as shown in Figure 9. The spatial calibration was performed by imaging a TSI Inc. 203.2 mm (8") dual-sided, dual-plane

diagonal target with vertical and horizontal dots spaced 10 mm apart and 1 mm spacing between planes. The target was oriented in line with the laser sheet. Stereo vector processing was performed in a similar methodology as the planar PIV processing. However, DaVis' auto calibration routine was performed to improve the accuracy of the stereo calibration. A typical field of view was ~50 mm x 130 mm.
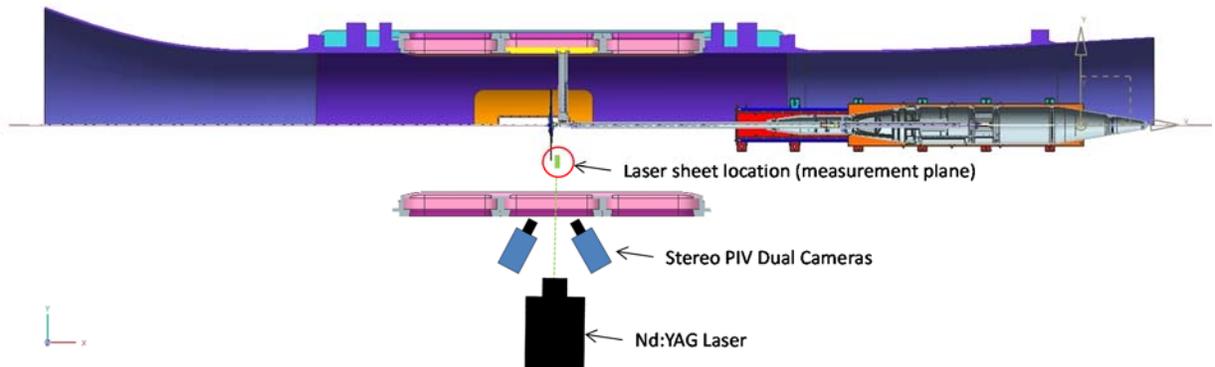
Figure 9. Notional diagram of the stereo PIV set-up.

Qualitative Flow Visualization Methods

For qualitative flow visualization, high-speed videos were captured with a Phantom (Vision Research Corp.) v1610 monochrome camera capable of up to 16,600 fps at full 1280×800 resolution (and up to 566,500 fps at 128×64 resolution). Flow indicator tufts were applied to the tower for qualitative analysis of the flow around the tower and captured with the Phantom v1610 camera. Also, a viscous, oil-based paint was applied to the turbine blades and run to form streaklines indicative of qualitative flow patterns on the blades.

Load Cell Measurements

The drive shaft thrust and torque were measured using ARL designed, manufactured, strain-gaged and water-proofed load cells. Torque cells are designed as single component, four-arm bridge units that can be mated and interchanged with single-component, four-arm bridge thrust cells in a sequential arrangement inline on the drive shaft. This arrangement allows interchanging cell designs with varying load capacity to better match expected test conditions, and eliminates cross-talk between the two cells. The load cells had a maximum frequency response of > 100 Hz which was more than suitable for steady and low frequency unsteady thrust and torque measurements. The highest anticipated blade rate frequencies were less than 50 Hz. Load cell calibrations were conducted in ARL's calibration lab. Calibrations for the torque and thrust cells are shown in Figure 10 and Figure 11.
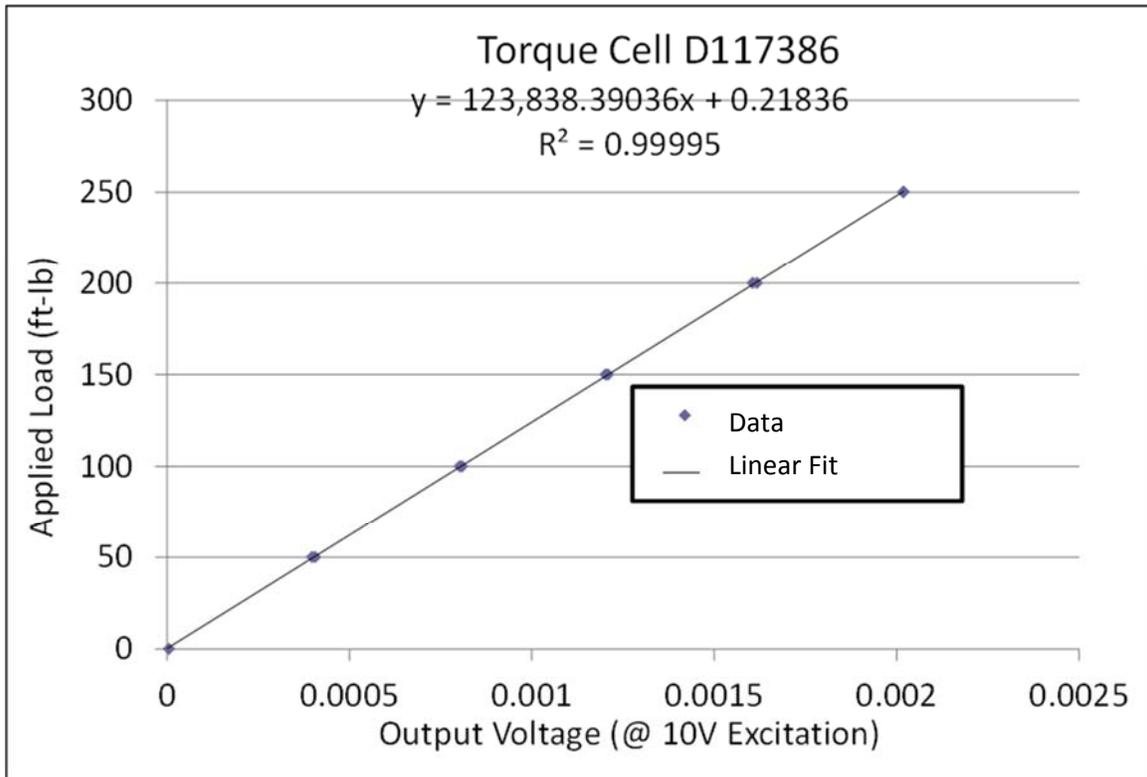
Figure 10. ARL torque cell calibration.

The two-component shaft bending moment load cell was an ARL designed, manufactured, strain gaged and water-proofed cell. This load cell was mounted in-line to the drive shaft immediately downstream of the rotor hub providing a direct measure of the two-components of bending moment applied to the rotor-drive shaft attachment by the rotating rotor. The frequency response of the load cell was sufficient to measure the steady and low-frequency unsteady bending moments applied to the shaft. The moment cell labeled A was aligned with a rotor blade while the second component labeled B was rotated 90° relative to moment A. Calibrations were performed in the ARL calibration laboratory. A two-component calibration test was performed to determine the primary and cross-talk terms of the two-component calibration matrix. The two-component calibration matrix for this load cell is:

$$c = \begin{bmatrix} -0.4607 & 67497.0124 & -895.6890 \\ 0.1536 & 1303.6018 & 70103.9303 \end{bmatrix}$$

Moment A = c(1,1) + c(1,2)*Volt$_A$ + c(1,3)*Volt$_B$
Moment B = c(2,1) + c(2,2)*Volt$_A$ + c(2,3)*Volt$_B$

Figure 12 shows the two-dimensional calibration data plotted with the computed bending moments from the applied calibration matrix above. The dashed lines represent the 95% prediction bands for the calibration matrix. All load cells were digitized on both the low and high frequency NI digitizers, Chassis 1 and Chassis 2. All load cell leads were routed along the hollow

23

drive shaft through a Fabricast Inc. custom 36 channel slip ring assembly (part# 8221-2.002-33-36U/S) located forward of the dynamometer.
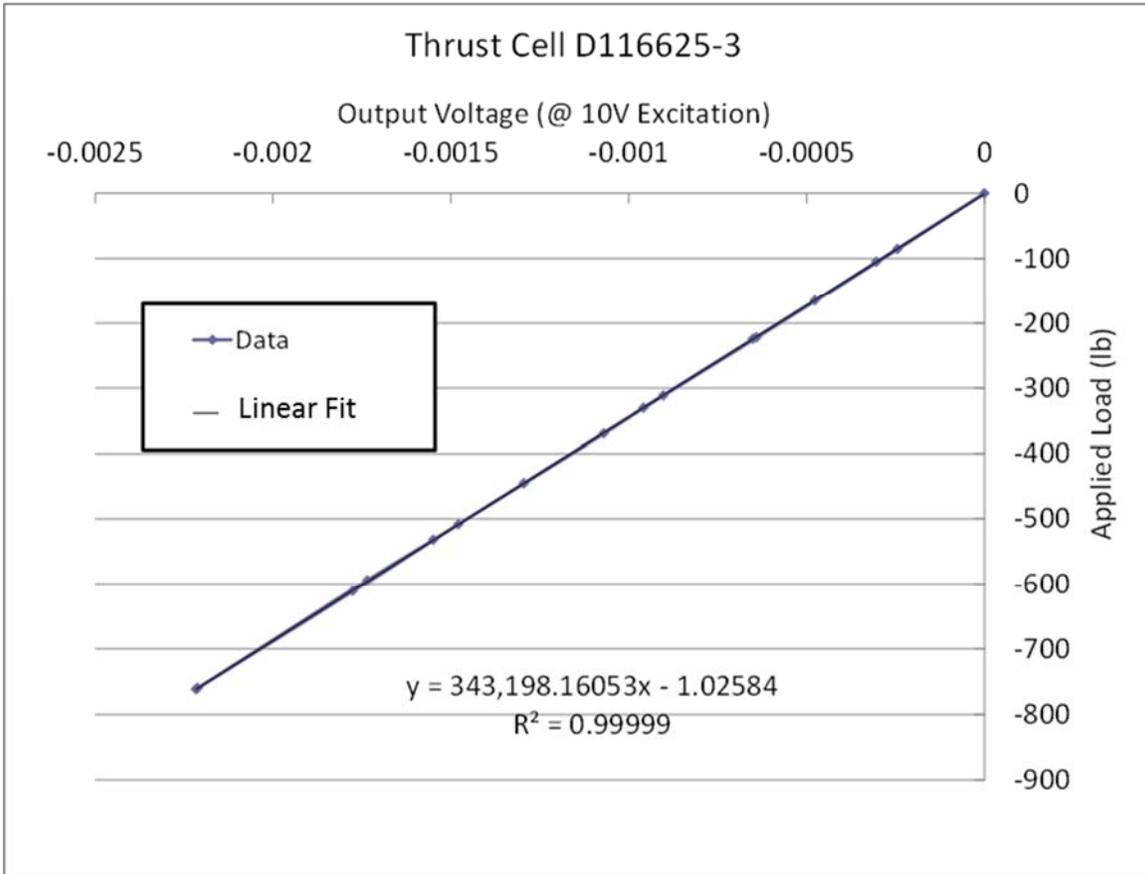
Figure 11. ARL thrust cell calibration.
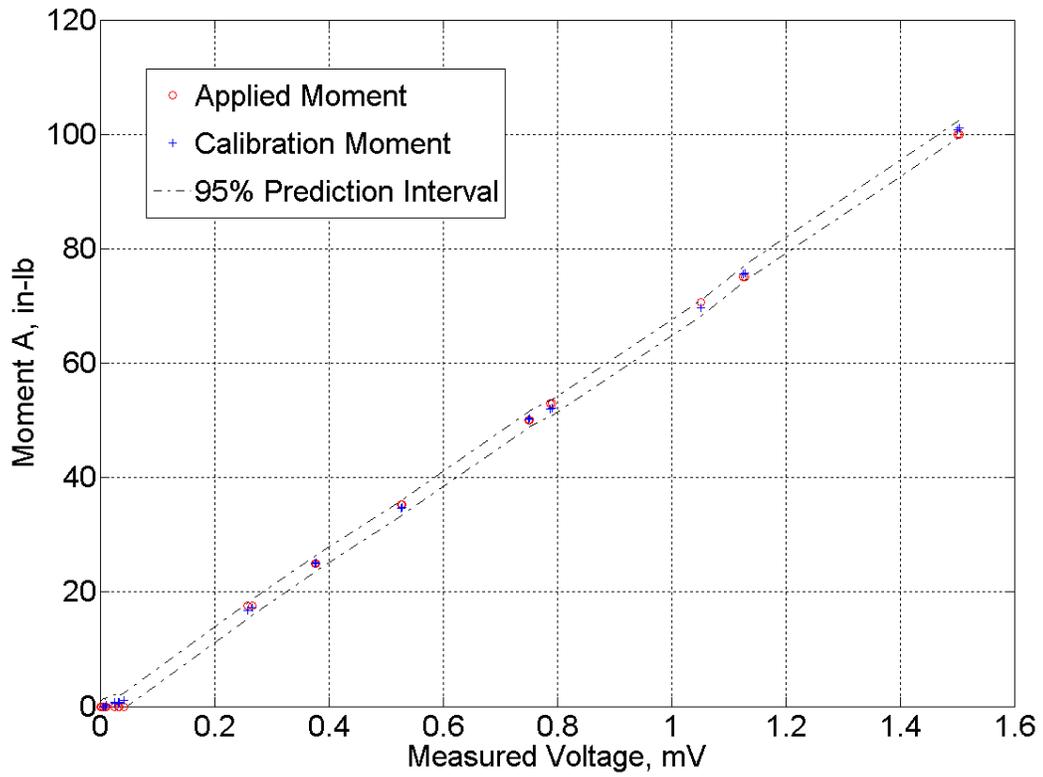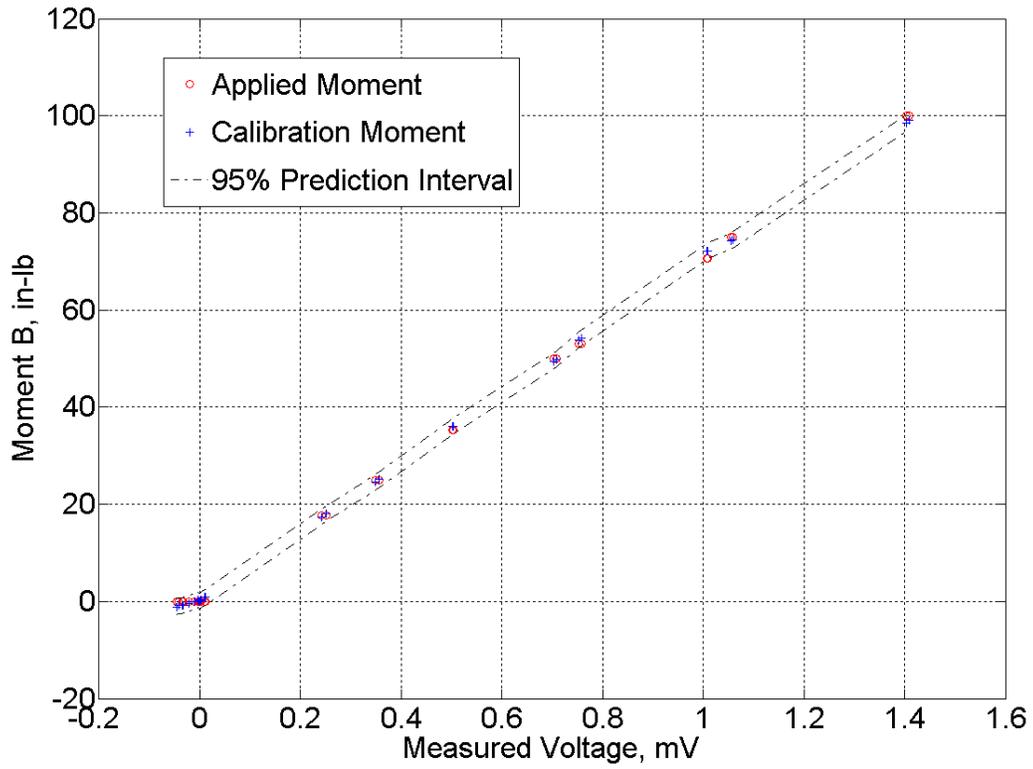
Figure 12. Bending moment calibration with estimated prediction intervals. a) Moment A, b) Moment B.

High Frequency Pressure and Vibration

High frequency, unsteady pressures were measured with PCB 105M147 quartz transducers mounted on the leading edge of the tower at four locations, 42%, 74%, 106% and 117% blade span. The transducers were positioned to measure the unsteady pressure signature associated with the blade, blade wake and tip vortex interaction with the tower. Tower – Nacelle vibration was measured with a PCB J356B07 Triaxial accelerometer mounted at the tower nacelle junction. The accelerometer is used to separate mechanical vibration from the pressure signals. All transducers were factory calibrated. The pressure and accelerometer signals were digitized at 4 kHz with the high frequency NI system (chassis 2). The tower/nacelle sensor leads were routed out the tower through the center road side window the tower was mounted on. Transducer calibrations are provided in Table 6. These sensors have a typical high pass frequency of 1.5 Hz so no steady pressure can be obtained.

Table 6. High frequency pressure and accelerometer calibrations.				
PCB 40% Span	PCB 40% Span	PCB 40% Span	PCB 40% Span	Triax Accel
3.04 mV/kPa	5.37 mV/kPa	5.08 mV/kPa	4.21 mV/kPa	100 mV/g

Blade Strain

Blade strain was measured using strain gage rosettes (Omega SGD - 2/350 - RY61) at two (2) spanwise locations (25% and 50% span) on Blade 2. The multi-component rosettes allow calculation of the local principal strains in the blade. In each rosette, Gage 2 was aligned along the blade span and components 1 and 3 were aligned as shown in Figure 13.
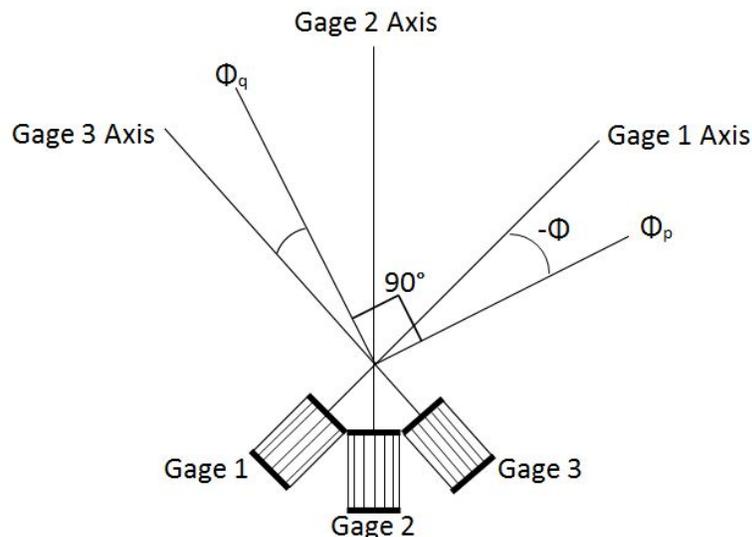
Figure 13. Strain gage rosette orientation and labeling.

The biaxial strain and stress field equations for the 0, 45 and 90 degree strain gauge rosettes used to describe the blade strains and stresses in the SANDIA rotor tests are defined as follows. The

26

principal strains are denoted by subscripts p and q in these equations. The post-processing routines include correcting the Gage Factor for lead length using:

$$F_{cor} = F\left(\frac{R_G}{R_G + R_L}\right)$$

where,
F= gage factor (provided by the manufacturer for this specific gage batch)
F_{cor} = corrected gage factor R_G = Gage resistance in Ohms
R_L= lead wire resistance in Ohms (measured).

The strain field in each gage is determined from the measured signal using:

$$\epsilon_n = \frac{4V_n}{V_{exc}F_{cor}}$$

where
V_n = Signal voltage in volts V_{exc} = excitation voltage in volts
F_{cor} = lead corrected gage factor ε_n= calculated strain from the signal voltage
 n = strain gage subscript (1, 2 or 3).

The principal strain field is calculated using the following equations:

$$\epsilon_p = \frac{\epsilon_1 + \epsilon_3}{2} + \frac{1}{\sqrt{2}}\sqrt{(\epsilon_1 - \epsilon_2)^2 + (\epsilon_2 - \epsilon_3)^2}$$

$$\epsilon_q = \frac{\epsilon_1 + \epsilon_3}{2} - \frac{1}{\sqrt{2}}\sqrt{(\epsilon_1 - \epsilon_2)^2 + (\epsilon_2 - \varepsilon_3)^2}$$

where
Subscript p designates the principal strain associated with gage 1 axis,
Subscript q designates the principal strain associated with gage 3 axis.

The principal stresses in the blade can then be calculated using:

$$\sigma_p = \frac{E}{2}\left[\frac{\epsilon_1 + \epsilon_3}{1 - v} + \frac{\sqrt{2}}{1 + v}\sqrt{(\epsilon_1 - \epsilon_2)^2 + (\epsilon_2 - \epsilon_3)^2}\right]$$

$$\sigma_q = \frac{E}{2}\left[\frac{\epsilon_1 + \epsilon_3}{1 - v} - \frac{\sqrt{2}}{1 + v}\sqrt{(\epsilon_1 - \epsilon_2)^2 + (\epsilon_2 - \epsilon_3)^2}\right]$$

where
σ_p = Principal stress associated with the gage 1 axis,
σ_q = Principal stress associated with the gage 3 axis,
E = Young's modulus = 197GPa,
v = Poisson's ratio = 0.272.

The principal axis orientation angle is then calculated from the following equation:

$$\phi_{p,q} = \frac{1}{2}\tan^{-1}\left(\frac{(\epsilon_2 - \epsilon_3) - (\epsilon_1 - \epsilon_3)}{\epsilon_1 - \epsilon_3}\right)\frac{180}{\pi}$$

$$\text{If} \quad \epsilon_1 = \frac{(\epsilon_1 + \epsilon_3)}{2} \qquad \text{then } \phi_{p,q} = \pm\, 45°$$

$$\text{If} \quad \epsilon_1 > \frac{(\epsilon_1 + \epsilon_3)}{2} \qquad \text{then } \phi_{p,q} = \phi_p$$

$$\text{If} \quad \epsilon_1 < \frac{\epsilon_1 + \epsilon_3}{2} \qquad \text{then } \phi_{p,q} = \phi_q$$

where,

$\Phi_{p,q}$ = is the angle of the gage 1 axis to the nearest principal axes. When the angle is positive the rotation is in the same direction as the gage numbering. When it is negative it is in the opposite direction of the gage numbering. The angle is in radians so the result has been multiplied by $180/\pi$ to get degrees. Please note the inverse tangent is undefined for ϵ_1 equal to ϵ_3. Angles ϕ_p and ϕ_q are always perpendicular to each other.

Acoustics

The turbine sound was measured by a hydrophone embedded in a paraboloid housing that was mounted to the outside of the middle tunnel window. Both the water tunnel window and hydrophone housing were made of acrylic (density=1190 kg/m^3 and bulk sound speed of 2750 m/s). The window was 44 mm thick. The diameter of the housing was 118 mm and the depth was 43 mm. The hydrophone focus was located 20 mm from the vertex which makes it 23 mm from the outside of the window. The hydrophone, a Reson TC 4013, was embedded into the housing and distilled water was poured around the hydrophone and sealed to assure water contact between the hydrophone and the acrylic. The freefield sensitivity of the hydrophone is nominally -200 dB re 1 V/µPa. With the housing the pressure level was amplified as will be shown later. The housing was clamped to the window with a layer of silicone based jelly between the housing and window to avoid any air bubbles.

The hydrophones were calibrated using an in-situ method. In this method, a spherical hydrophone was placed in the same location as the turbine and excited with a voltage to generate a known radiated acoustic power. An International Transducer Corporation (ITC) Model 1032 source was used. The transmitting response of the hydrophone is shown in Figure 14. For this experiment, the source was located at a radius of 206 mm (70 percent of the turbine tip radius or 33.7 percent of the test-section radius). The sampling rate of the analyzer is 204.8 kHz. The maximum frequency is 100 kHz. The maximum frequency is below the Nyquist frequency. The bandwidth is 12.5 Hz providing ensemble period is 0.08 s. With taking 2000 ensembles, the total acquisition time is at least 160 s. The random errors are provided by Bendat and Piersol, (Engineering Applications of Correlation and Spectral Analysis, John Wiley & Son, 1980, p. 274). The normalized random errors are for the autospectrum is 0.0224 or less than 0.1 dB.

To provide a spatial average the source was kept at the constant radius but positioned to (45, 135, 225, and 315) degrees from vertical with positive angle being clockwise looking downstream. Figure 15 shows the voltage response of the window hydrophone to the source for the four angular locations. The black curve shows the linear mean response and the cyan curve shows the background level for a typical position without the source on. Figure 15 shows humps in spectra every 10 kHz. This is caused by the wave amplification of the acrylic due to its finite radial extent

and the material property change from that of water. Additionally, there is a small fluctuation in the amplitude at periods less that 1 kHz. This is caused by the radial modes set up cross-wise in the tunnel due to its 1.22 m diameter.
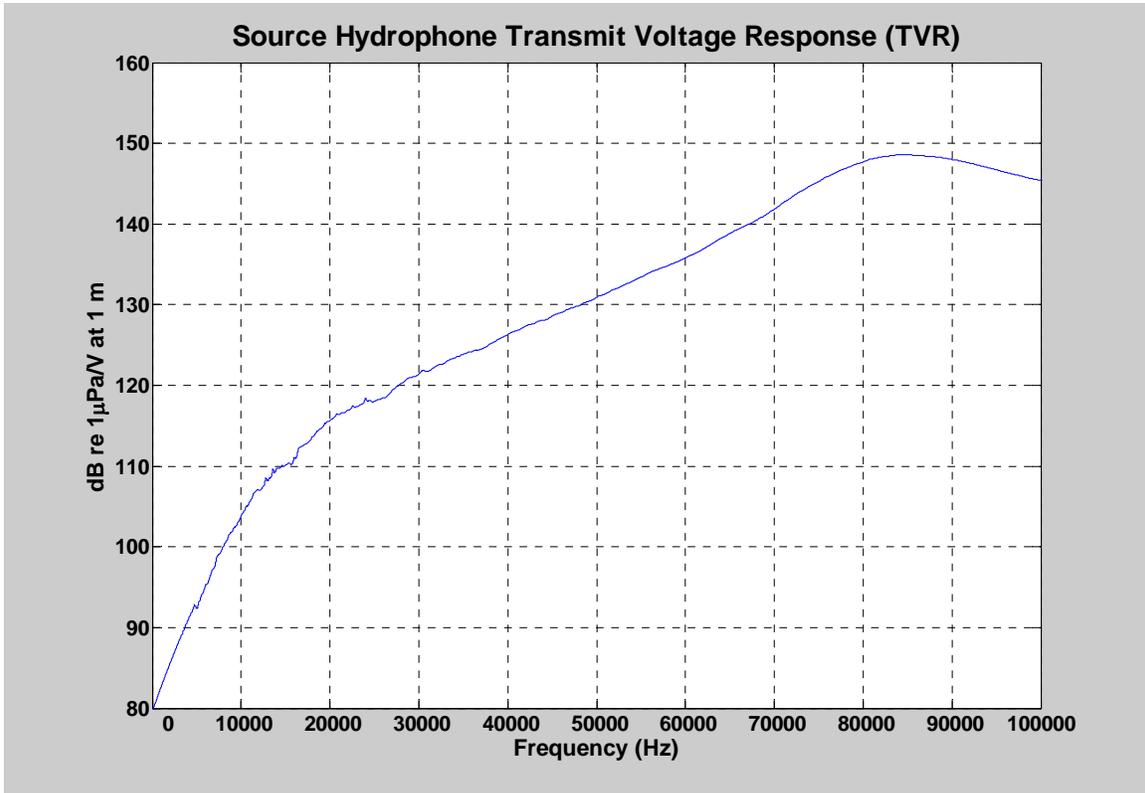
Figure 14. Transmitting response for the ITC 1032 hydrophone.
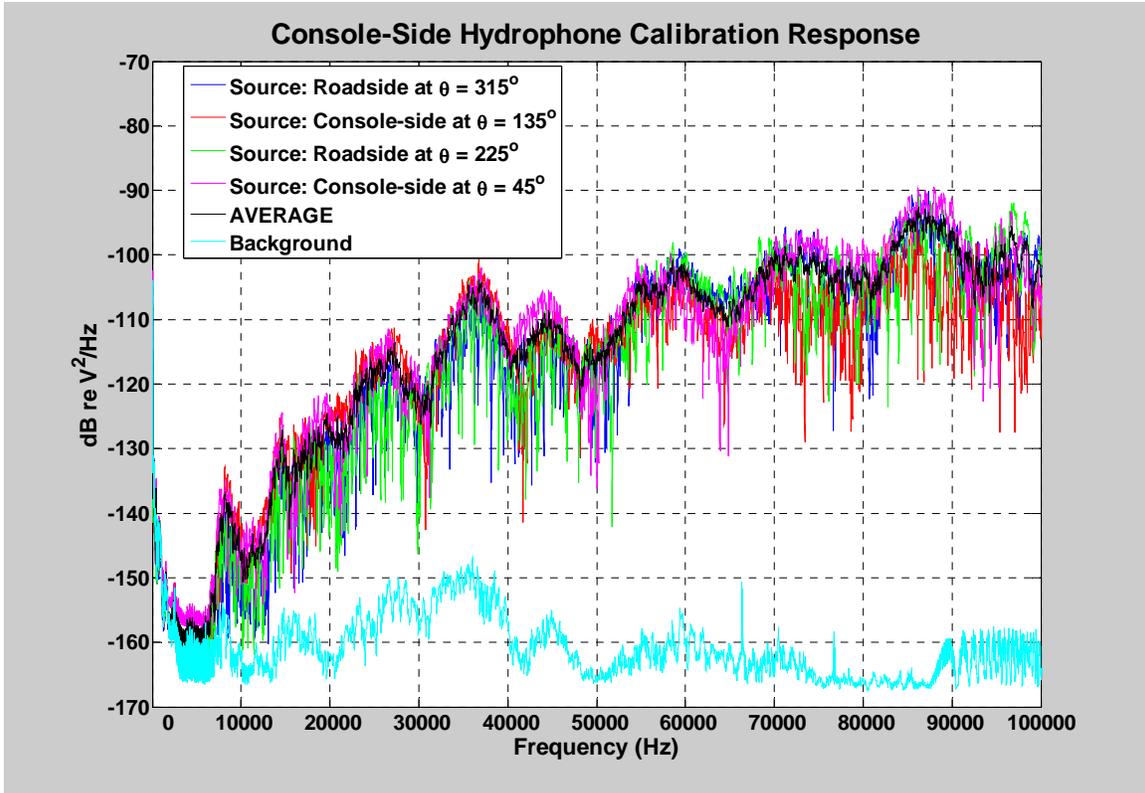
Figure 15. Window hydrophone response to various calibration sources.

Figure 16 shows the final calibration curve S_{WH} used to process the radiated sound from the turbine.

$$S_{WH} = V_{WH} - V_S - TVR_S$$

Here V is the autospectrum of voltage in dB and TVR is the transmit voltage response. The subscripts WH and S are the window hydrophone and source, respectively. All the levels are in dB. The curve continues to show the humps separated by about 10 kHz and smaller fluctuations associated with tunnel cross modes. Comparing the calibration curve to the nominal sensitivity of a freefield receiving sensitivity shown in blue indicates that the parabolic nature of the hydrophone housing increases its sensitivity.
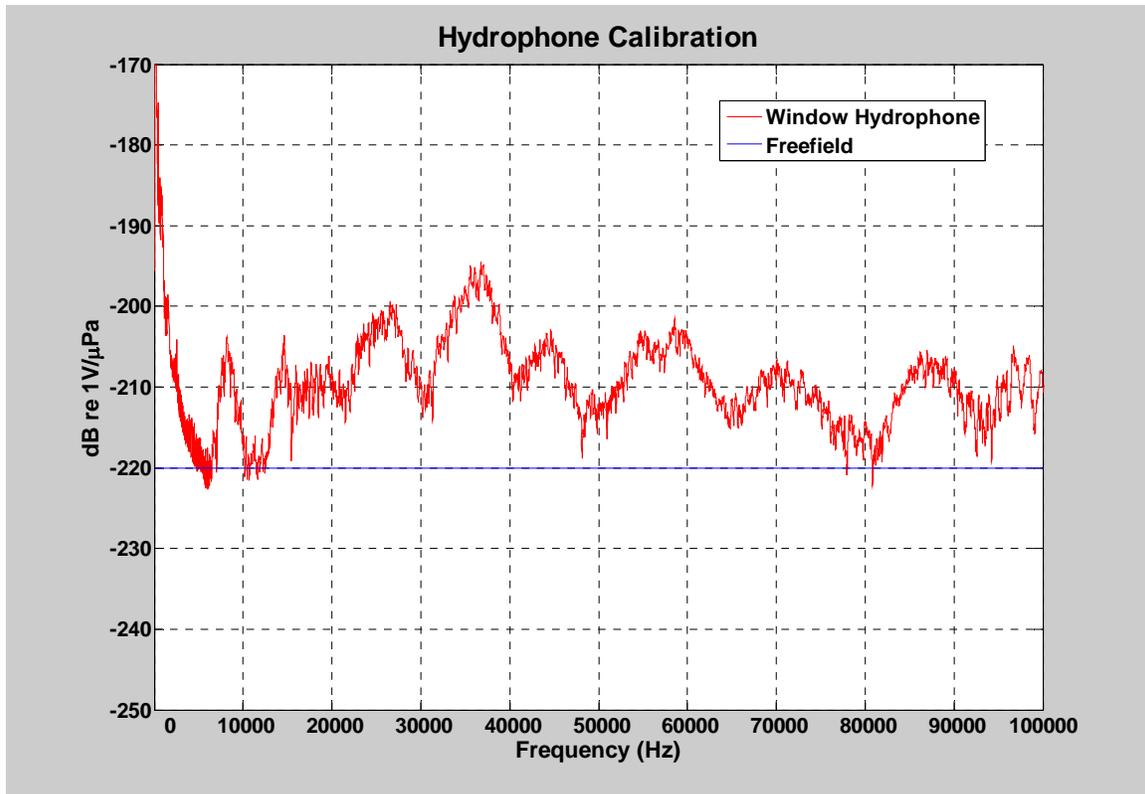
Figure 16. Average calibration curve for window hydrophone.

Cavitation Assessment

Cavitation tests were conducted on the Sandia rotor in the 48 inch GTWT water tunnel test. Tests included cavitation inception on each blade for a variety of types of cavitation as well as cavitation breakdown (i.e., degradation in rotor torque due to cavitation on the blades). Cavitation inception is defined at the pressure for which the earliest visual signs of inception occurred.

The cavitation test was conducted in the following manner: the operating condition (velocity and RPM) was fixed and the freestream pressure was raised to 310kPa (45 psia), the maximum allowable pressure for this specific test set-up due to window limitations. The pressure was then slowly and systematically lowered until cavitation was observed visually. The pressure and cavitation type were then recorded. The pressure was then systematically raised in a similar manner until all visual signs of cavitation abated. This is termed, cavitation desinence and is generally considered more conservative for design performance estimates. In this test series, inception and desinence were found to occur at similar pressures, so only inception values are reported. A video record was also acquired during the test.

The tests were conducted on two separate days, the first of which included a general overall test of the rotor for inception and breakdown, and the second test comprised a look at the individual blades for the various forms of cavitation. The total dissolved air content of the tunnel water was measured at 7.2 molar parts per million for the first test (overall rotor) and 6.4 molar ppm for the second (individual blade) test. ARL has a long established and documented history of performing

31

cavitation tests on different turbomachinery devices. The procedures, such as the gas content used to perform a water tunnel cavitation tests, are well accepted in the propeller community.

In the first test, four discrete velocities were specified (3, 4, 5, and 6 m/s) and the rpm was varied accordingly to produce TSRs of 3.8, 4.0, and 4.2. At the two higher velocities (5 and 6 m/s), it was impossible to suppress cavitation in the tip vortex at the maximum operating pressure of 310 kPa (45 PSIA), so no inception data were available. A video record of the cavitation performance was recorded for each test condition. Follow-on tests could be conducted with different tunnel windows for higher tunnel static pressure and at lower gas content to attempt to suppress cavitation at higher velocities.

The second test was conducted at a single TSR of 4.0, corresponding to a tunnel velocity of 4 m/s and a rotor rotational speed of 531 rpm. In this test series, the inception and further developed cavitation points were measured on an individual blade basis for each of the three blades.

Results

Test Matrix

Table 6 lists the test matrix summary during the November-December 2012 test entry in the ARL 48-inch diameter water tunnel. The primary powering tests were performed in tests 3487, 3492 and 3514. Freewheeling tests were performed in test # 3517. Powering data were recorded throughout the test program with multiple repeat data sets at the design condition of U = 5 m/s, TSR =4. Cavitation measurements were conducted in test # 3488 and 3507. Acoustic measurements were performed in the November 26-29 period, test #s 3509-3511. The remainder of the test period was allocated to flow field mapping with LDV and PIV as outlined in Table 7. Analog acquisition of powering, drive shaft loads, pressure, vibration and tunnel conditions was performed throughout the test. High frequency acquisition of the ARL thrust and torque cell, sufficient to resolve the unsteady drive shaft thrust and torque, was initiated in Test # 3496. Prior to this test, the ARL thrust and torque cells were digitized on a high resolution NI DAQ card with <1Hz acquisition rate for high resolution steady acquisition. The tunnel wall static pressure at the axial location 2.235 m (88") from the test section upstream flange was added to the data base in test # 3496 to provide an additional pressure measurement downstream of the turbine.

Table 7. Test Matrix Summary.		
Date	**Test #**	**Comments**
6-Nov-12	3484	Shakedown, bare hub LDV - Inlet profiles
		Torque via Dyne = 5.96 N-m (4.4 lb-ft) zero tare, Model Pressure = 13.8 kPa (2 psid)
		2. CSL 80 static tap

	3485	Turbine model install & shakedown
	3486	Powering shakedown
7-Nov-12		Tunnel conditions:
		Run 1: Vinf = 5 m/s, rpm = 332
		Run 2: Vinf = 2 m/s, rpm = 133
		Run 3: Vinf = 7 m/s, rpm = 930
	3487	Powering Test
		Air Content = 13.3 ppm
		Zeros taken: Dyne Q = 5.97 N-m (4.4 lb-ft) zero tare
		Run 2-34: Vinf = 2 m/s
8-Nov-12		Runs 35-46: Vinf = 5m/s
		Runs 48-55: Vinf = 7m/s
		Tunnel put on Bypass to lower air content for Cavitation Test
	3488	Cavitation Test
		Air Content = 7.22 ppm at start of test
		Air Content = 7.3 ppm at end of test
	3489	Flow field mapping: LDV Survey
		X=134.6 mm downstream (DS) of Rotor hub LE, Survey SNL_LDV_X135Radial_Encode
		Tunnel Conditions: Vinf= 5 m/s, 310.3 kPa (45 psia), 664 rpm
		data point taken approximately every 15 minutes
9-Nov-12		Run 4 - 300 seconds of data
	3490	Flow field mapping: LDV Survey
		X=134.6 mm DS of Rotor hub LE, Survey SNL_LDV_X135Radial_Encode expanded
		Tunnel Conditions: Vinf= 5 m/s, 310.3 kPa (45 psia), 664 rpm
		data point taken approximately every 15 minutes
	3491	Flow field mapping: LDV Survey - Rotor inflow
		X=-17 mm upstream (US) of Rotor hub LE, Survey SNL_LDV_Inflow_X-17_Encode
		X=-800 mm US of Rotor hub LE, Survey SNL_LDV_Inflow_X-800
		Tunnel conditions: Vinf = 5 m/s, 310.3 kPa (45 psia), rpm 664
12-Nov-12		Air Content = 10.08 ppm
	3492	Powering test
		Runs 1-11: 2 m/s
		Runs 12-15: 5 m/s
		New stolab SN7730 installed in tunnel for tunnel temperature
		SN7730 Calibrated 25 October 2012

Date	Run	Description
	3493	Torque cal check
	3494	Flow field mapping: LDV Survey
		X=215.9 mm DS of Rotor hub LE, Survey SNL_LDV_X216_Radial_Encode
13-Nov-12		X=574 mm DS of Rotor hub LE, Survey SNL_LDV_X574_Radial_Encode_console
		Air Content = 10.9 ppm
		Tunnel Conditions: Vinf = 5 mps, 310.3 kPa (45 psia), 664 rpm
		Note: Strain 1 on mid span rosette failed (run 5)
	3495	Flow field mapping: LDV Survey - tower wake
	3496	X=249.9 mm DS of Rotor hub LE, Survey SNL_LDV_X250_Radial_Encode_TowerWake
14-Nov-12		Static Tap - RU 88 in DXD 78 ~3.45 kPa (0.5 psi) low
		Tunnel Conditions: Vinf = 5 m/s, 310.3 kPa (45 psia), 664 rpm
		Add Static tap P88 to data set
		Add ARL T & Q to high frequency acquisition (TDMS files)
		Performing dynamic force calibration.
	3497	Flow field mapping: PIV Survey - Proximal to rotor
15-Nov-12		US of Rotor, Mapping SNL_TURB_UP_Y0: Y=0, X-Zplane
		US of Rotor, Mapping SNL_Turb_UP_Y-3: Y=-76.2 mm (3"), X-Zplane
		Tunnel Conditions: Vinf = 5m/s, 310.3 kPa (45 psia), 664 rpm
	3498	Flow field mapping: PIV Survey - Proximal to rotor
		DS of Rotor, Mapping SNL_Turb_DS_Y0: Y=0, X-Zplane
		US of Rotor, Mapping SNL_Turb_Upwideview_Y0, X-Z plane
16-Nov-12		camera tilted (12.4 degrees up) for large FOV
	3499	US of Rotor, Mapping SNL_Turb_UP_Y2, Y=50.8 mm (2"), X-Z plane
	3500	DS of Rotor, Mapping SNL_Turb_DS_Y-1p5: Y=-38.1 mm (1.5"), X-Zplane
		DS of Rotor, Mapping SNL_Turb_DS_Y-4: Y=-101.6 mm (4"), X-Zplane
		Tunnel Conditions: Vinf = 5m/s, 310.3 kPa (45 psia), 664 rpm
	3501	Flow field mapping: PIV & LDV Survey - tower Wake Road side DS glass window
19-Nov-12	3502	LDV survey: Repeat of X=249.9 mm DS of Rotor hub LE, Survey SNL_LDV_X250_Radial_Encode_TowerWake
		Bending moment A load cell went - most likely wet.
20-Nov-12	3503	Flow field mapping: SPIV Surveys - DS of rotor. LDV surveys RS glass window
		Stereo Piv 1: Mapping SNL_Turb_Stereo1_Tip

		LDV survey: Repeat of X=249.9 mm DS of Rotor hub LE, Survey SNL_LDV_X250_Radial_Encode_TowerWake
		Tunnel Conditions: Vinf = 5 m/s, 310.3 kPa (45 psia), 664 rpm
		Stereo Piv 2: Mapping SNL_Turb_Stereo2_Tip_Lowspeed
		Tunnel Conditions: Vinf = 4 m/s, 310.3 kPa (45 psia), 531 rpm
21-Nov-12	3504	Flow field mapping: SPIV Surveys - DS of rotor. LDV surveys tower wake 1D DS
		Stereo Piv 2: Mapping SNL_Turb_Stereo2_Tip_Lowspeed - finish mapping at different phase angles
		Tunnel Conditions: Vinf = 4 m/s, 310.3 kPa (45 psia), 531 rpm
	3505	Stereo Piv 3: Mapping SNL_Turb_Stereo3_Hub
		LDV survey: X=574mm Survey SNL_LDV_X574_Radial_Encode_TowerWake
		Tunnel Conditions: Vinf = 5 m/s, 310.3 kPa (45 psi), 664 rpm
26-Nov-12		Install hydrophones: 1) RS diffuser window, 2) CS middle window, 3) Hatch
	3506	Flow field mapping: SPIV Surveys - DS of rotor.
		Stereo Piv 4: Mapping SNL_Turb_Stereo4_Tip
		Tunnel Conditions: Vinf = 5 m/s, 310.3 kPa (45 psi), 664 rpm
		Hub rosettes- suspected short, power supply "B" off
	3507	Cavitation Test
		Air Content = 17.85 ppm at start
		On Bypass
		Air Content = 12.15 ppm
		Air Content = 8.11 ppm
		Off Bypass
		Air Content = 6.4 ppm
		Tunnel Conditions: Vinf = 4 m/s, 531 rpm
27-Nov-12	3509	Acoustics Meas.
		Air Content = 8.2 ppm
		On Bypass
		Air Content = 3.7 ppm

		Off Bypass
		Air Content = 3.3 ppm
		Zeros at 137.9 kPa (20 psia)
		Zeros at 310.3 kPa (45 psia)
		Runs 1-15: tank hydrophone 1.517 m (59.75") from front edge and 1.206 m (47.5") from back edge of tank.
		Run 16: tank hydrophone at 0.762 m (30")
		Run 17: tank hydrophone at 2.184 m (86)
		Run 18: tank hydrophone at 1.517 m (59.75")
28-Nov-12	3510	Acoustic Meas: Change rotor - install bare hub
		Air Content = 5.6 ppm
		On Bypass
		Off Bypass
		Air Content = 3.3 ppm
29-Nov-12	3511	Acoustic In-situ Calibration
		Finish install of source for acoustic cal
		Zeros
		Run 1: hydrophone at 1.517 m (59.75")
		Run 2: hydrophone at 0.762 m (30")
		Run 3: hydrophone at 2.032 (80")
		Offline
		Drain - rotate source
		Online
		Offline
		Drain - remove sources - install windows
		Online
	3512	LDV field mapping: LDV Surveys - 1D DS of rotor plane - Bare Hub Tower wake
		LDV survey: X=75mm Survey: SNL_LDV_BareHubInflow_X75_TowerWake
		Tunnel Conditions: Vinf = 5 m/s, 310.3 kPa (45psia), 664 rpm
		Install rotor
30-Nov-12	3513	LDV field mapping: LDV Surveys - PIV flow maping locations
		LDV survey: X=64mm Survey: SNL_LDV_X64_Radial_Encode
		Tunnel Conditions: Vinf = 5 m/s, 310.3 kPa (45psia), 664 rpm
		Air Content = 12.1 ppm
	3514	Powering Test and PIV flow Mapping at 1D DS of rotor
		PIV Mapping : SNL_Turb_1DiamDS
		Runs 2-6: Vinf = 2 m/s, 310.3 kPa (45 psia)

		Runs 7-11: Vinf = 3 m/s, 310.3 kPa (45 psia)
		Runs 12-16: Vinf = 4 m/s, 310.3 kPa (45 psia)
		Runs 17-21: Vinf = 5 m/s, 310.3 kPa (45 psia)
	3515	Powering repeat
	3516	LDV field mapping: LDV Surveys - PIV flow maping locations
		LDV survey: X=89mm Survey: SNL_LDV_X89_Radial_Encode
		Tunnel Conditions: Vinf = 5 m/s, 310.3 kPa (45psia), 664 rpm
	3517	Freewheel test
		At 2 m/s not freewheeling
3-Dec-12		After Run 3 - moved rotor via dyne system to 200 rpm. Commanded zero rpm. Now freewheeling
		Run 4: Freewheeling
		Run 8: Coming to zero
		Run 9: Data = 150 seconds, speed up until break over then go to zero - dynamic test on freewheeling
		Drain - remove hatch - prep for flow vis
	3518	Flow Vis - mini-tuffs on tower and surface paint of rotor
		not able to zero due to Flow Vis

Power Performance

Figure 17 and Figure 18 show the mean powering data, C_P, C_T and C_Q measured for the rotor at 5 different inflow speeds and varying TSR without and with the blockage correction described earlier. The 2 m/s powering measurements in Test # 3487 were determined to be biased due to a zero drift and possible bearing friction. The black lines in Figure 17 and Figure 18 represent the low order performance predictions from the rotor design described earlier [31]. These low order predictions do not incorporate the tower but do provide a nacelle correction. The red dotted lines are Reynolds Averaged Navier Stokes (RANS) computational fluid dynamics (CFD) simulations performed at ARL of the in-tunnel rotor test. The CFD simulations were conducted with the model the rotor in the tunnel without the tower.

Figure 17 shows the actual tunnel data measured and uncorrected for blockage in the tunnel. Good agreement is observed between the CFD and measured data for C_P and C_Q. The measured C_T curves are low due to blade tower effects, as will be described later. The measured data are higher than the BEM predictions, which are for a free field performance, as expected due to tunnel blockage. The model – tunnel blockage, defined by the ratio of the rotor/nacelle/tower frontal area to the cross-sectional area of the tunnel, is ~ 5%. This blockage should produce a higher torque and power measured in the tunnel relative to the free-field due to an increased mass flow through the rotor by the wall-confined streamlines.
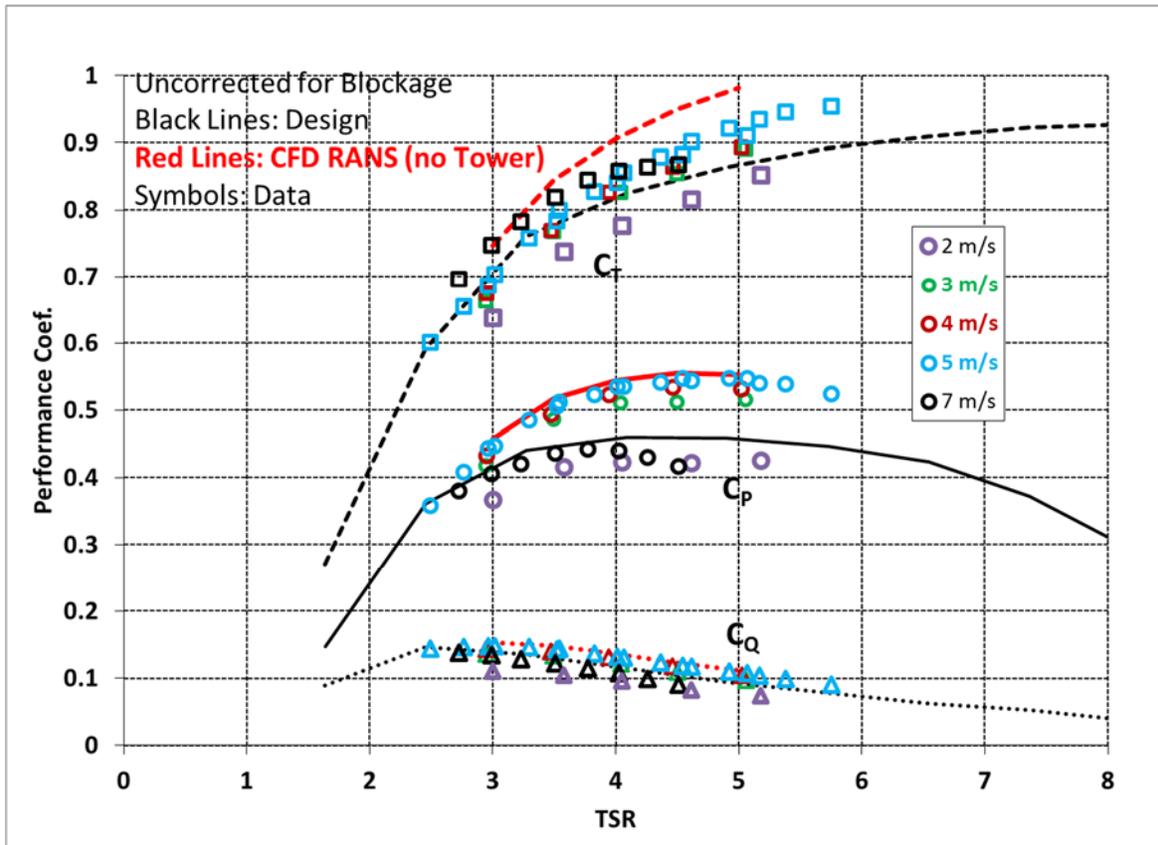
Figure 17. Dimensionless powering coefficients measured in the tunnel without a blockage correction.

Figure 18 shows the blockage corrected [21] powering performance data measured with the turbine model. Calculated blockage corrections ranged from 6% to 9% depending on inflow speed and TSR. The blade loadings and powering data are inline with expectations from the BEM calculations, except for results at 2 and 7 m/s. The differences at 2 m/s can be explained by most likely Reynolds number effects. The 7m/s data is low due to cavitation breakdown as discussed later in the report. The 3, 4, and 5 m/s data is cavitation-free on the blades. Overall, excellent agreement is observed between the measured performance and the low-fidelity model predictions, despite the unconventional design features of this rotor. All bias corrections are accounted for that the measured data will allow. Note that hub/nacelle and drive shaft components may not be exact geo-sims of the full-scale components and gap pressure induced load bias can be Reynolds number dependent.

An analysis was conducted to assess the effect of Reynolds numbers on the powering performance. Because the geometry and fluid properties were fixed during all of the testing, the change in velocity or TSR is analogous to a Reynolds number variation. Table 8 shows the blade chord Reynolds number Re_c as a function of tunnel velocity, V_{Tunnel}. It should be noted that blade chord profile thins as it approaches the tip, so the highest Reynolds number occurs closer to mid-span. Figure 19 and Figure 20 show the variation in measured C_Q and C_T for a constant *TSR* (of 3 and 4) as a function of velocities, respectively. In Figure 19, the C_Q values at lower velocities show some effect of Reynolds number and begin to level off at the higher velocities. The two highest

velocities measured in the test, 6 and 7 m/s, were influenced by the presence of cavitation which was unavoidable due to pressure limitations in the test, so those velocities are not shown. The increase of C_Q at the higher velocities represents an improvement in turbine efficiency. The values of C_T, shown in Figure 20, are shown to decrease slightly as velocity (or Reynolds number) increases. The effect is not as strong as that of C_Q. It appears that this blade geometry become roughly Re_c independent above ~350,000.
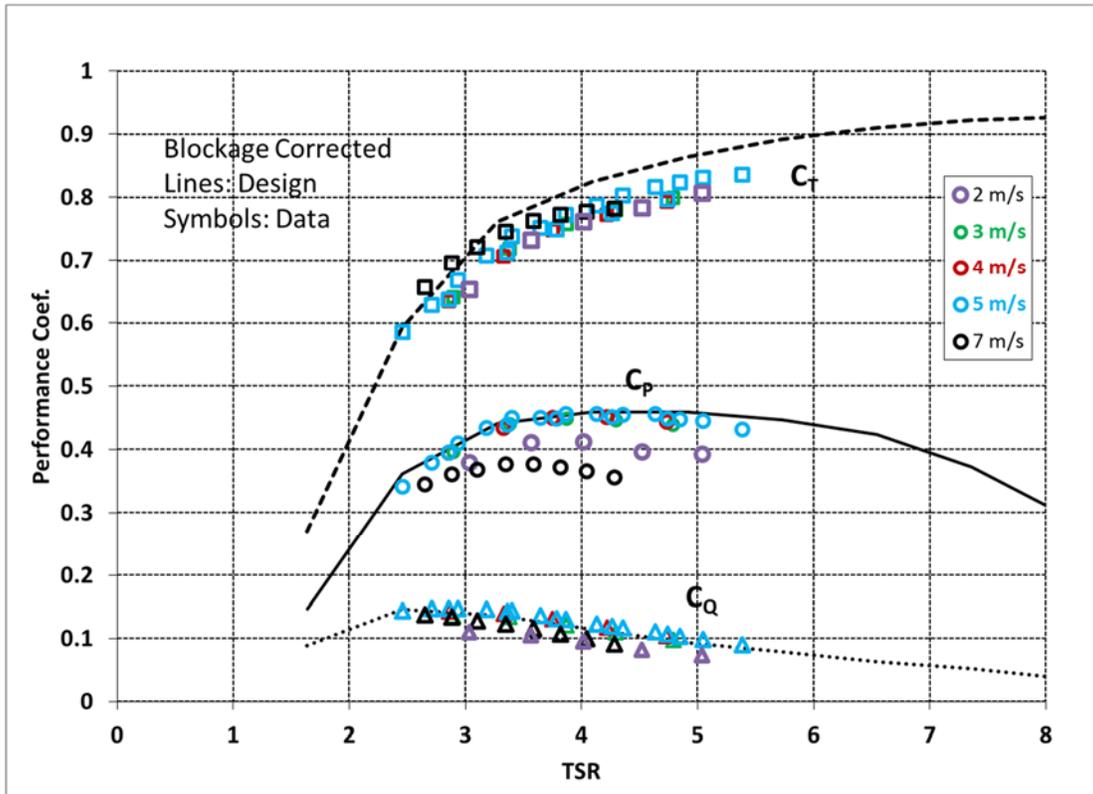
Figure 18. Dimensionless powering coefficients measured in the tunnel with blockage correction.

Table 8. Re_c versus tunnel speed.			
V_∞ (m/s)	Re_c (22% span)	Re_c (50% span)	Re_c (95% span)
2	208,871	232,882	198,221
3	313,307	349,323	297,332
4	417,742	465,764	396,442
5	522,178	582,205	495,553
6	626,613	698,645	594,663
7	731,049	815,086	693,774

39
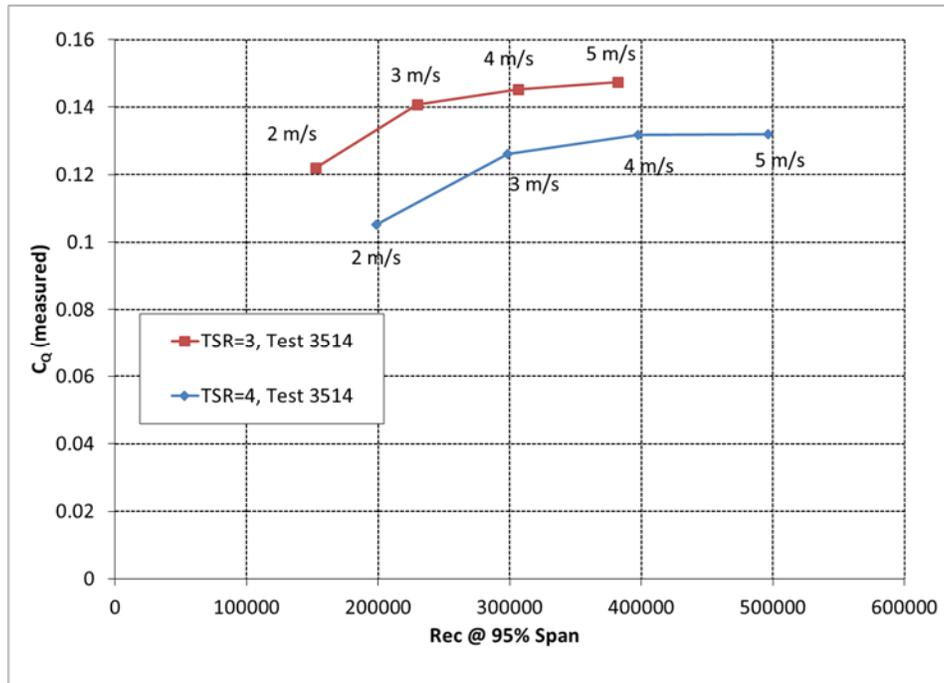
Figure 19. Measured C_Q as a function of Re_c at a constant *TSR* of 3 and 4 from Test 3514.
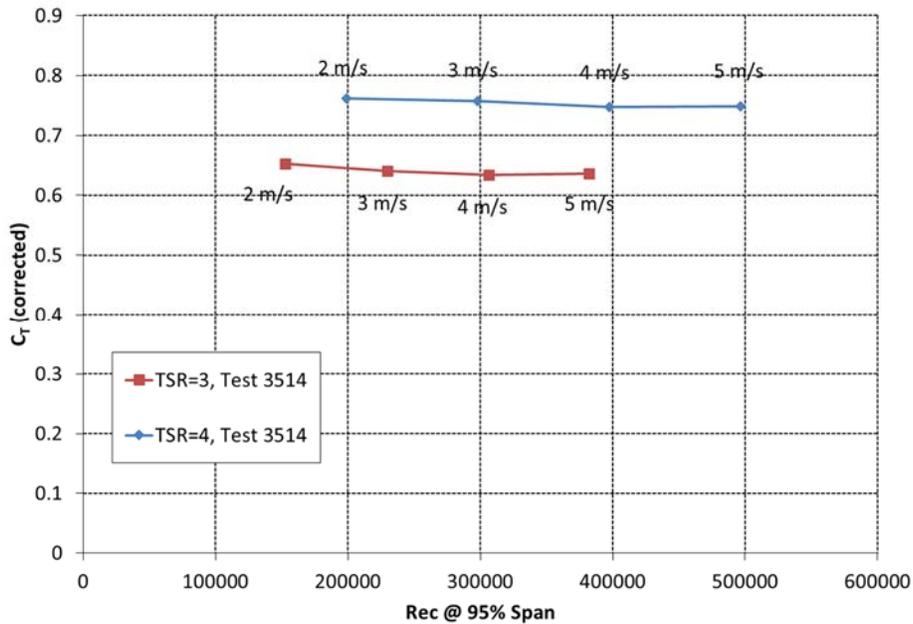
Figure 20. Blockage-corrected C_T as a function of Re_c at a constant *TSR* of 3 and 4 from Test 3514.

Cavitation Performance

Cavitation inception was defined at the pressure for which the earliest visual signs of inception occurred. Inception was defined as a cavitation event rate of 1-3 per second and this occurred sporadically at first. As the pressure was lowered, the cavitation in the tip vortex became steady

and was the first type detected (controlling form). The tip vortex cavitation was generally first observed approximately one tip chord downstream of the blade, Figure 21, and progressed upstream as pressure was lowered further (i.e. decrease in operating cavitation number) until the vortex cavitation was directly in contact with the blade, Figure 22. The next observed form with increasingly lower pressure was blade surface cavitation which appeared when the blade was very near its cavitation breakdown point. Cavitation breakdown is defined as the point for which the blade torque begins to decrease due to the formation of cavitation on the blade surfaces. A 3% decrease in rotor torque due to the presence of cavitation was where breakdown is defined for these tests. Figure 23 shows the early stages of blade cavitation on the edge of breakdown, and Figure 24 shows the blade in severe cavitation breakdown. Cavitation can be observed on the downstream face (suction side) of the turbine blade. Note that the camera position was changed for these photographs to allow visual access to the suction side of the turbine blades.

Figure 21. Photograph from Test 3488 of intermittent tip vortex cavitation inception downstream of the Sandia rotor, 4 m/s, 531 rpm, TSR=4, σ = 38.7.
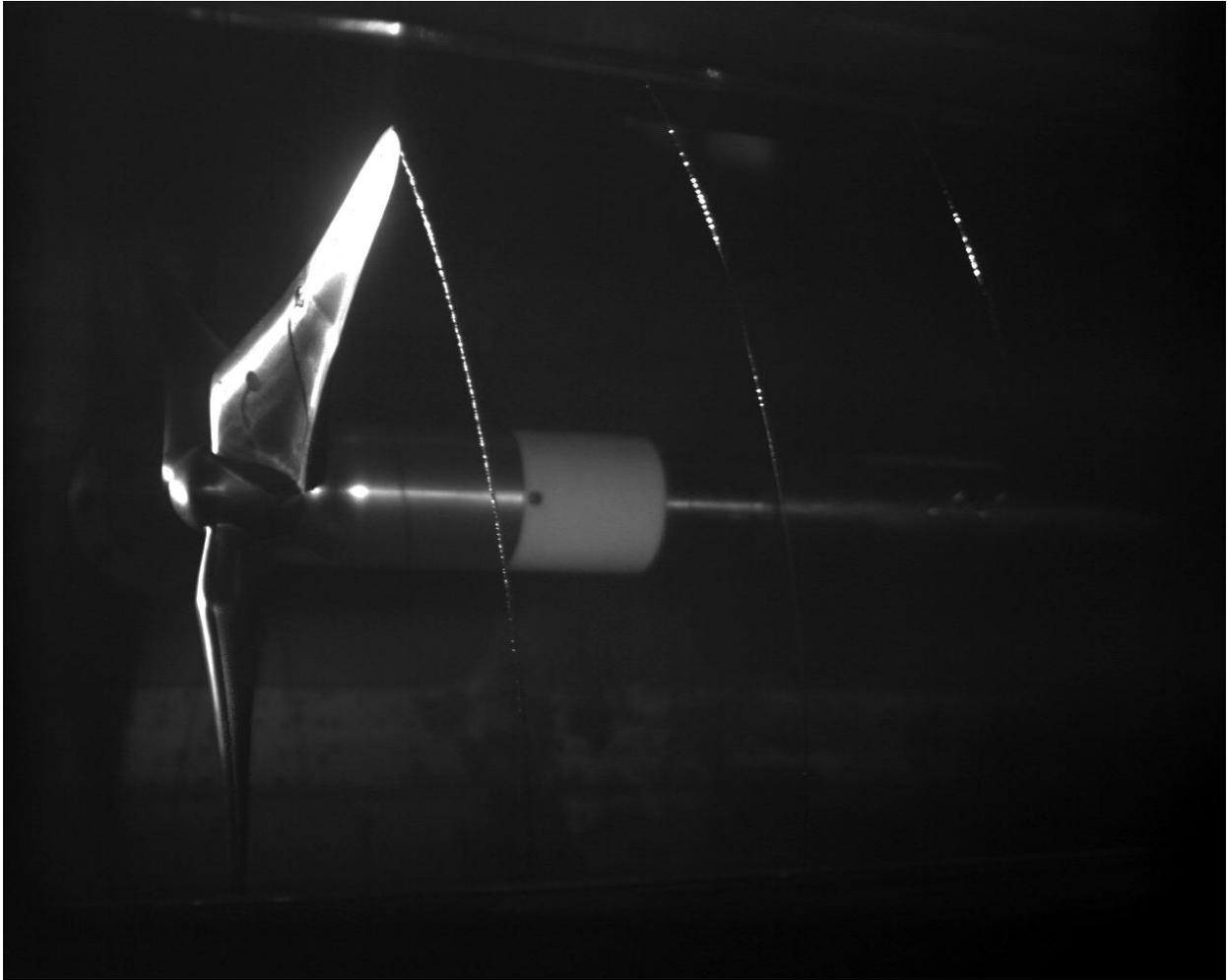
Figure 22. Photograph from Test 3488 of steady tip vortex cavitation on the Sandia rotor, 4 m/s, 531 rpm, TSR=4, σ = 25.7.
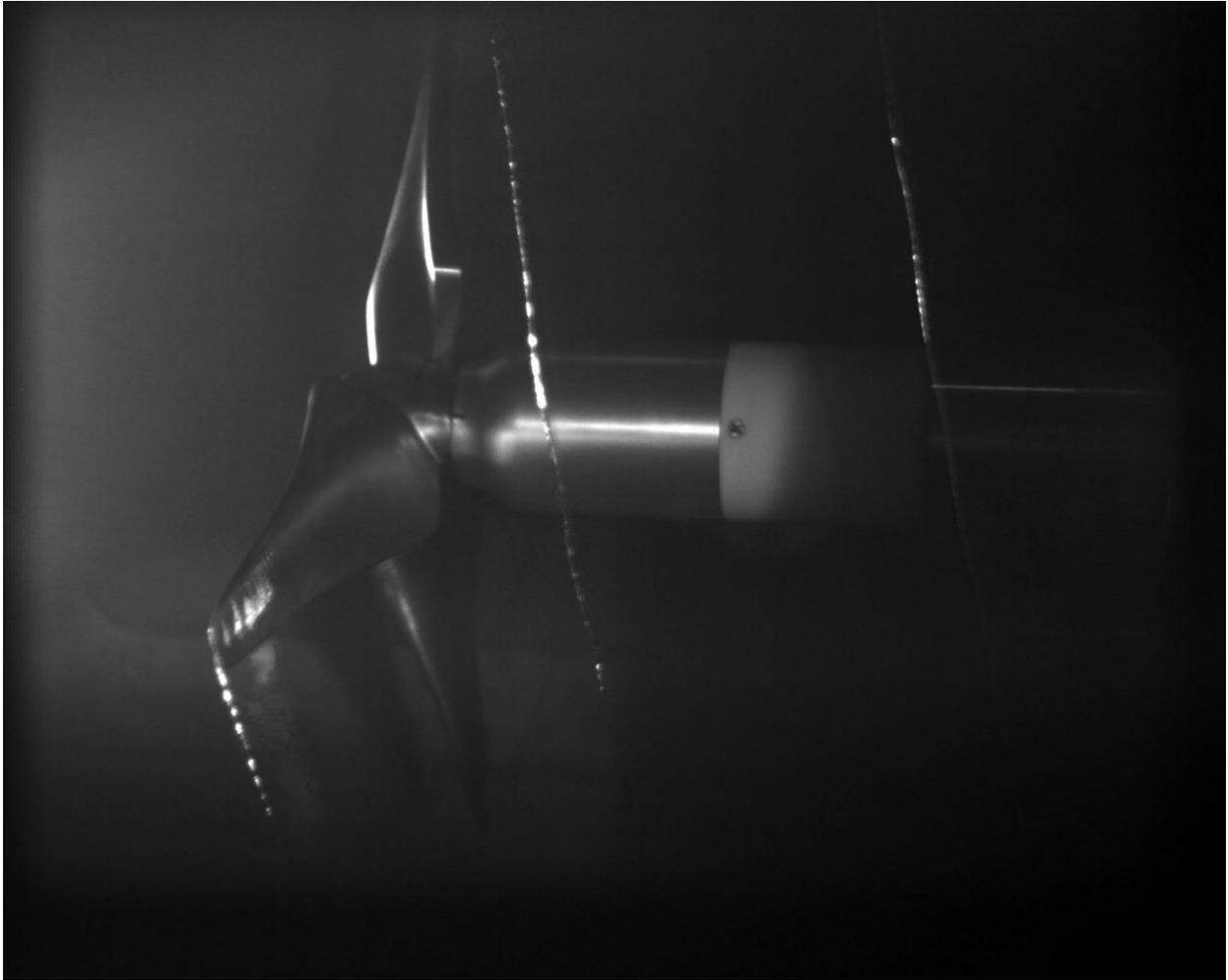
Figure 23. Photograph from Test 3488 blade cavitation inception on the Sandia rotor in a torque breakdown condition, 4 m/s, 531 rpm, TSR=4, σ = 17.

Figure 24. Photograph from Test 3488 developed blade cavitation on the Sandia rotor in a torque breakdown condition, 4 m/s, 531 rpm, TSR=4, σ = 14.8.

Figure 25 shows a plot of the model scale cavitation data from Test 3488 and 3507 for each form of cavitation at the 4 m/s condition. The data at 3 m/s showed similar results, and as mentioned earlier, the maximum pressure limitation (310.3 kPa (45 psia)) during these tests rendered it impossible to suppress cavitation at higher velocities, thus no measurement of inception was possible. The individual blade cavitation data from Test 3507 are shown superimposed on the plot in Figure 25 and they are included in tabular form in Table 9. The slight discrepancy in the inception points between the two tests represents a typical day-to-day variation in cavitation performance due to the dependence of cavitation on factors (e.g., nuclei content) that cannot be controlled.
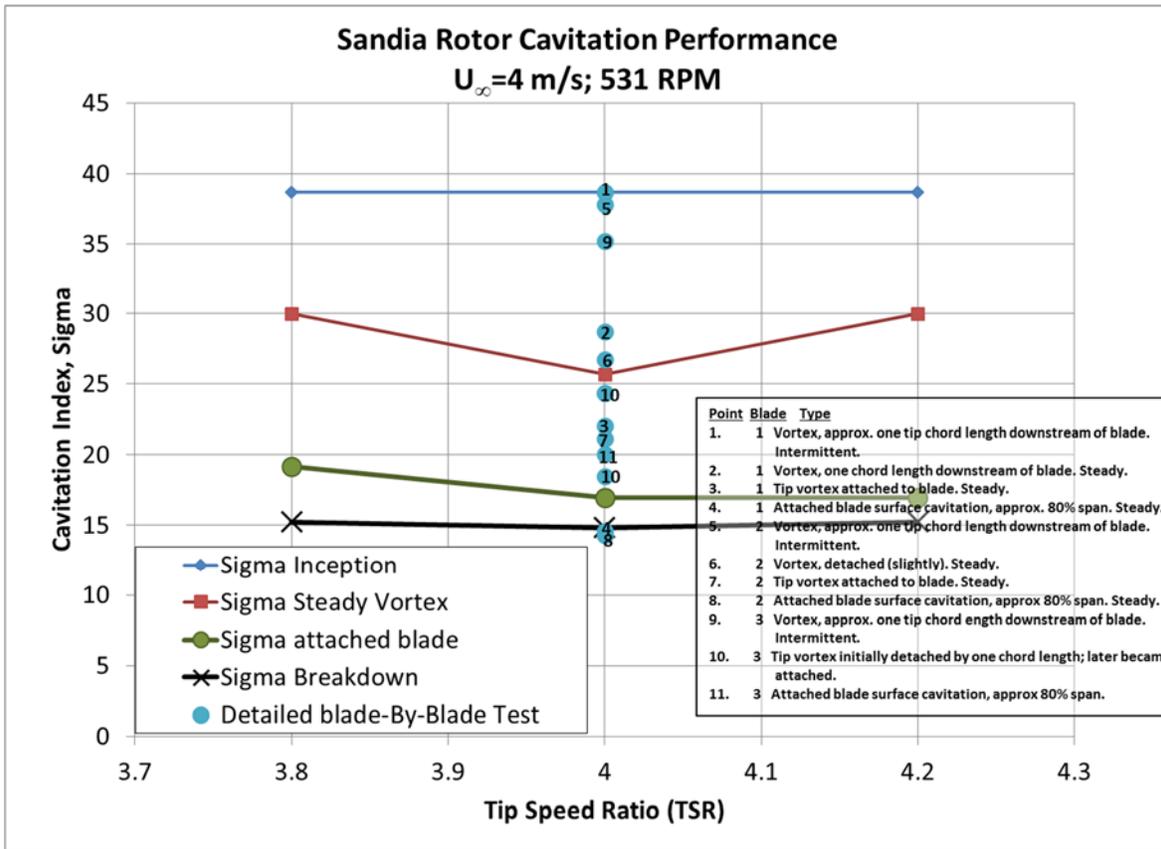
Figure 25. Plot of model scale cavitation data for overall rotor and individual blades.

Table 9. Tabular summary of Test 3507, individual blade measurements.						
Blade #	V_∞ (m/s)	Air content (ppm)	P_tunnel (KPa/ psia)	TSR	σ Model Scale	Notes
1	4	6.4	303.4/44	4	37.8	Vortex, intermittent, beginning approx. 1 chord (tip) length downstream of blade. Approx. 1 event/sec.
1	4	6.4	231/33.5	4	28.7	Vortex-steady. 1 chord length downstream of blade.
1	4	6.4	171/24.8	4	21.2	Steady tip vortex attached to blade.
1	4	6.4	162/23.5	4	20.0	Attached blade surface cavitation. Suction surface, approx 80% span.
2	4	6.4	310.3/45	4	38.7	Vortex, intermittent, beginning approx. 1 chord (tip) length downstream of blade. Approx. 0.2 event/sec.
2	4	6.4	215/31.2	4	26.7	Vortex, steady, detached (slightly)
2	4	6.4	177.9/25.8	4	22.0	Steady tip vortex attached to blade.
2	4	6.4	149.9/21.7	4	18.5	Attached blade surface cavitation. Suction surface, approx 80% span.

45

3	4	6.4	282.7/41	4	35.2	Vortex, intermittent, beginning approx. 1 chord (tip) length downstream of blade. Approx. 0.2 event/sec.
3	4	6.4	196.5/28.5	4	24.4	Tip vortex. Initially detached by one chord length. Later became attached to blade tip
3	4	6.4	196.5/28.5	4	24.4	repeat of above
3	4	6.4	118.6/17.2	4	14.6	Attached blade surface cavitation. Suction surface, approx 80% span. Intermittent.
3	4	6.4	116.5/16.9	4	14.3	Attached blade surface cavitation. Suction surface, approx 80% span. Steady.

The model scale tip vortex cavitation inception index was consistently in the range of 38-39 for all of the TSRs measured (3.8, 4.0, 4.2). While this cavitation value is unusually high (i.e., high susceptibility to cavitation) from experience at the GTWT, it is not surprising due to the high loading at the blade tips. That the cavitation index was relatively independent of TSR (albeit through a very limited measured range), indicates that cavitation inception was not highly dependent on the blade tip angle of attack. For the more developed states of a steady cavitating tip vortex, the best performance (i.e., the lowest σ) was seen at the on-design condition with slight degradation at the off-design points, which is the more typical "cavitation bucket" observed in pumps. The inception valves given in this report correspond to model scale data. Full scale performance predictions may require further scaling methodologies to correct for Reynolds Number differences and water quality effects between the current test conditions and fielded units.

It should be noted that the cavitation index for which breakdown occurred was typically less than half of where inception occurred. This is typical of what is observed on most turbomachines, where $\sigma_{breakdown}$ is roughly 30%-40% of $\sigma_{inception}$ for surface forms of cavitation. Torque breakdown due to cavitation is illustrated in Figure 26. In this test, the velocity and rpm were fixed to yield a TSR of 4.0. Pressure was systematically lowered and torque coefficient, C_Q and σ were recorded. The breakdown point was defined as a 3% loss in torque. Tests were conducted by beginning at a high pressure and decreasing the pressure slowly, holding at constant values while data were acquired, then resuming the decrease of pressure. Tests were conducted at tunnel velocities of 3 m/s through 6 m/s, with two repeats at the 4 m/s condition. Each maximum-to-minimum pressure constituted a single test series. The 4 m/s and 5 m/s cases were chosen as the data from which to estimate the 3% breakdown point (the 3 m/s was deemed to be a bit too low in velocity and hence, may show Reynolds number effects; the 6 m/s was limited by maximum pressure constraints in the tunnel and is thereby incomplete). The 3% torque breakdown point was found to occur at approximately σ=16.
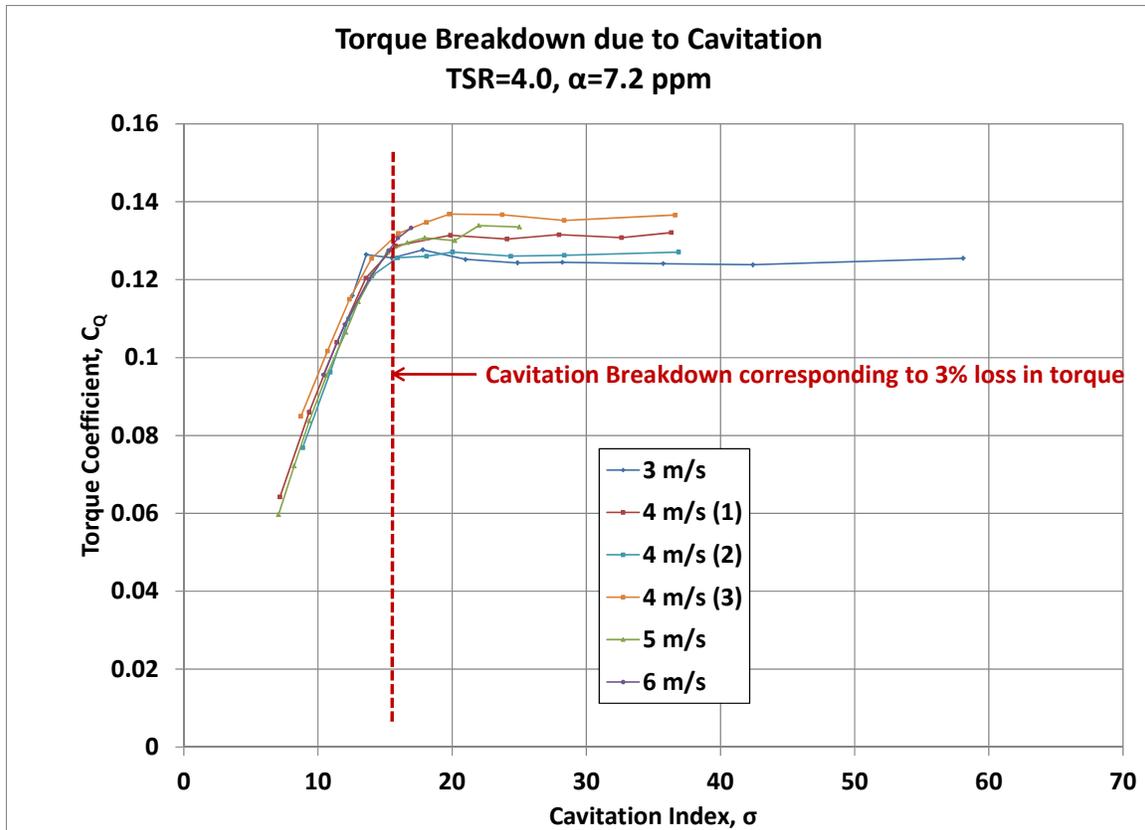
Figure 26. Cavitation breakdown data from Test 3488 at a TSR of 4.0, air content of 7.2 ppm.

Unsteady Drive Shaft Loading

Steady and unsteady drive shaft loads were measured during the tests. In addition to the unsteady thrust and torque, two-components of the unsteady bending moments applied to the drive shaft at the rotor plane attachment were measured. The first moment (Moment A) was measured in a plane aligned with a blade and the second moment (Moment B) was measured 90° from the first. Figure 27 shows the unsteady shaft loads versus measurement time over a 0.5 sec time window from the Test 3496 run 7 high frequency data set. The data in Figure 27 illustrate the blade tower interaction as this manifests itself in a blade rate unsteady load on the driveshaft. These loads manifest themselves as a decrease in the measured torque and thrust with an increase in bending moments applied to the rotor – drive shaft attachment. This behavior is similar to that encountered in wind with rotor blade tower interactions [12] and is a major contributor to drive train failure and increased maintenance costs. The blade rate character of the force signature is clearly illustrated in Figure 28 where the unsteady load data of Figure 27 is plotted versus phase angle. The phase angle of the blade-tower interaction is 0, 120, 240 degrees.

The upstream potential flow effect of the tower effectively changes the blade incidence angle as the blade passes the tower. This variation in incidence angle changes the blade loading, lift and drag, which produces a variation in the measured drive shaft thrust and torque as shown in Figure 27 and Figure 28. The thrust and torque curves show an approximate 10% reduction in loading.

47
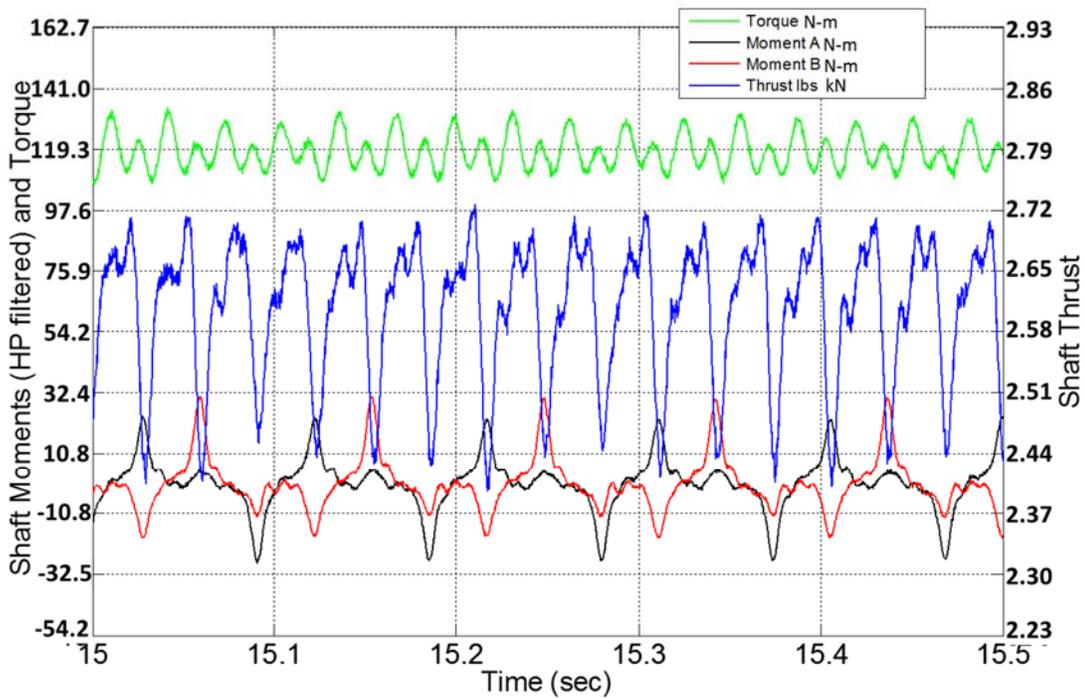
Figure 27. Measured unsteady shaft loads, U=5m/s, TSR=4.
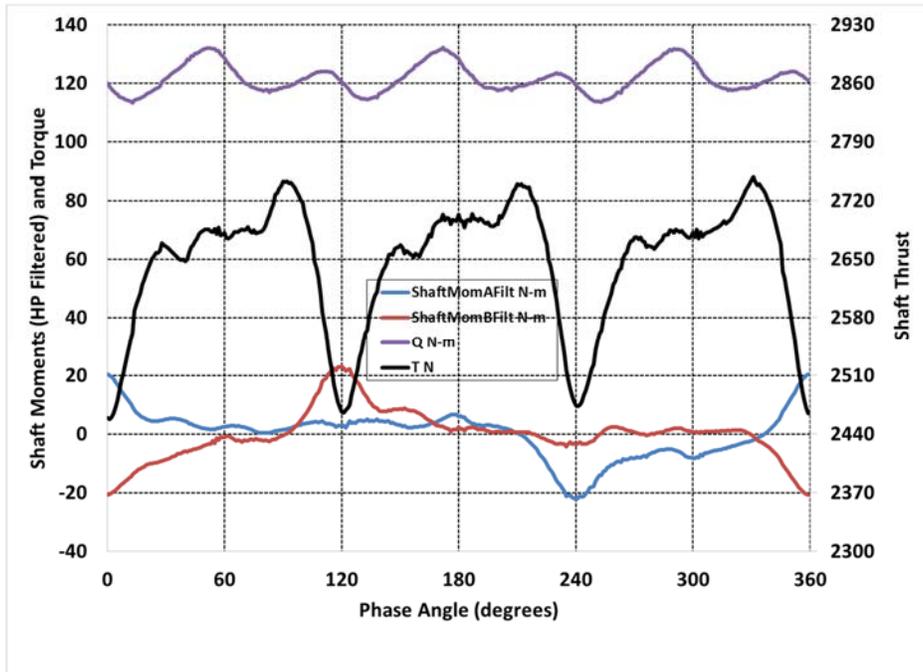
Figure 28. Unsteady shaft loads plotted versus phase angle.

The periodic change in the lift loading of one blade relative to the other two also produces an asymmetric load distribution applied to the rotor disc relative to the center of the rotor hub. This asymmetric load distribution generates the periodic bending moments applied to the drive shaft, as illustrated in Figure 27 and Figure 28. In a tower free operation, it can be shown that the

bending moments at the rotor hub to drive shaft attachment should be approximately zero with a uniform, low TI inflow and identical blade performance on each of the three blades. The bending moment data is high passed filtered at a 2 Hz cutoff frequency to remove any zero operation (V_x = 0 m/s and TSR = 0) voltage or load biases. Load cell zero voltage drift or a small bending moment applied to the shaft by the rotor weight can contribute to the zero operation bias. While the load cell zero voltage can be easily removed through a standard zeroing process, the rotor weight bias cannot be easily removed since it depends on the circumferential rotor position due to the defined coordinate direction of the load cell relative to rotor angular orientation. The high pass filtering methodology was determined to be the best solution to isolating the rotor – tower interaction effect on the drive shaft bending moments.

The full data set includes time resolved load data for all tests and runs. The unsteady ARL thrust and torque cell data were only acquired after test 3495. It is expected that the signature of the unsteady load data will not qualitatively change much in character from the on-design test runs shown in Figure 27 and Figure 28 with changing inflow speed and TSR. The amplitude of the periodic forcing will change with inflow speed and TSR as one would anticipate with relative velocity squared scaling on the blades. The blade rate frequency will vary with TSR but the general phase signature of a blade rate variation (0°, 120° and 240°) will not.

Blade Strain
The 25% and 50% span blade mounted strain gage rosettes were sampled with the high frequency A/D system throughout the test. As described earlier, the gage rosette allows for the full strain field to be measured and the principal strains to be computed. The gage factors and gage resistances for these rosettes were F=2.12 and R_G=350. The excitation voltage was 10 volts. The strain data are reported in micro-strain per the data processing procedures described earlier. Material stress is estimated using the following material properties for 17-4 stainless steel: Poisson Ratio = 0.272 and Young's Modulus of 197 GPa (28.6×10^6 psi).

Gage #2 in the 25% span location failed after the first day of testing. This the gage oriented in the spanwise direction. The other two gages, #1 and #3, continued to function for the remainder of the test until the final day of testing. While these two gages provide a measure of strain oriented at the spanwise off-axis orientations and show the blade rate unsteadiness, we are not able to assess the total bending strain along the spanwise direction or the principal strains. The mid span rosette functioned through test 3494 at which point gage #1 failed.

Figure 29 shows the measured blade strain variation at the mid span location relative to phase angle. The data illustrate that the tower – blade interaction results in a sizable (~20%) variation in unsteady blade strain. The mid-span location tended to show a greater % variation in blade strain relative to tower interaction when comparing gages 1 and 3 between the 25% and 50% locations. Figure 30 shows the calculated principal strains with the computed principal strain angle φ. The principal angle, φ, is defined earlier and is 45°-φ from the blade span axis. The data in Figure 29 and Figure 30 are for the on-design condition from Test # 3487 run 41: V_x=4.9 m/s, P=310.3 kPa (45 psia), and 664.2 rpm.
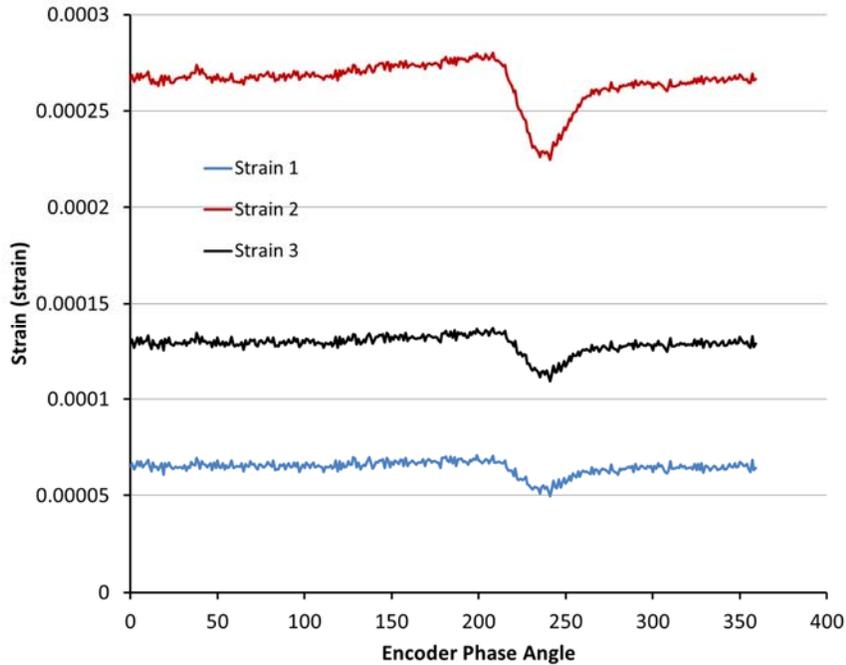
Figure 29. Measured blade strain at the mid span location relative to phase angle. TEST # 3487 RUN 41: V_X=4.9 M/S, P=310.3 KPA (45 PSIA), AND 664.2 RPM.
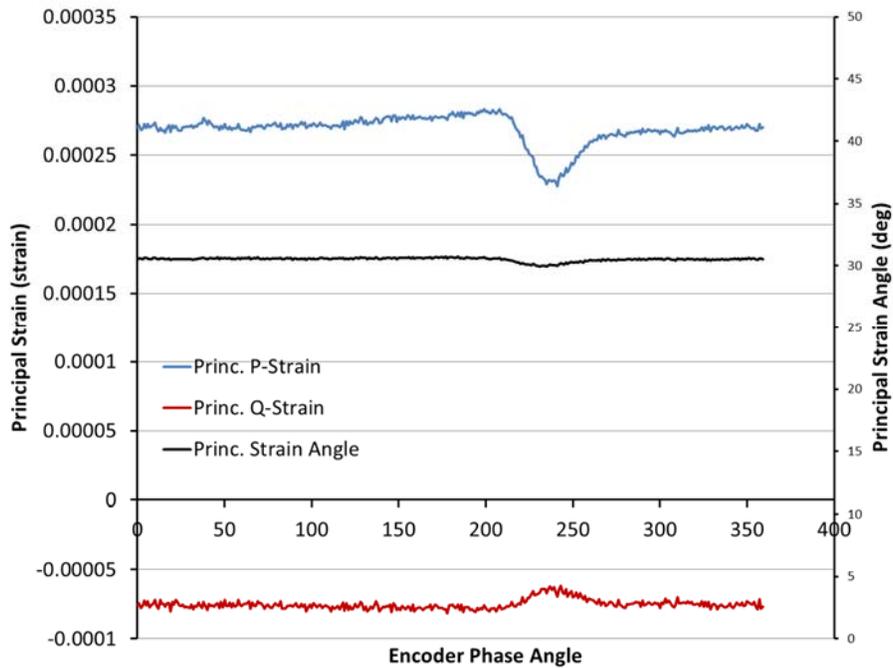
Figure 30. Principal strains at mid span. TEST # 3487 RUN 41: V_X=4.9 M/S, P=310.3 KPA (45 PSIA), AND 664.2 RPM.

The measured blade strain is directly related to the applied unsteady load on the blade. As a result, it is expected that the periodic character of the blade strain will be similar at different

50

inflow speeds and TSRs where the once per rev character is maintained but the magnitude of the strain variation will be a function of the blade loading which will vary with inflow speed and TSR.

The computed principal stresses for the 17-4 SS blade from the measured strains are shown in Figure 31. The stresses are calculated using the Young's modulus of 17-4 SS, E= 197.2 GPa and Poisson's ratio, v = 0.272.
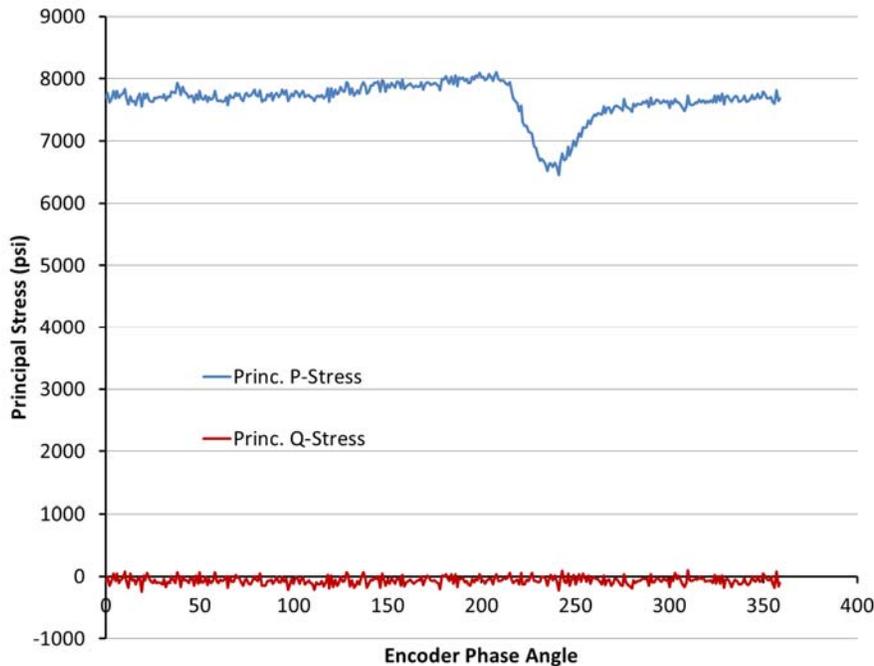
Figure 31. Computed blade stress from the measured blade strain.

Unsteady Tower Pressure

The pressure transducers along the tower show a significant cyclic behavior that coincides with the passage of the blades, blade wakes, and tip vortices in front of the tower. The tip vortex can be seen interacting with the tower in Figure 32. These are still frames extracted from the high speed video of the tip vortex / tower interaction included in the data set (File names Sandia3491r###.avi). The blade wakes and through blade flow components (swirl) vary along the blade span and this variation will translate into unsteady pressure loading on the tower. The pressure field also generated by the passing blade will contribute to the cyclic pressure loading on the tower.

51
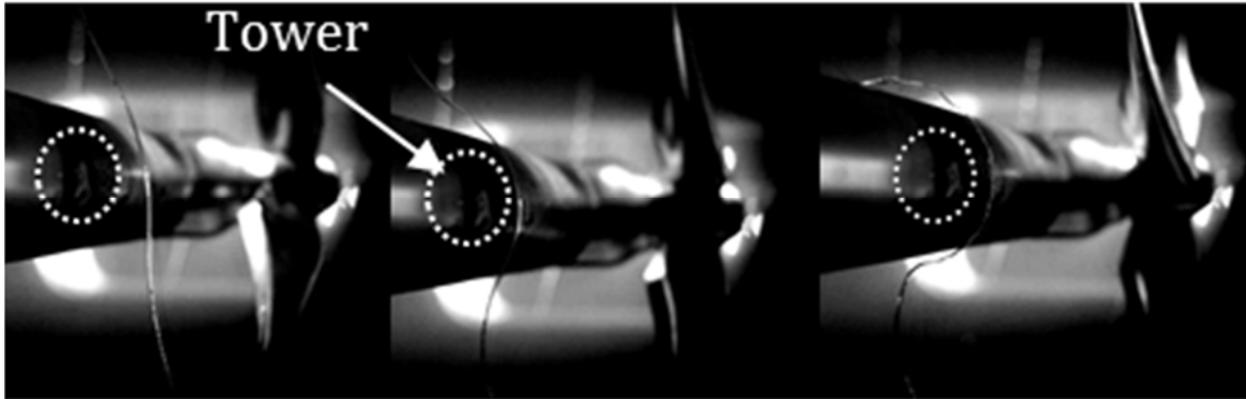
Figure 32. High speed video frames showing tip vortex – tower interaction.

Figure 33 shows the measured unsteady pressure as a function of phase angle for the 5 m/s inflow and TSR of 4 (663.6 rpm). The data in Figure 33 are plotted as pressure coefficients. Measured pressure variations are approximately ± 20 kPa along the tower. The cyclic pattern is observed to vary with freestream speed and TSR as the pitch of the blade wake and tip vortex helix varies with inflow speed and TSR. This helix pitch may also vary with spanwise distance from the hub to tip. The variation in the phase character of the tower pressures with TSR are illustrated in Figure 34. In this figure, the tower pressure data from Test 3487 and runs 37-45 are shown (~5 m/s and rpm ~500 → 1050). This unsteady pressure may generate unsteady tower vibration or noise.
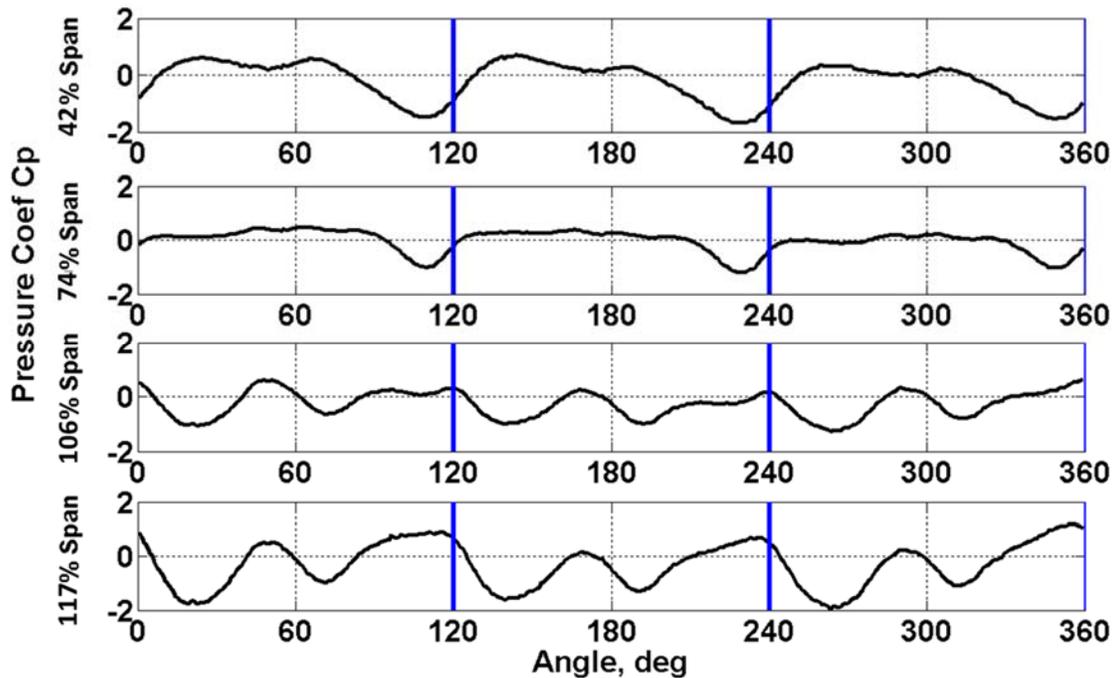
Figure 33. Tower unsteady pressures measured at four spanwise locations. Test #3496 run 7 (5 m/s, TSR = 4).
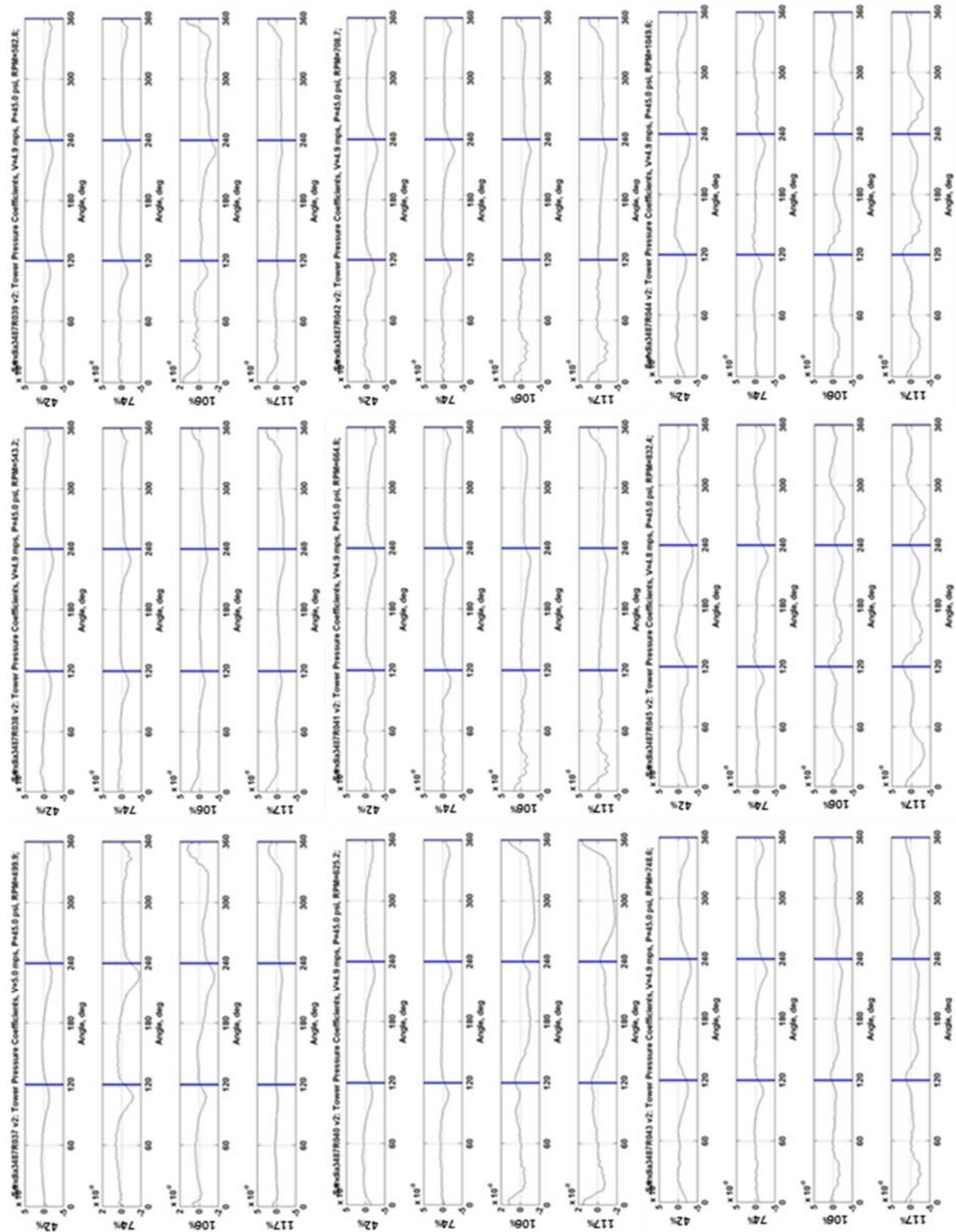
Figure 34. Variation in tower pressure signature with TSR at V_X = 5m/s.

53

Flow Field Mapping

Flow mapping was conducted with both LDV and PIV. Table 10 and Table 11 summarize the LDV and PIV measurements defining location, filename and survey notes. The green highlighted entries in Table 10 are profiles obtained in the tower wake. The LDV and PIV variable names and definitions are provided in the tables in Appendix 1.

| Table 10. LDV flow mapping summary.					
	X mm	Y mm	Z mm	Notes1	
SNL_LDV_X135_RadialExpand_Encode	134.6	Radial	0	encoded radial profile opposite tower - zoomed in to Tip region for increased spatial resolution	Probe positioned opposite tower: Vt (tangential velocity in cylindrical coordinates) = Vz
SNL_LDV_X135_Radial_Encode	134.6	Radial	0	encoded radial profile opposite tower - full region	Probe positioned opposite tower: Vt (tangential velocity in cylindrical coordinates) = Vz
SNL_LDV_X89_Radial_Encode	88.9	Radial	0	Downstream SPIV location - encoded radial profile opposite tower	Probe positioned opposite tower: Vt (tangential velocity in cylindrical coordinates) = Vz
SNL_LDV_X574_Radial_Encode_Console	574	Radial	0	encoded radial profile opposite tower - full region	Probe positioned opposite tower: Vt (tangential velocity in cylindrical coordinates) = Vz
SNL_LDV_X216_Radial_Encode	215.9	Radial	0	encoded radial profile opposite tower - full region	Probe positioned opposite tower: Vt (tangential velocity in cylindrical coordinates) = Vz
SNL_LDV_X64_Radial_Encode	63.5	Radial	0	encoded radial profile opposite tower - full region	Probe positioned opposite tower: Vt (tangential velocity in cylindrical coordinates) = Vz
SNL_LDV_X574_Radial_Encode_TowerWake	574	Y mm	-18.8, 0, +18.8	encoded radial profile tower wake - full region	Probe positioned opposite tower: Vt (tangential velocity in cylindrical coordinates) = -Vz
SNL_LDV_X250_Radial_Encode_TowerWake	249.9	Radial	0	encoded radial profile tower wake - full region	Probe positioned opposite tower: Vt (tangential velocity in cylindrical coordinates) = -Vz
SNL_LDV_Inflow_X800	-800	Radial	0	encoded radial profile Inflow Profile	Probe positioned opposite tower: Vt (tangential velocity in cylindrical coordinates) = Vz
SNL_LDV_Inflow_X17_Encode	-17	Radial	0	encoded radial profile Inflow Profile	Probe positioned opposite tower: Vt (tangential velocity in cylindrical coordinates) = Vz
SNL_LDV_BareHubInflow_X51	-50.8	Radial	0	Bare Hub profiles at inlet	Probe positioned opposite tower: Vt (tangential velocity in cylindrical coordinates) = Vz
SNL_LDV_BareHubInflow_X800	-800	Radial	0	Bare Hub profiles at inlet	Probe positioned opposite tower: Vt (tangential velocity in cylindrical coordinates) = Vz
SNL_LDV_BareHubInflow_X250_TowerWake	249.9	Radial	0	Bare Hub profiles in tower wake	Probe positioned opposite tower: Vt (tangential velocity in cylindrical coordinates) = -Vz

Table 11. PIV flow mapping summary.					
All PIV data acquired with encoding.			Data variable nomenclature see variables sheet		
For Plotting: plot contours using variables Xfilt, Yfilt, Zfilt, Radius, Angle, Vxfilt, Vyfilt, Vzfilt, Vrfilt and the corresponding std files (Vxfiltstd)					
Note for Stereo data: All SPIV taken on side of rotor opposite tower (y negative)					
Directory Name	File Name	X mm	Y mm	Z mm	Notes
SNL_Turb_1DiamDS	SNL1d#mps TSR##filt	1 rotor diam DS	0	X-Z plane, radial	# is inflow speed, ## is tip speed ratio. Variable correlation: Z & R--> Chan 1 x; X --> Chan 2 y; Vz & Vr --> u; Vx --> v. Not encoded.
SNL_Turb_DS_Y0	TDS#DegFilt	just DS of rotor	0	X-Z plane, radial	# is phase angle. Variable correlation: Z & R--> Chan 1 x; X --> Chan 2 y; Vz & Vr --> u; Vx --> v.
SNL_TURB_UP_Y0	TurbUS0Y# degfilt	Just US of rotor	0	X-Z plane, radial	# is phase angle. Variable correlation: Z & R--> Chan 1 x; X --> Chan 2 y; Vz & Vr --> u; Vx --> v.
SNL_Turb_Upwideview _Y0	TUS2DEG#f ilt	Just US of rotor	0	X-Z plane, radial	# is phase angle. Variable correlation: Z & R--> Chan 1 x; X --> Chan 2 y; Vz & Vr --> u; Vx --> v.
SNL_Turb_DS_Y-1p5	TDS1Deg#F ilt	just DS of rotor	-38.1 (-1.5")	X-Z plane	# is phase angle. Variable correlation: Z --> Chan 1 x; X --> Chan 2 y; Vz --> u; Vx --> v.
SNL_Turb_DS_Y-4	TDS2DEG#F ILT	just DS of rotor	-101.6 (4")	X-Z plane	# is phase angle. Variable correlation: Z --> Chan 1 x; X --> Chan 2 y; Vz --> u; Vx --> v.
SNL_Turb_UP_Y2	TUS3DEG#F ILT	Just US of rotor	50.8 (2")	X-Z plane	# is phase angle. Variable correlation: Z --> Chan 1 x; X --> Chan 2 y; Vz --> u; Vx --> v.
SNL_Turb_UP_Y-3	TUS3Y#Deg filt	Just US of rotor	-76.2 (3")	X-Z plane	# is phase angle. Variable correlation: Z --> Chan 1 x; X --> Chan 2 y; Vz --> u; Vx --> v.
SNL_Turb_Stereo1_Tip	st1deg#ma rfilt	63.5	Y-Z Plane, radial	Z or Alpha	# is phase angle. Variable correlation: Y & R--> Chan 1 x; Z --> Chan 2 y; Vy & Vr --> u; Vx --> -w; Vz & Vt --> v.
SNL_Turb_Stereo2_Tip_ Lowspeed	st2deg#ma rfilt	63.5	Y-Z Plane, radial	Z or Alpha	# is phase angle. Variable correlation: Y & R--> Chan 1 x; Z --> Chan 2 y; Vy & Vr --> u; Vx --> -w; Vz & Vt --> v.
SNL_Turb_Stereo3_Hub	st3deg#ma rfilt	88.9	Y-Z Plane, radial	Z or Alpha	# is phase angle. Variable correlation: Y & R--> Chan 1 x; Z --> Chan 2 y; Vy & Vr --> u; Vx --> -w; Vz & Vt --> v.
SNL_Turb_Stereo4_Tip	st4ph#filt	88.9	Y-Z Plane, radial	Z or Alpha	# is phase angle. Variable correlation: Y & R--> Chan 1 x; Z --> Chan 2 y; Vy & Vr --> u; Vx --> -w; Vz & Vt --> v.

The flow field mapping was performed with the following coordinate system definition. The coordinate system origin is located on the axis of the turbine at the hub leading edge. Positive X is in the downstream direct (flow direction). Positive Y is along the tower direction toward the right when looking upstream from downstream. The positive Z direction is vertical positive up as defined by a right-hand coordinate system. Figure 35 illustrates the coordinate system definition. The rotor rotation rate is in the clockwise direction looking upstream. The shaft encoder rotates with the drive shaft, thus, encoder angle (theta - θ) counts up from 0 to 360 in the counter-clockwise direction when looking upstream, opposite the rotor rotation direction. The stereo PIV data is taken in a Y-Z plane at defined X locations downstream of the rotor. As a result, the data measured in the Cartesian coordinate system (X, Y, Z) can be transformed into a cylindrical

coordinate system (X, Radius R, Angle α). The cylindrical angular coordinate is defined as α to distinguish from the encoder angle position θ. The encoder home pulse, θ = 0°, is aligned with blade one on the rotor and occurs with the tip of blade 1 aligned with the tower at the mid chord location, the 3 o'clock position in Figure 35.

The LDV data were post-processed with ARL's MLaDDeR processing code. Gate time weighted averaging was used to correct for velocity bias. Time coincidence filtering with a 200 percent gate time filter was performed to ensure sampling time coincidence between the two LDV velocity channels. The time coincidence filtering was needed to compute the Reynolds stress statistics[51]. Noise filtering was performed with either a 3 rms histogram or 3 rms elliptic filter[52].
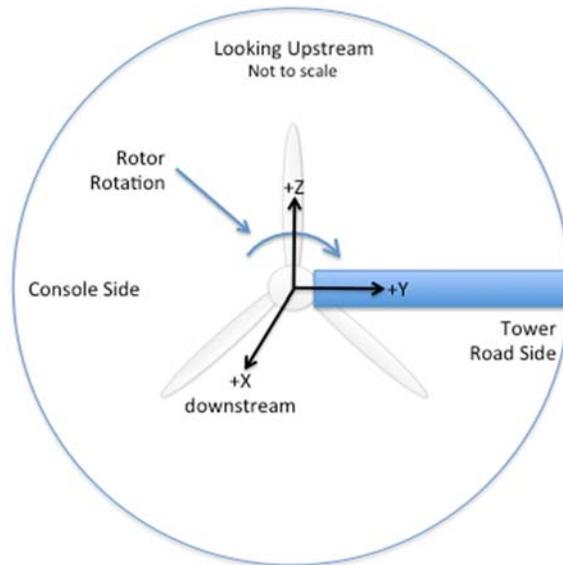
Figure 35. Coordinate System Definition.

Bare Hub Measurements:

Bare hub velocity surveys were taken with LDV. The bare hub surveys were conducted at three axial locations as shown by the green-shaded boxes in Figure 7. Those surveys were obtained at the design tunnel velocity of 5 m/s. The driveshaft was spun at a speed of 664 rpm to include any secondary effects of the rotating components (not including the rotor). The three surveys included two surveys upstream of the model and one survey in the model tower wake. The bare hub surveys were not phase encoded. The computed mean velocities for the two upstream surveys are shown in Figure 36. Axial (X) and vertical (Z,) components were measured with the two-component LDV. The surveys were conducted from the console-side window, traversing into the tunnel past the tunnel centerline. Positive Y is on the tower side of the rotor and the flow stagnation or flow blockage effect of the tower can be seen in the profile at X=-50.8 mm. The tower causes an approximate 0.5 m/s reduction in the axial velocity. The open symbols represent the X=-800 mm upstream survey, and the closed symbols the X=-50.8 mm upstream survey. Results show that the inflow velocity far upstream (X=-800 mm) is generally uniform with only a small velocity deficit due to the blockage caused by the tower on the roadside of the tunnel.
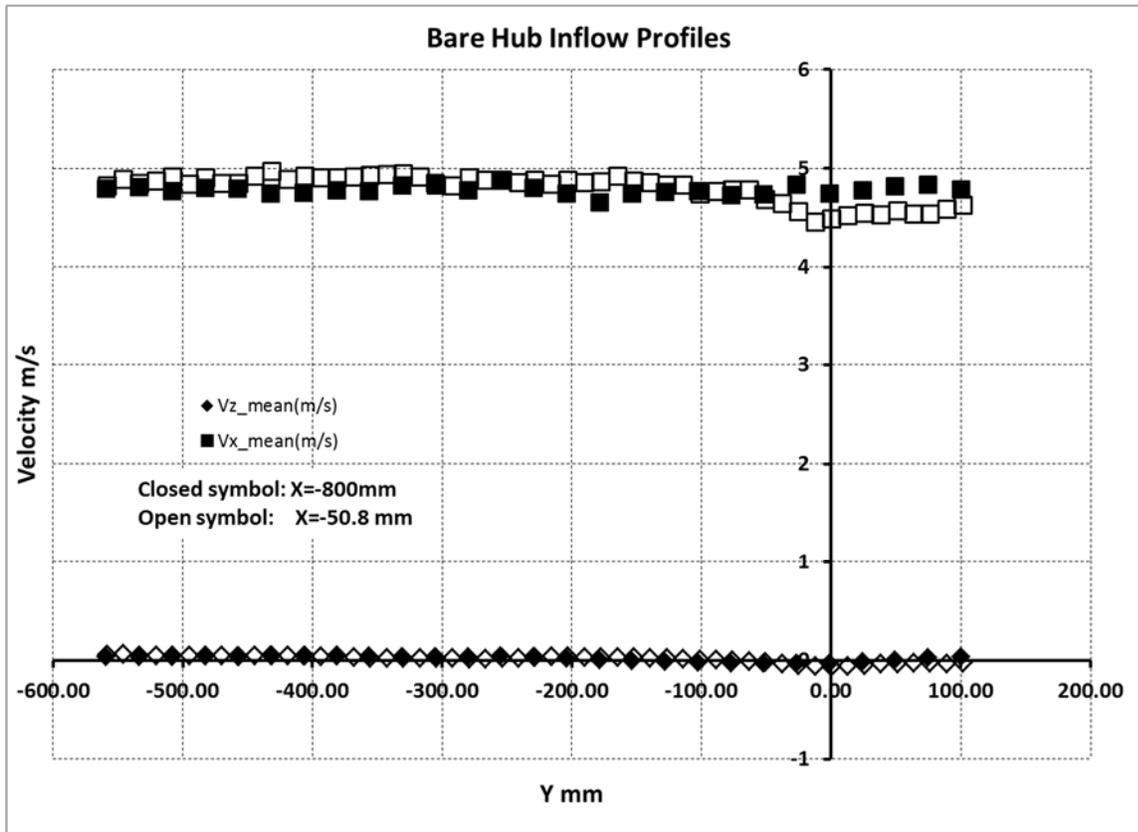
Figure 36. Bare hub inflow profiles.

The tower wake profile measurements are plotted in Figure 37. The profile was measured at an axial location X=249.9 mm or 79.4 mm downstream of the trailing edge of the 76.2 mm diameter tower. The same LDV system setup was used but the system was setup and traversed on the road side of the tunnel from the drive shaft out to the tunnel wall. The fiber optic probe was rotated 180 degrees to realign the probe measured axial velocity in the positive X direction in the tunnel. This probe rotation inverted the measured positive vertical velocity component to the –Z direction. As a result, the Vz component velocity data for all the road side (tower wake) measurements were multiplied by -1 to transform the Vz component data into the test coordinate system with Z positive up.

A large junction vortex will form upstream of the tower at the tower – tunnel wall junction. This vortex wraps around the tower and creates a counter-rotating vortex pair aligned with the flow direction. This counter-rotating vortex pair creates a well-defined velocity signature in the tower wake near the wall. The vortex legs create a wall-directed downwash behind the tower along the tops of the vortices away from the wall. Near the wall, both a wall-directed stagnation effect and a crossflow (Z-direction) pumping effect slows the axial velocity. The near wall velocity characteristics are most likely related to this complex flow field associated with the junction vortex. The measured Reynolds stresses in the tower wake are shown in Figure 38.
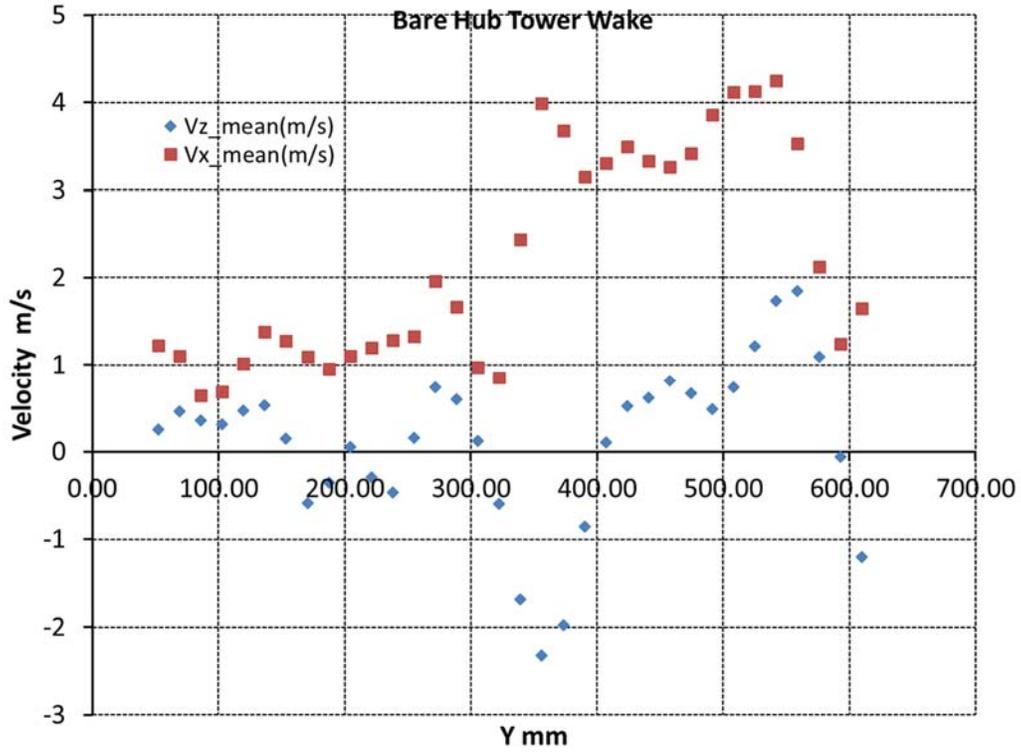
Figure 37. Mean velocity profiles in the tower wake.
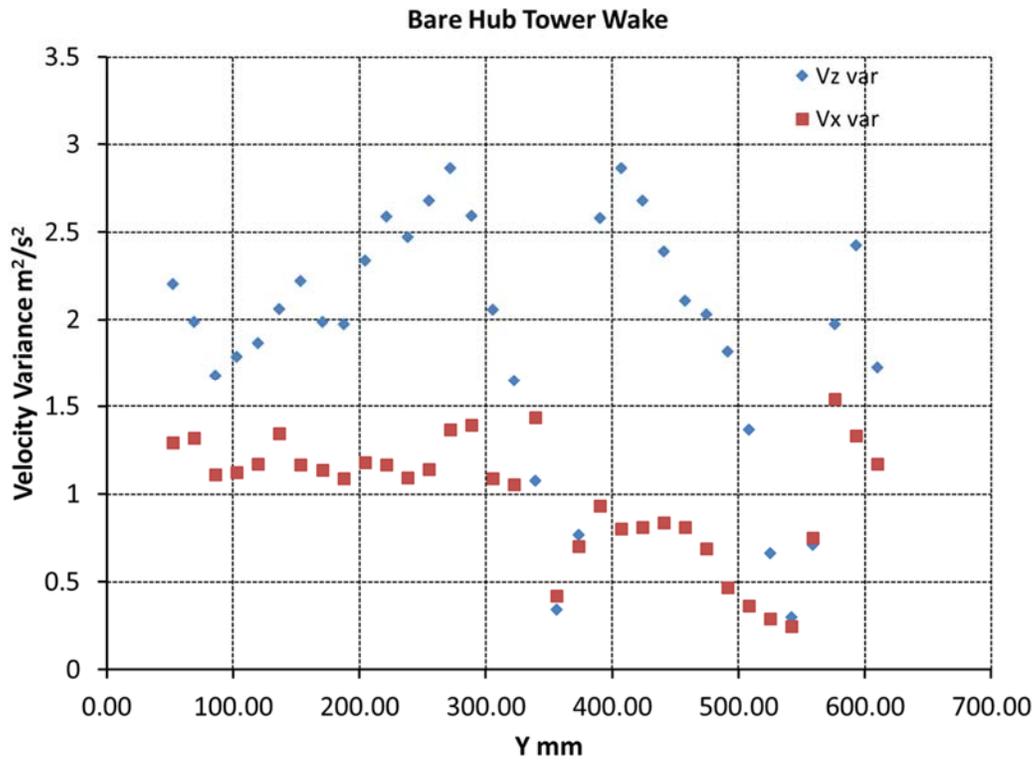
Figure 38. Reynolds normal stress profiles in the tower wake.

Rotor Measurements:

The LDV profile measurements with the turbine were all conducted at a tunnel velocity of 5 m/s and 664 rpm (TSR=4). All flow field measurements with the rotor, LDV and PIV, were encoded with rotor angular position θ. Figure 39 shows the time-averaged mean inflow velocities with the operating rotor at the -800 mm and -17mm axial locations. The impact of the rotating rotor can be seen in the profiles at X=-17mm. Figure 40 shows contour plots of the phase averaged inflow velocity data as a function of rotor angular position. The blade and tower influence are visible in the contour maps at X=-17 mm.
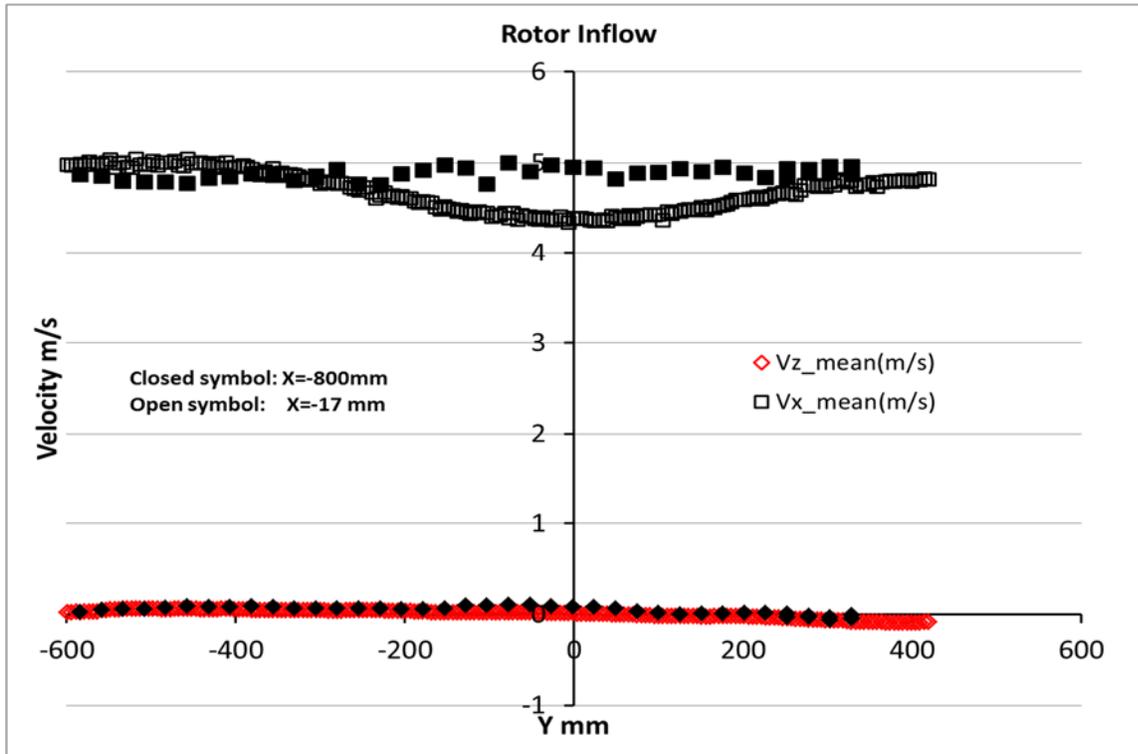
Figure 39. Rotor inflow profiles.
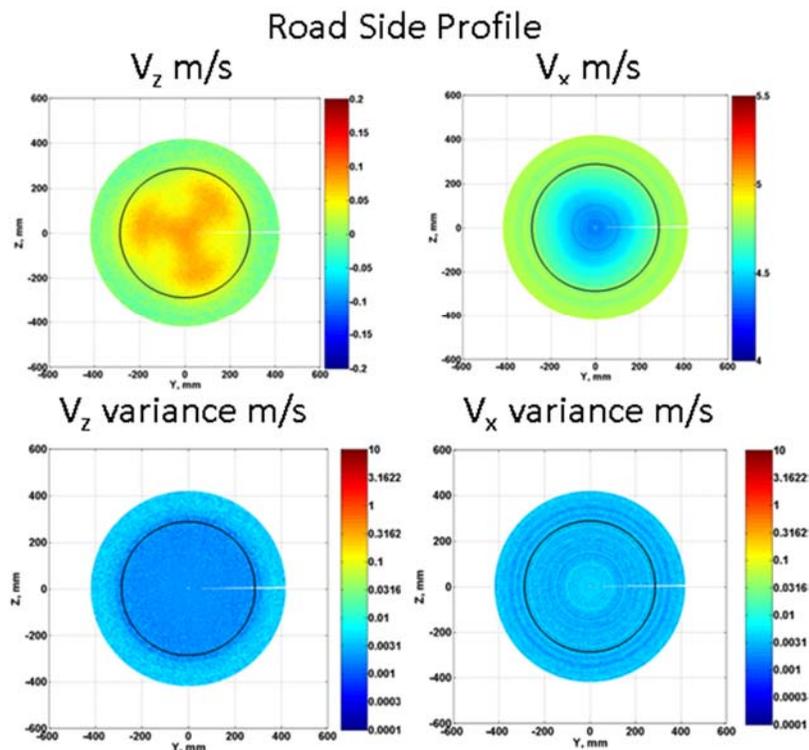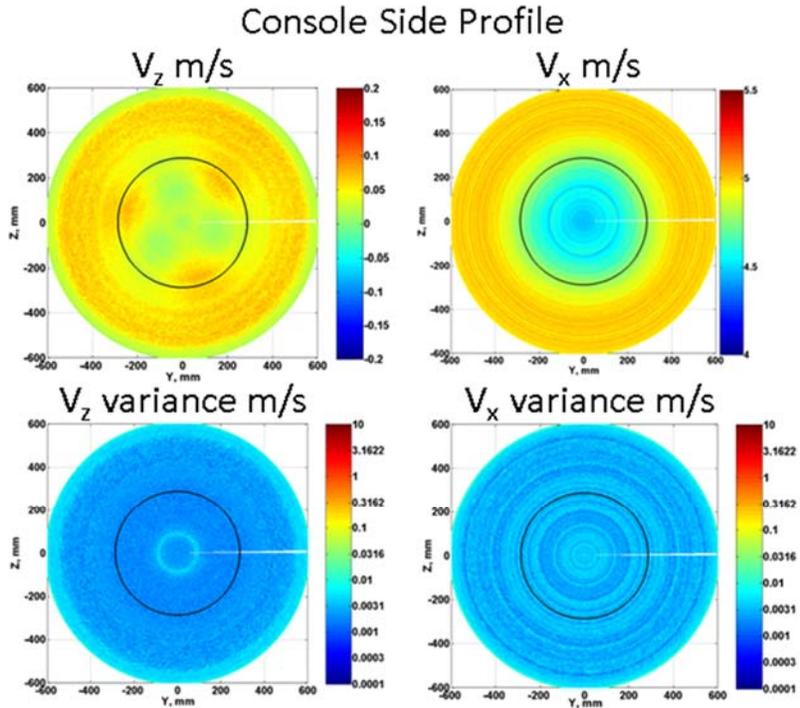
Figure 40. Contour map of inflow velocity at X=-17mm using LDV traversed opposite of tower and in line with tower.

Spatially and temporally resolved LDV measurements were conducted in the wake of the turbine as defined in Figure 7 and Table 10. All downstream rotor measurements (LDV and PIV) were encoded with the rotor position. The LDV measurements downstream of the rotor were performed with the two system setups similar to those described earlier. The notes section of Table 10 describes the probe position relative to the model and tower. The non-tower wake profiles were conducted with the fiber optic probe setup on and traversed from the console side of the tunnel, opposite to the tower. The probe was aligned and traversed along the rotor radius direction, on the negative Y-directed axis at Z=0 from the rotor drive shaft out to beyond the rotor plane toward the tunnel wall. These encoded profiles do not have the tower wake influence in the measurements and quantify the flow field associated with each blade wake and flow passage between the blades free from tower effects. These measurements effectively quantify the spatial wake flow field associated with rotor only configuration such as would be predicted in most design code methodologies where the tower is usually neglected. The tower wake profiles were conducted with the fiber optic probe set up on the road side (in line with the tower) of the tunnel axially behind the tower on the Z=0 axis. The "SNL_LDV_X250_Radial_Encode_TowerWake" profile was conducted along the rotor radius with a positive Y-directed traverse at Z=0 from the rotor drive shaft the tunnel wall. The downstream rotor wake profile "SNL_LDV_X574_Radial_Encode_TowerWake" was conducted at three Z locations -19.05 mm, 0 mm and 19.05 mm mapping out a Y-Z plane at X=574 mm.

Figure 41 shows the encoded mean wake flow development measured behind the rotor by the two-component LDV. The data, shown in the contours maps in Figure 41, were measured at X = 63.5, 89, 135, 216 and 574 mm. The color maps were generated with the same colormap scale for easy and direct assessment of the mean flow wake development up to one rotor diameter downstream. The contour data shown in Figure 41 were measured on radial profiles from the console side of the tunnel opposite the tower and, thus, do not exhibit tower wake effects. This data were phase averaged with a two degree phase window and time-coincidence filtered to allow for Reynolds shear stress calculation. The two degree encoder bin width provides a higher number of ensembles per phase window for calculation of the statistics.

The contour maps, in Figure 41, illustrate the complex flow patterns in the near-wake structure of the rotor. The thin rotor blade wakes are visible in the V_T contours as the thin radially oriented regions of positive V_T at the ~100, 220 and 340 degree encoder angle positions at the X = 63.5 mm axial location. The strong negative V_T, blue, regions in the contours represent the significant flow turning by the rotor blades. The tip vortices shed from the blade tips are indicated by the small regions of large amplitude, alternating positive and negative V_X velocity component observed along the black circle representing the rotor tip in Figure 41. The wake deficit and swirl component of the wake are still strong at one diameter downstream of the rotor with clear evidence of strong tip vortices. The instantaneous PIV data at one diameter downstream can provide a measure of the tip vortex strength at this location.

Figure 42 shows the measured Reynolds stresses for this data set. Color maps are maintained at a constant range unless otherwise indicated. High Reynolds stress levels are observed to occur on the shear layers associated with the blade wakes and the blade passage jets. The vortices are confined regions of high stress. However, these high stress values are, in part, associated with slight spatial meandering of the vortices from revolution to revolution.

The time averaged LDV velocity data corresponding to the contours shown in Figure 41 and Figure 42 are shown in Figure 43 and Figure 44. The mean velocity data, shown in Figure 43, shows a flat outer flow around the rotor wake with a defined wake deficit. The wake deficit increases with increasing axial distance downstream of the rotor with a well-defined swirl component that increased with radial distance in toward the hub. The Reynolds stress data shown in Figure 44 a) and b) show elevated turbulence levels in the near wake that quickly decay by 135 mm downstream. The tip region of the flow exhibits very large stresses due to the cyclic presence of the tip vortices in the measurement field.
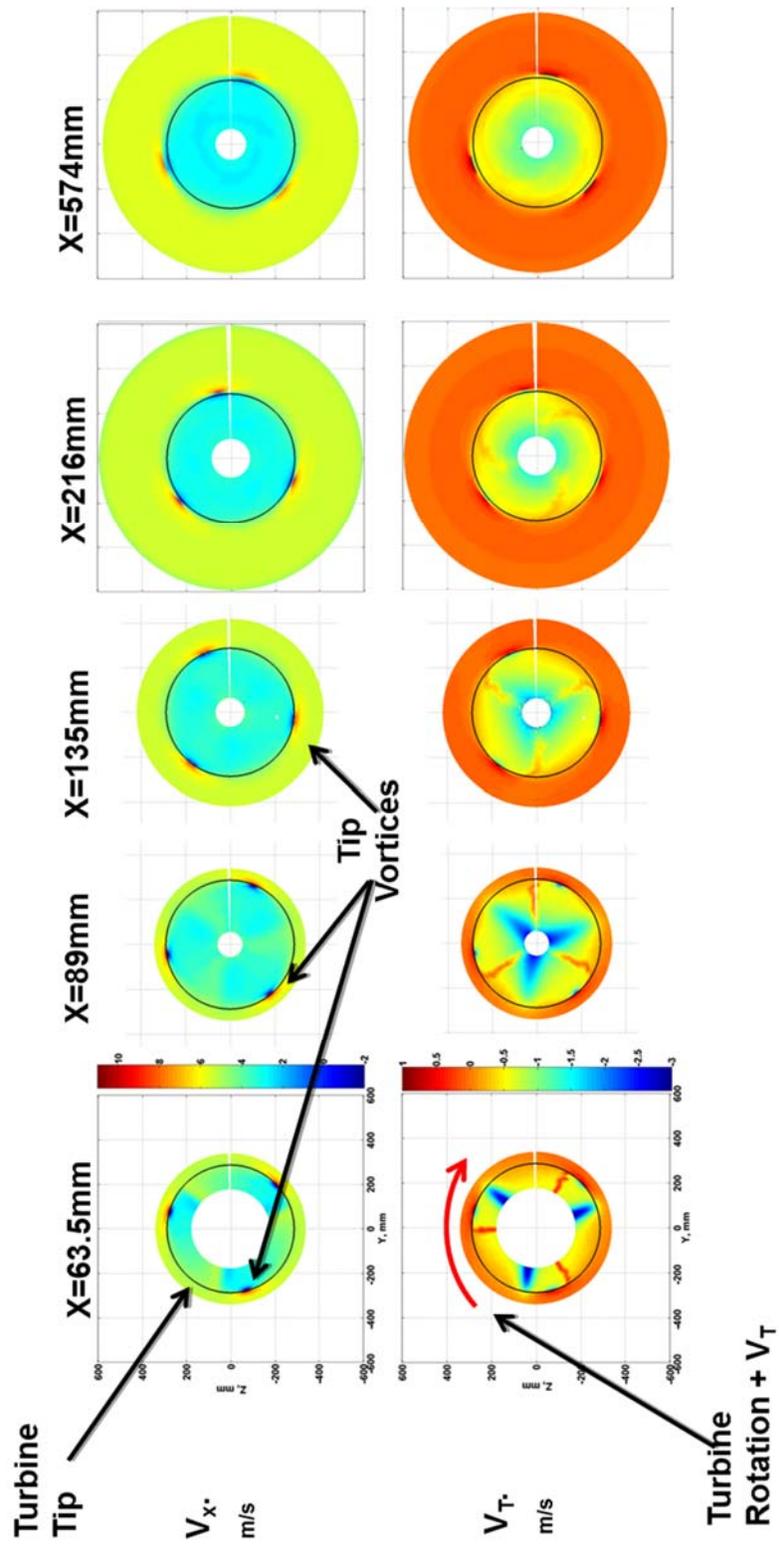
Figure 41. Mean wake flow field development downstream of rotor.
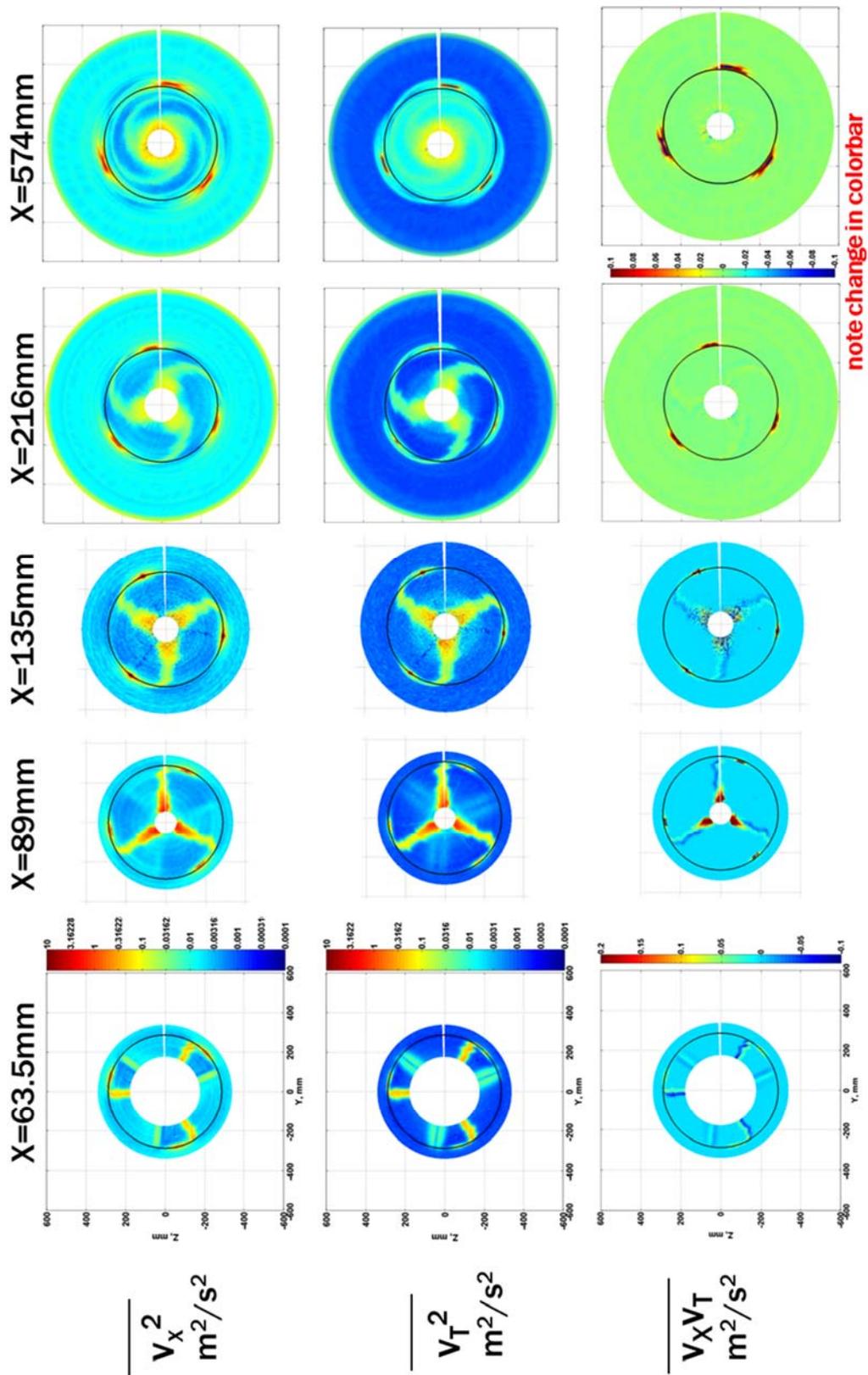
Figure 42. Reynolds stress development in the wake flow of the rotor.
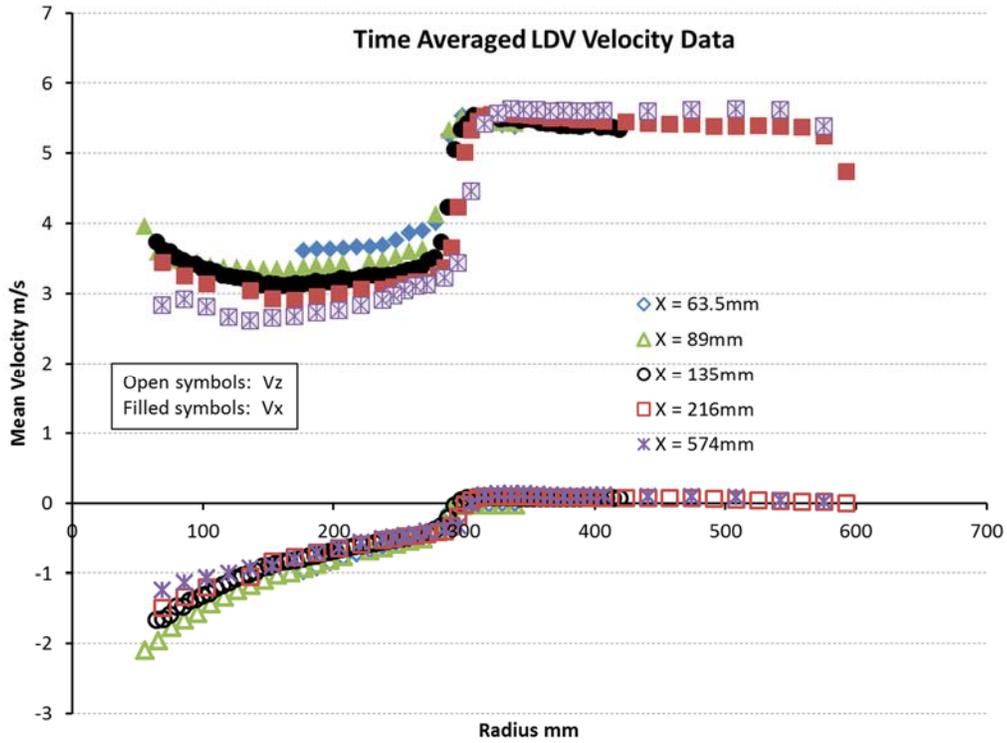
Figure 43. Time averaged mean velocity profiles of the data in Figure 41.
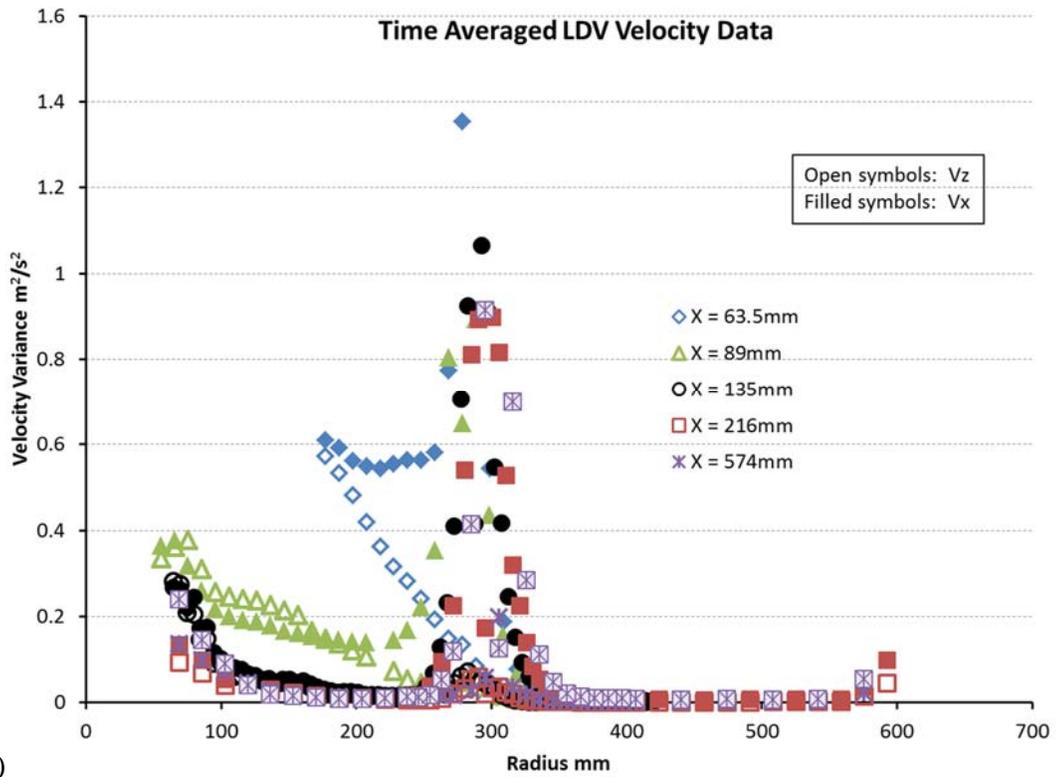
a)
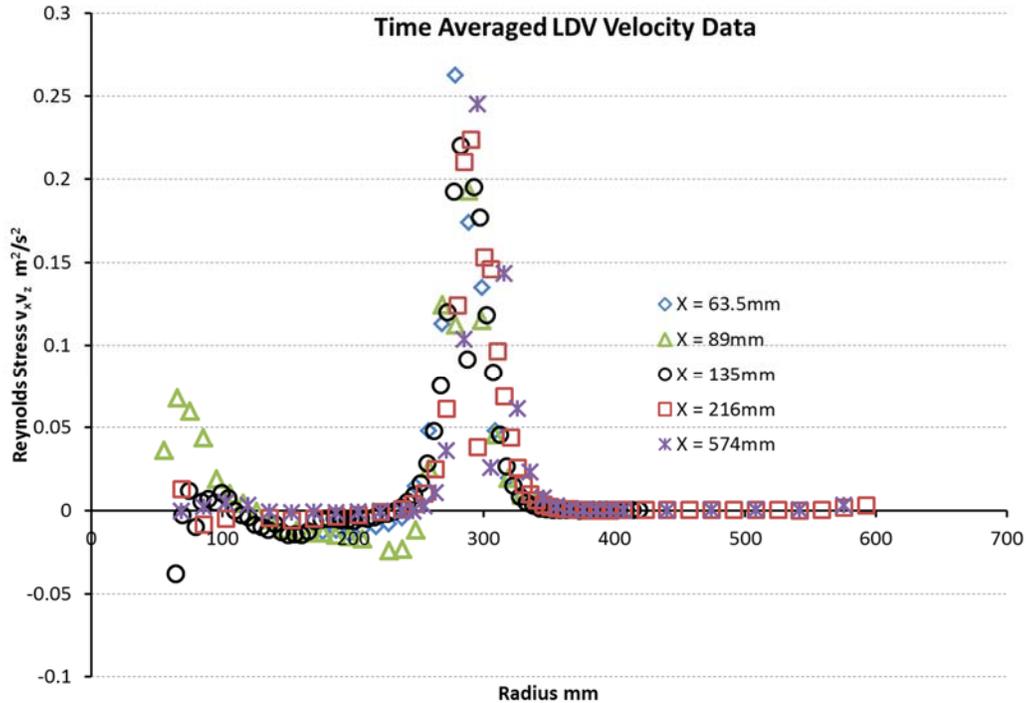
b)

Figure 44. Time averaged Reynolds Stress profiles of the data in Figure 42. a) Normal stresses, b) shear stresses.

The time averaged tower wake flow data, mean flow and turbulence, at X = 249.9 mm are shown in Figure 45. The peculiar behavior is believed to be associated with a combination of the near wall junction flow structure and window assembly. The inner flow structure is a combination of the tower wake flow interacting with the rotor flow dynamics, blade wakes and flow turning. Phase averaged contour plots of the data in Figure 45, shown in Figure 46, illustrate the complex flow fields associated with blade interaction with the tower and the combined flow acceleration and swirl outboard of the rotor tips.

The complex wake flow structure at X = 249.9 mm recovers to a more uniform flow structure by X = 574 mm downstream of the rotor. Figure 47 shows the wake mean flow and turbulence at the X = 574 mm location. Turbulence structure is concentrated in the wake / outer flow shear layer just outside of the rotor tip. The profile data at X = 574 mm were measured at three Z locations of -19.05, 0 and +19.05 mm to determine spanwise variability and development. While the mean flow profile data do not show much spanwise variability, the turbulence data in Figure 47 b) show a slight spanwise sensitivity in the outer wake flow with higher variances measure at Z = 0 mm.
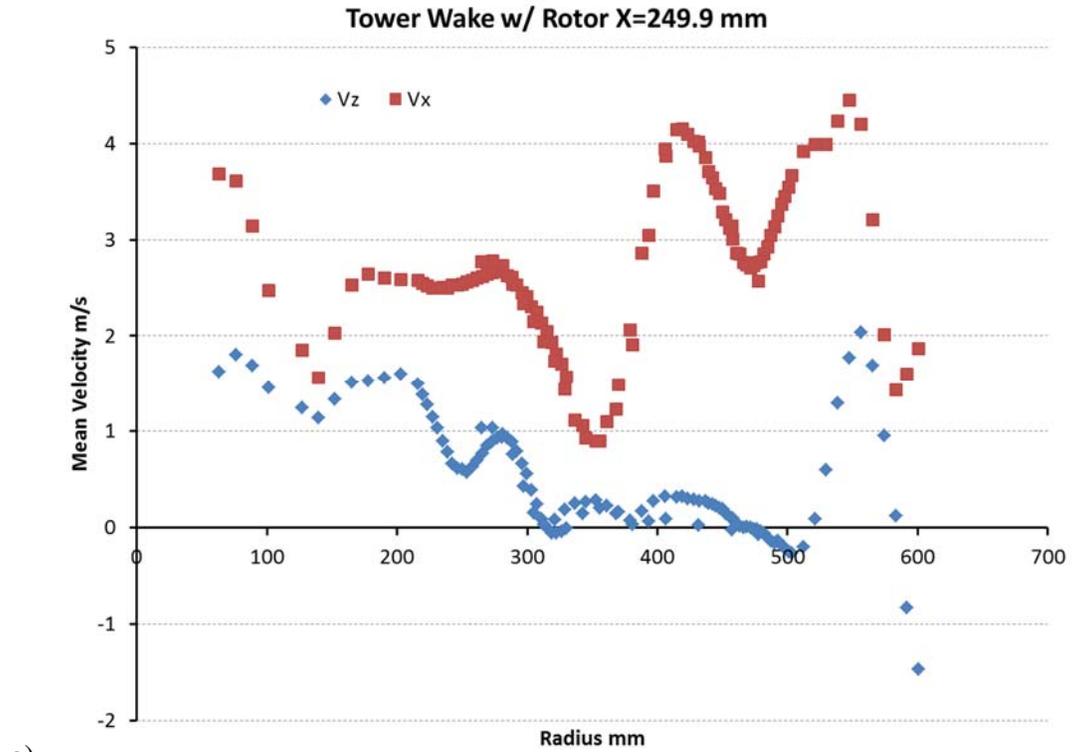
a)
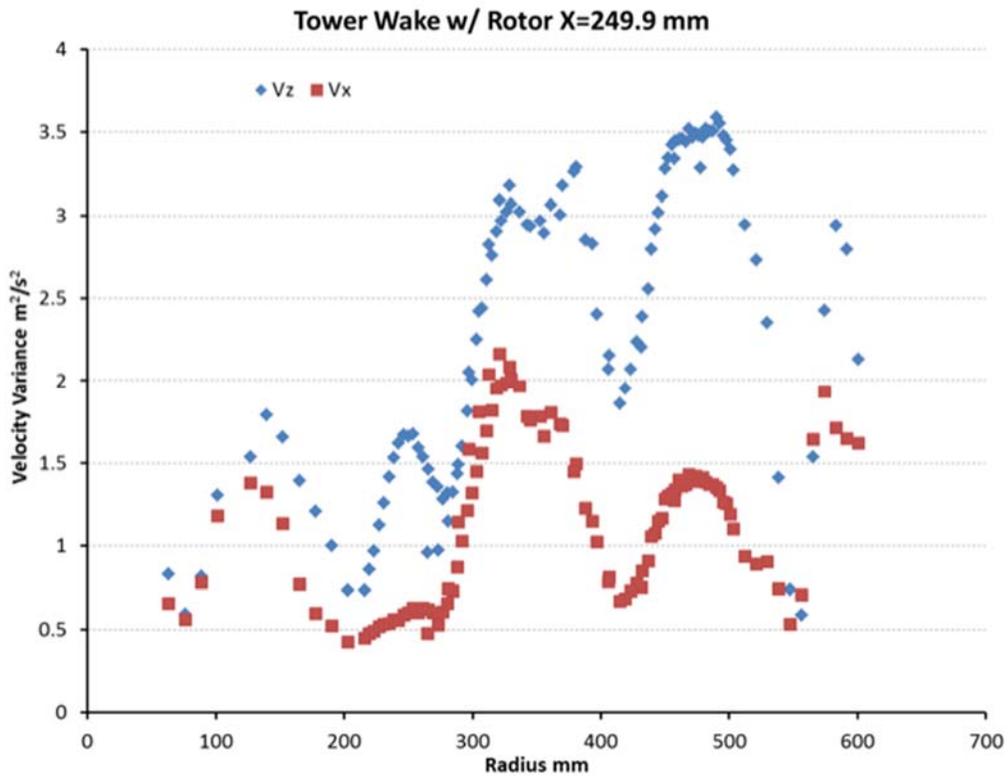
b)

Figure 45. Tower wake flow at X = 249.9 mm. a) mean flow, b) turbulent normal stresses.
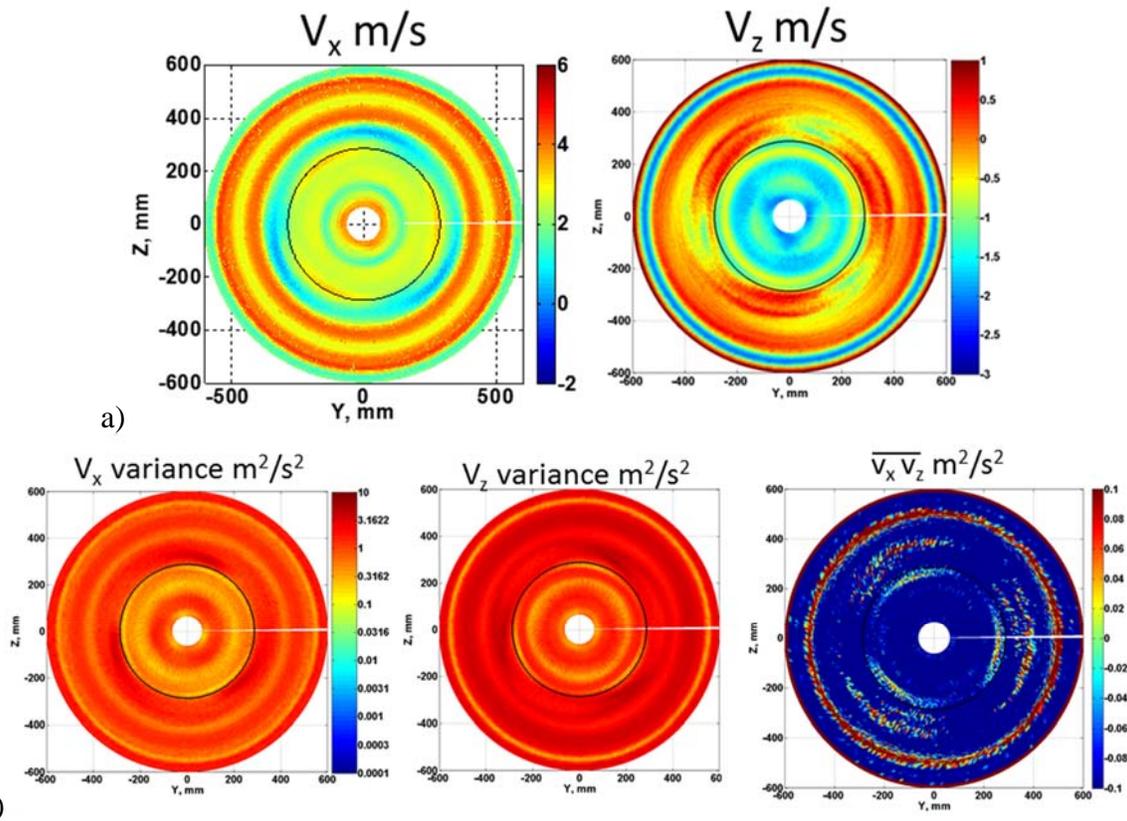
Figure 46. Phase averaged tower wake flow data at X = 249.9 mm. a) mean flow structure and b) turbulence.
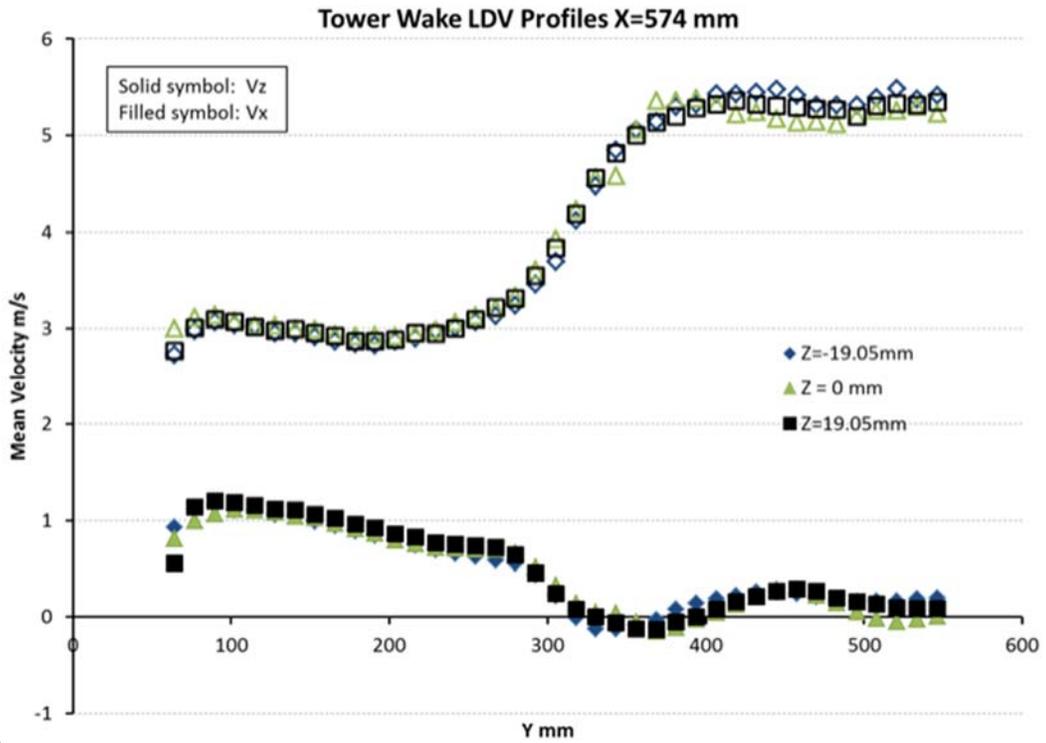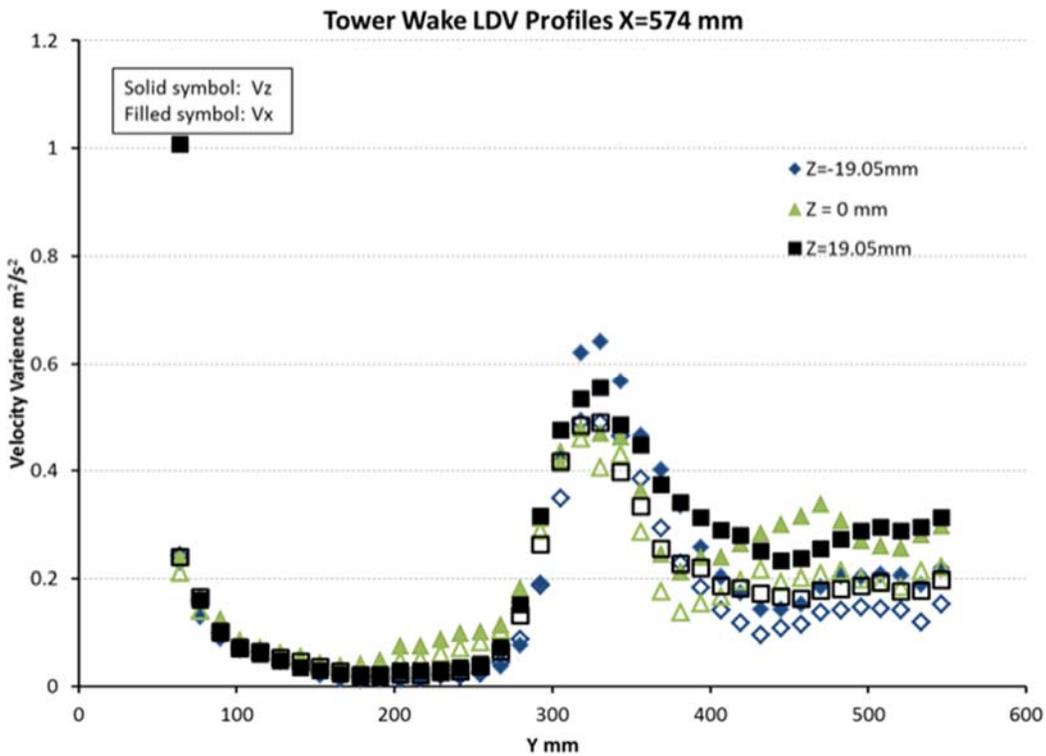
Figure 47. Tower wake flow field downstream of the rotor at X = 574 mm. a) mean flow and b) turbulence.

Planar PIV measurements were performed at the rotor inflow immediately upstream of the rotor, Figure 48 and Figure 49, in the rotor wake immediately downstream of the rotor, Figure 50.

Inflow mappings were obtained with a non-tilted camera orientation imaging the rotor hub and a small region of flow below the hub leading edge (LE) with a larger region of flow above the hub LE. Tilted camera flow mappings were obtained to capture a larger field view excluding the hub region and including flow beyond the rotor tip radius. The planar flow mappings were recorded on the rotor centerplane in a X-Z plane at Y = 0 mm, as well as several off-center mappings at Y ≠ 0. The full PIV flow-mapping matrix is outlined in Table 11. The PIV data were acquired phase locked to an encoder position. Typically 10 to 15 phase angles were obtained over the 120 degree phase window associated with one blade passage.

Figure 48 and Figure 49 show the planar PIV inflow maps for the small and large field of views. The small field of view data set, Figure 48, was obtained just upstream of the rotor plane. The large field of view mapping, Figure 49, was acquired with the rotor plane bisecting the field of view providing an inflow, through the rotor plane and just downstream of the rotor plane velocity characterization. The contour maps show the velocity field at the four phase angles of 80, 100, 140 and 150 degrees. The 140 degree encoder position corresponds to the laser light bisecting one rotor blade while the 80 degree position is aligned between two rotor blades. The small field of view contour maps in Figure 48 show the stagnation flow at the hub LE with flow turning around the hub. The large field of view contours, Figure 49, exhibit flow acceleration and turning in the rotor tip region with the formation of the tip vortex in the 140 degree contours. The planar vorticity, calculated from the V_r and V_x components of the measured velocity, is also shown in Figure 49. This measure of vorticity is reasonable for the large angle, ~ 80-85°, of the wake helix relative to the axial flow direction downstream of the rotor. The flow mapping at 150 degree encoder phase shows the tip vortex convecting downstream and strengthening with a strong axial flow wake developing.

The downstream planar PIV flow mapping on the centerline of the rotor, Y = 0 mm, is shown in Figure 50. Similar to the large field view inflow mapping shown in Figure 49, this downstream mapping was performed with a tilted camera to increase field view and capture the flow field outside of the rotor radius. The 80, 100, 140 and 150 degree encoder positions are also shown in this figure. The tip vortices are clearly visible in the data sets. The axial flow acceleration around the rotor is evident at the 80 and 100 degree phase angles while the blade wakes are starting to convect into the field of view at the 140 and 150 degree phase angles. These PIV maps can be used to quantify tip vortex development, size and strength, with convection downstream as well as the helix spacing on the rotor wake.

Planar PIV flow mappings conducted one rotor diameter downstream are shown in Figure 51. The mean flow, rms velocities and the $v_r v_x$ Reynolds shear stress are shown in the figure. The camera field of view was selected to image the outer half of the rotor wake and the adjacent outer flow for evaluation of blockage effects and comparison to velocity ratios predicted with the blockage correction scheme used in this study [21]. The full data set for this flow mapping includes inflow velocities of 2, 3, 4 and 5 m/s at TSRs from 3 to 6. The 3, 4, and 5 m/s inflow speed data sets at a TSR of 4 are shown in Figure 51.

Stereo PIV flow mapping was performed immediately downstream of the rotor at the X=63.5 mm and X = 89 mm axial positions. The X = 63.5 mm mappings, "Stereo1Tip" and "Stereo2TipLowSpeed" were confined to approximately the outer 30% span of the rotor plane

and a small region outside of the rotor radius. This reduced field of view was due to restricted optical access of the upstream camera to the imaging plane at the inboard regions due to blockage by the rotor blades. This flow mapping then focused on the tip flow region of the rotor. Stereo flow maps were obtained at two inflow speeds, the design speed of 5 m/s and a non-cavitating tip vortex condition at 4 m/s. The downstream stereo flow maps at X = 89 mm, "Stereo3Hub" and Stereo4Tip" were conducted at 5 m/s and comprised two independent, overlapping fields of view to provide a full flow field mapping from the hub out beyond the rotor radius. The stereo PIV data were acquired over an encoder window of ~160 to 280 degrees.

Figure 52 and Figure 53 show a representative mapping of the X = 89 mm stereo PIV velocity and Reynolds stress at an encoder phase angle of 255 °. The encoded LDV data, from Figure 41 and Figure 42, at the same location are shown for comparison with the stereo PIV data. The same color contour levels are used for both the PIV and LDV contour maps. The LDV contours maps are rotated 60° clockwise to align with the PIV maps for ease of comparison. The PIV data show excellent agreement with the LDV in both the mean velocity and Reynolds stresses. Small discrepancies are most likely due to the large fields of view used in the PIV mappings and the limited number of ensembles used to compute the higher order statistics. The large spatial resolution, relative to the LDV, was documented earlier in the report and can produce a spatial low pass filtering. Noise can also pass the PIV processing noise filters along the edges of the velocity maps due to edge effects related to particle loss in the image pairs along the edges of the vector processing region.

Figure 54 shows the 4 m/s stereo PIV flow mapping of the rotor tip flow at X = 63.5 mm. The data in Figure 54 are plotted at an encoder phase angle of 205° intersecting the tip vortex. The 4 m/s data set is shown to characterize the full 3-d flow field associated with the strongly inclined tip vortex under non-cavitating flow conditions. The intermittent tip vortex cavitation observed in the 5 m/s data set at this same location causes vector drop out in the vortex core due to the intense laser scattering from the local cavitation bubbles in the core. When the tip vortex is at the focal plane of the imaging system, this scattering and resulting vector drop out compromises estimation of the velocity statistics in the vortex core.
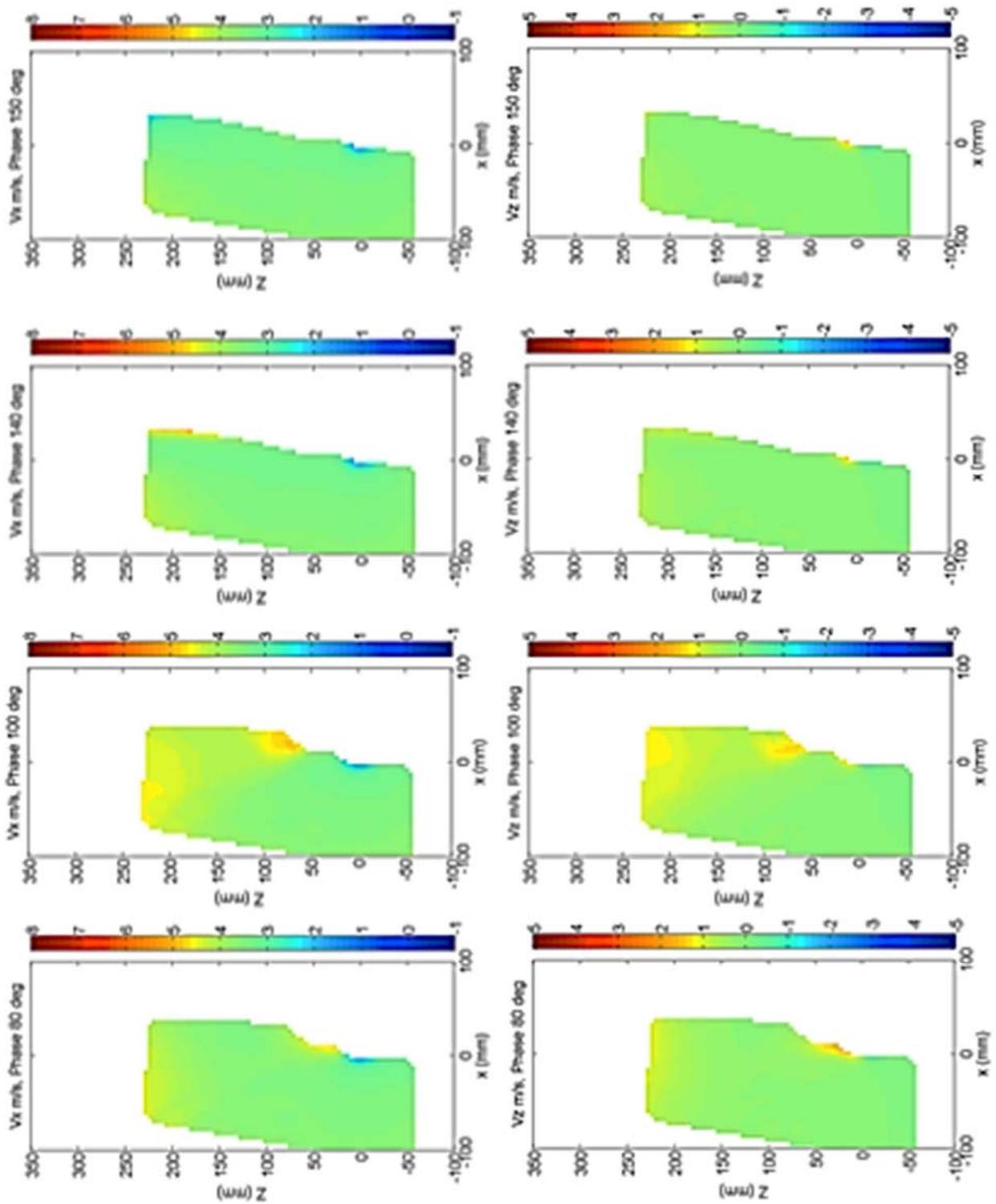
Figure 48. Small field of view planar PIV velocity map at the rotor inflow.

72
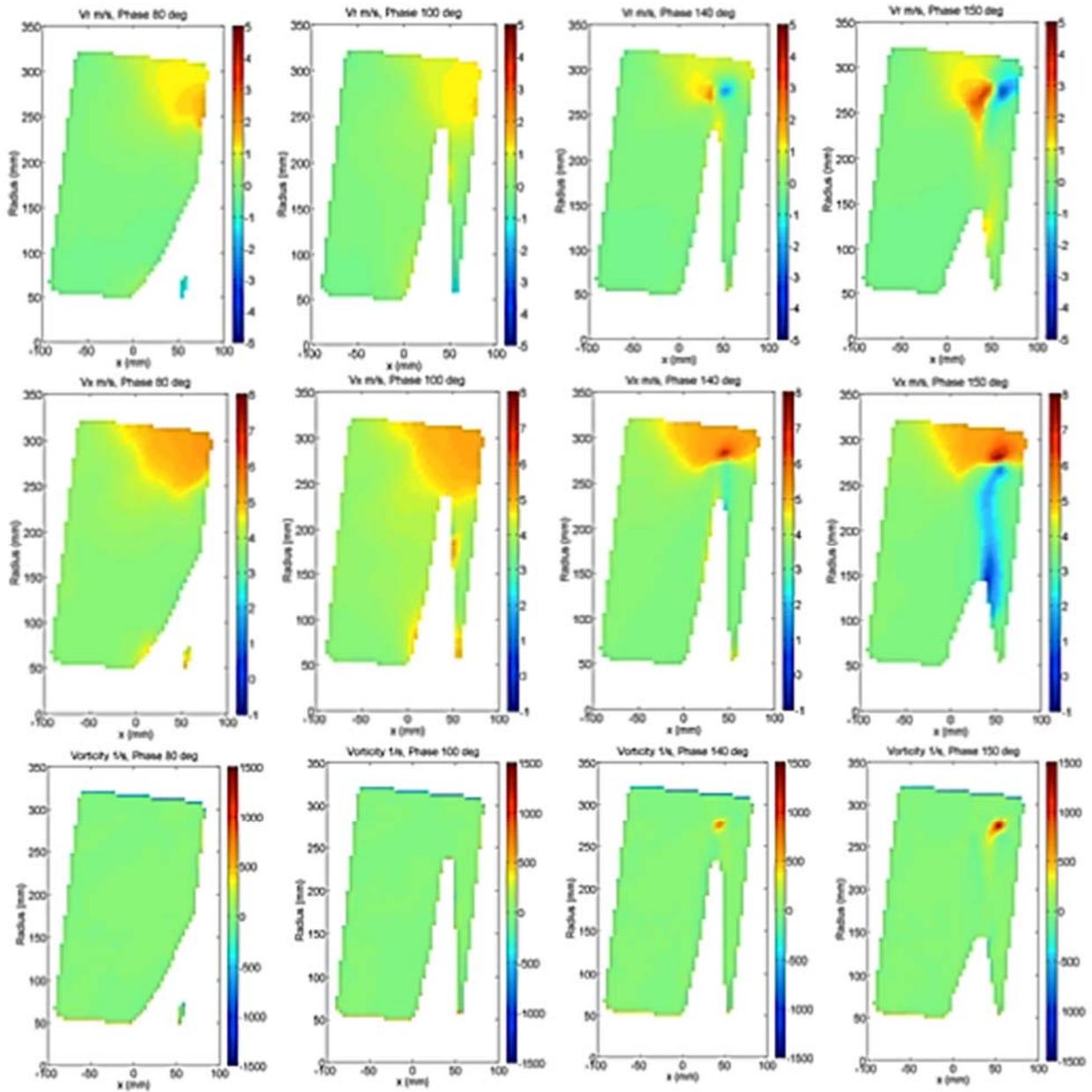
Figure 49. Large field of view planar PIV velocity map at the rotor inflow.
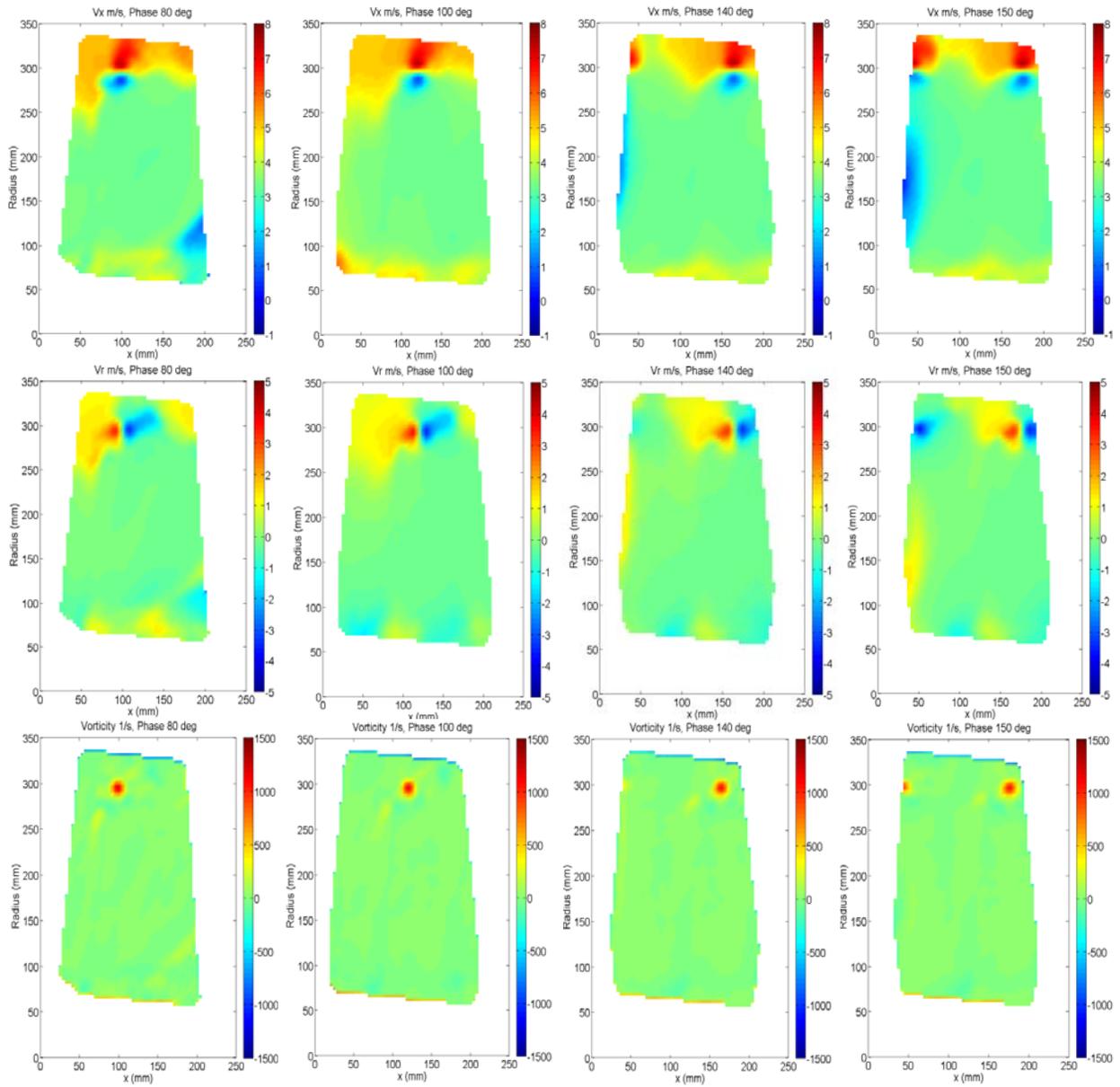
Figure 50. Large field of view planar PIV velocity map immediately downstream of the rotor.
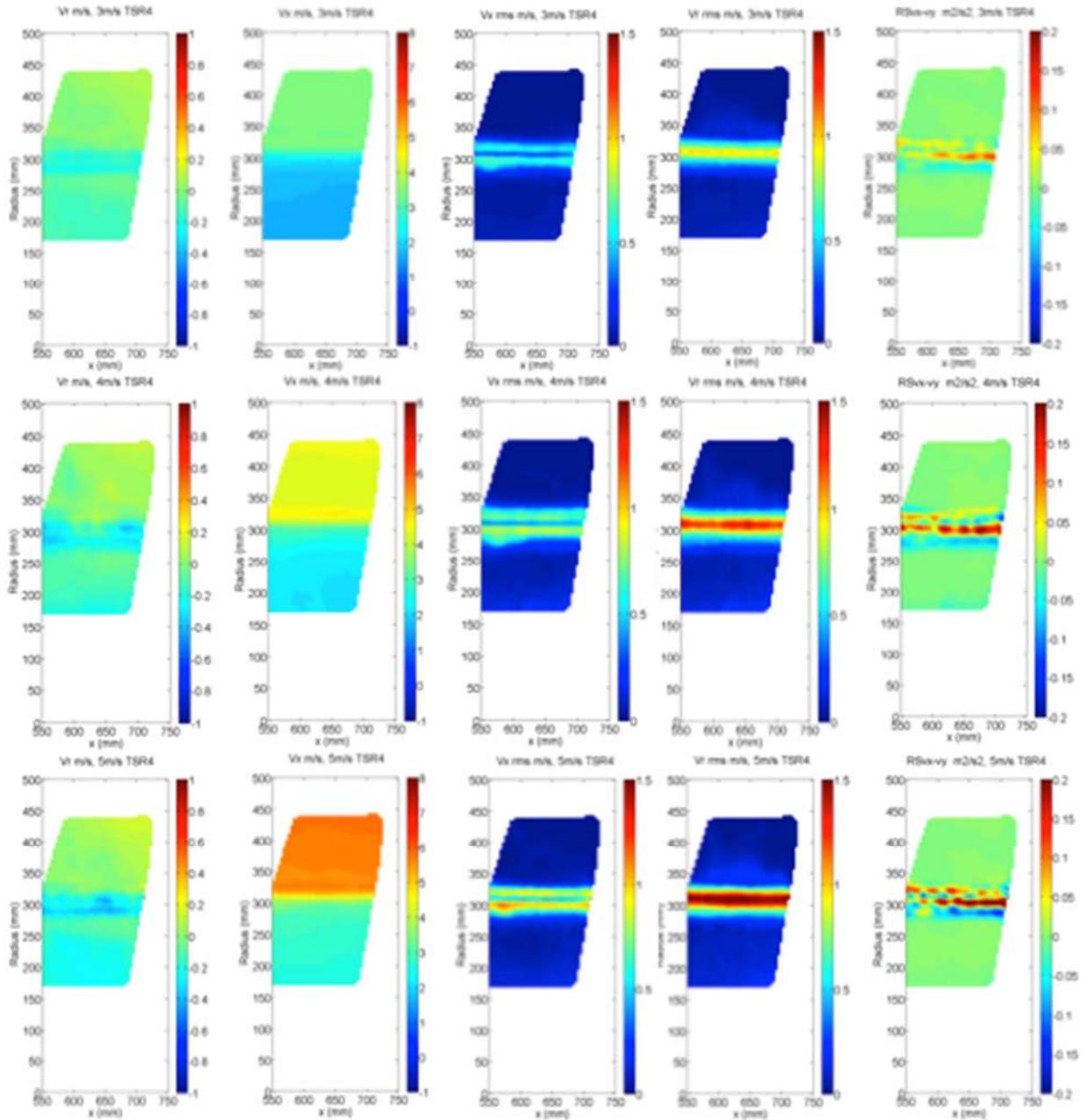
Figure 51. Planar PIV flow mapping at one rotor diameter downstream.
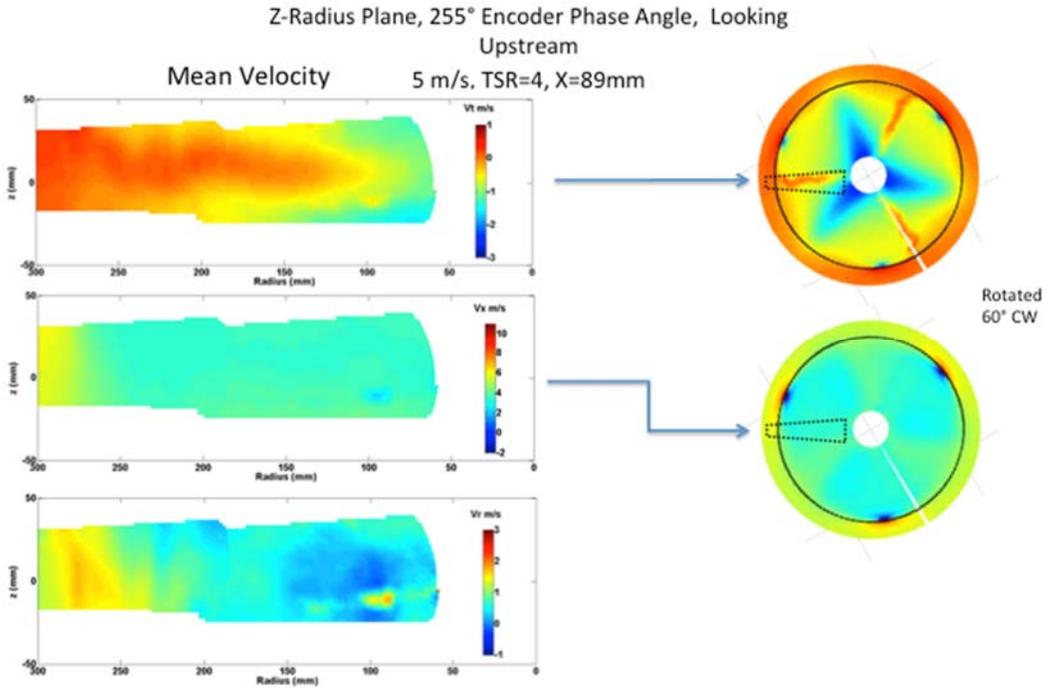
Figure 52. Mean velocity stereo PIV mapping at X = 89 mm with comparison to encoded LDV measurements.

a)
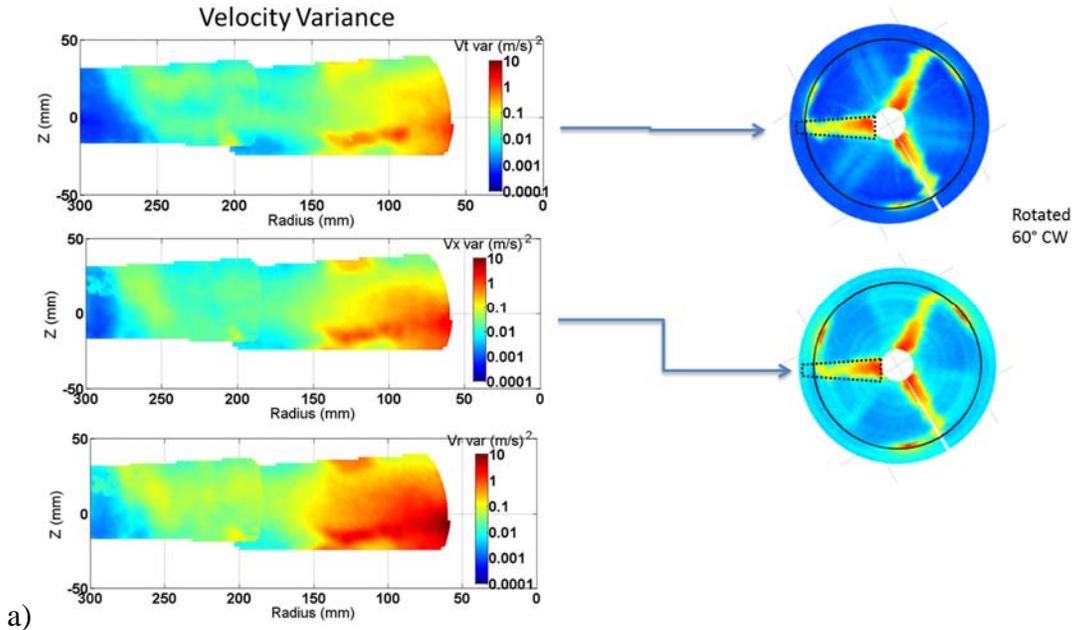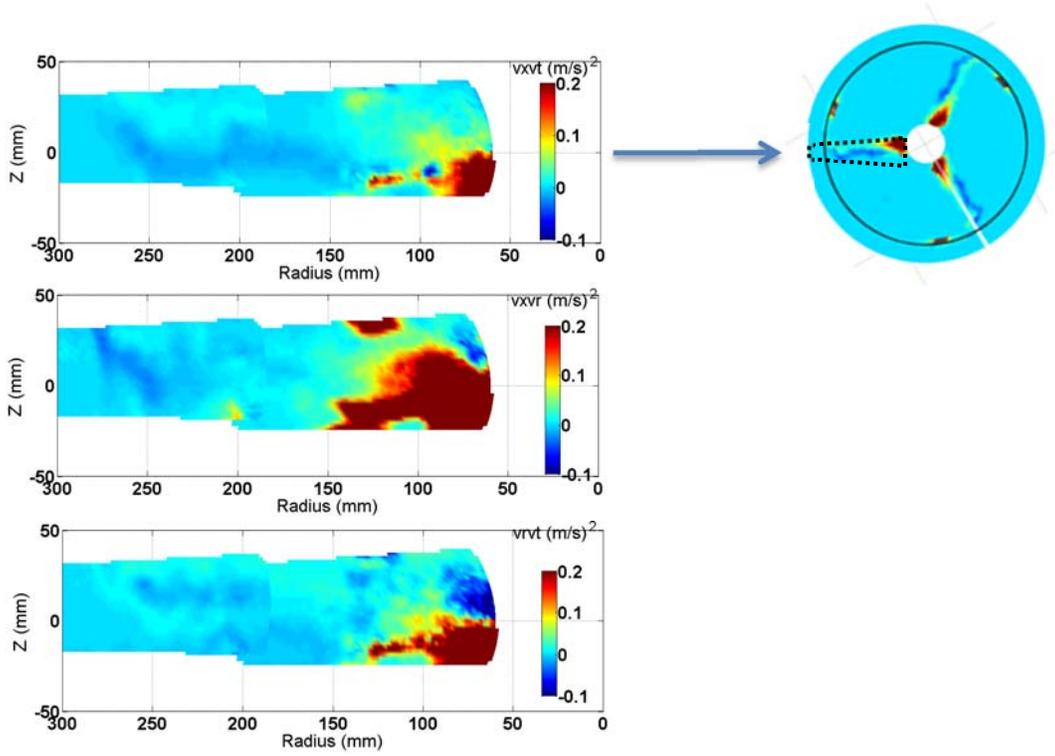
b)

Figure 53. Velocity Reynolds Stresses measured with Stereo PIV at x = 89 mm with comparison to encoded LDV measurements. Same data as shown in Figure 52. a) normal stresses, b) shear stresses.
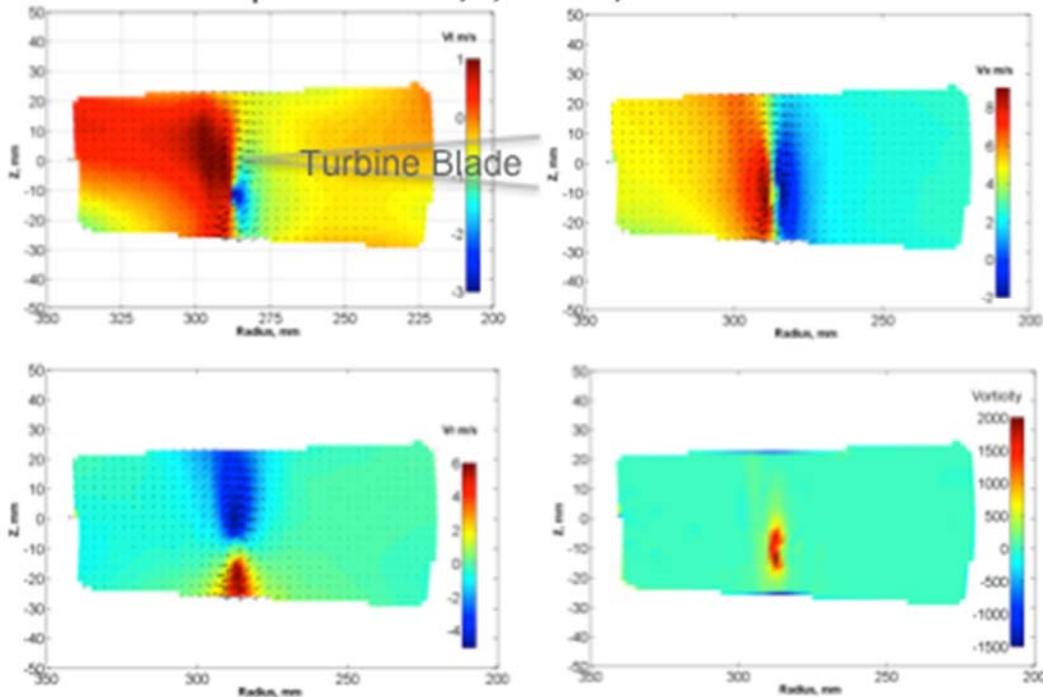
Figure 54. Stereo PIV mapping of tip vortex flow field at X = 63.5 mm under non-cavitating tip vortex conditions, V_x inflow of 4 m/s.

Acoustics Results

The turbine was installed on the shaft and operated at the TSR=4. The absolute pressure in the tunnel was 310 kPa. Figure 55 shows the radiated sound after applying the array calibration curve for the turbine for a sequence of speeds. Although in general the levels increase with increasing speed, there are subtleties that need to be pointed out. Although we see that the spectra from 2.0 m/s to 3.55 m/s exceed the background, these signals are still influenced by other mechanical sources such as the dynamometer drivetrain within the water tunnel. Only when the speed reaches 4 m/s do we have signal above the other tunnel sources. Conversely for speeds of 4.5 m/s and higher the turbine is cavitating. Since we are interested only in a non-cavitating signature within the scope of this project, we only obtained usable spectra at 4.0 m/s.

As a final check for signal-to-noise ratio, the turbine was removed and a bare hub was installed. Figure 56 shows a comparison between the turbine and bare hub at the same rpm. We can see from this plot that there is signal for most of the spectrum. There are background correction routines that can be used to correct the hydrophone levels. However, since some power was required to spin the bare hub, this may have introduced some motor noise that was not present during the motor generation. Thus the spectrum presented in Figure 56 is an upper bound to the radiated sound.
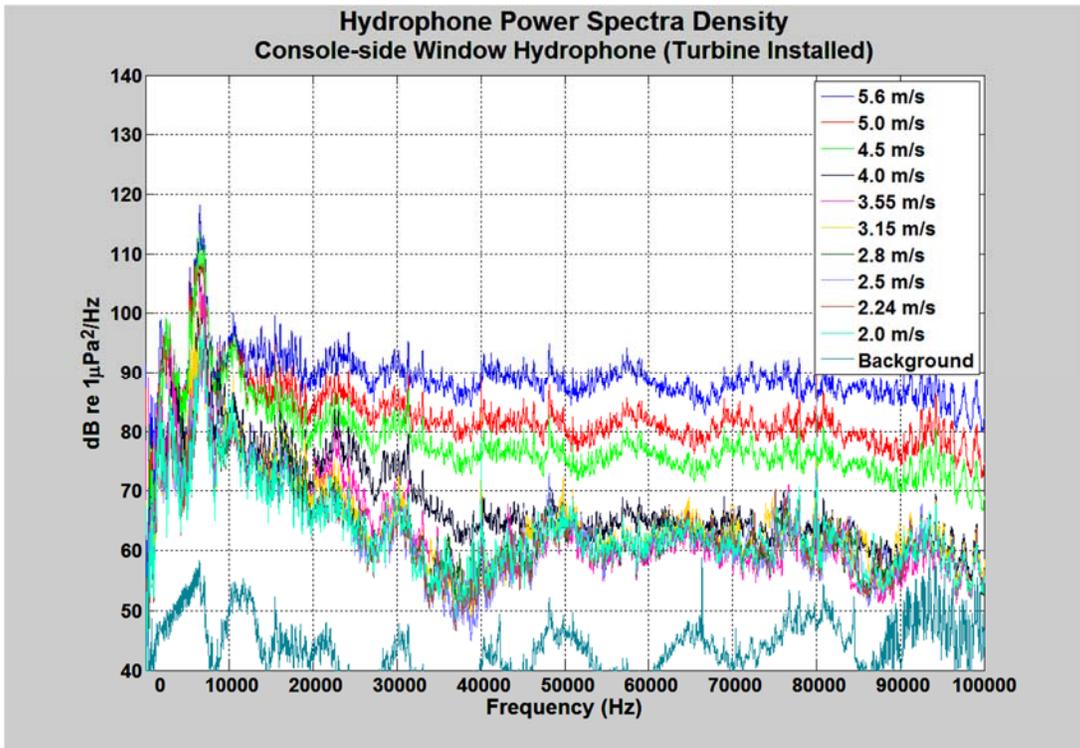
Figure 55. Radiated sound power spectral density at 1 m for the turbine for tunnel speeds between 2.0 m/s and 5.6 m/s. The case for 0 m/s and 0 rpm (background) is also shown. For all cases the TSR=4.0.
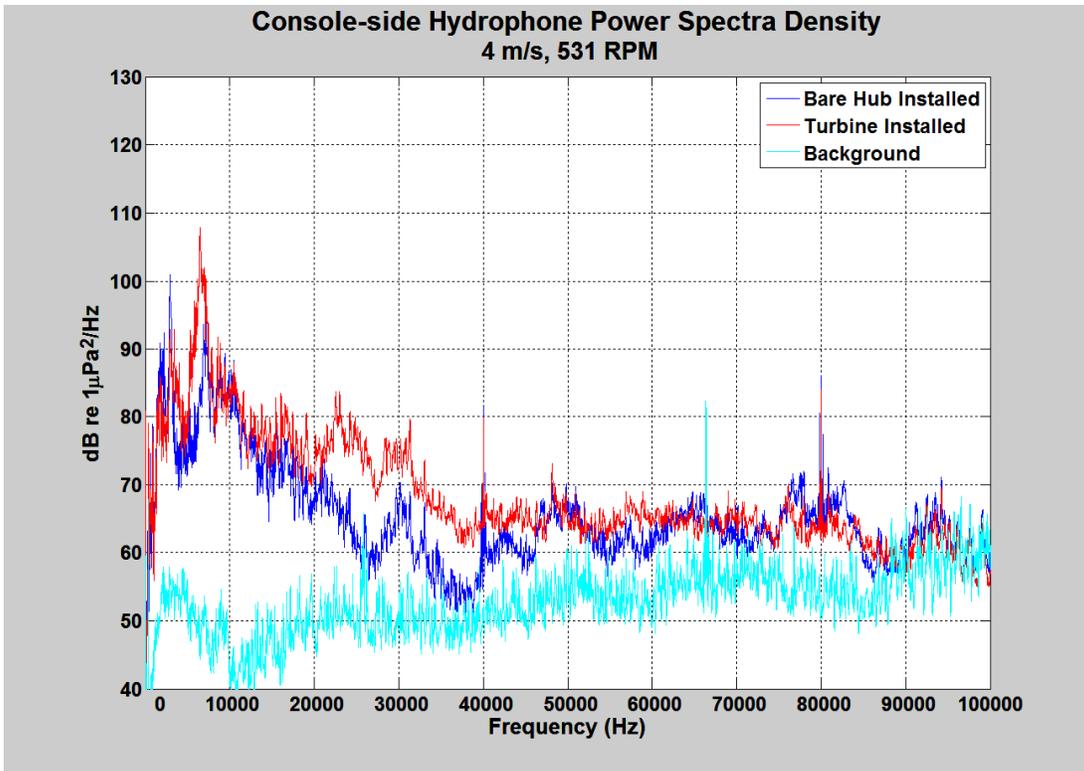
Figure 56. Comparison of turbine sound to bare hub at 4 m/s, TSR=4.0.

Figure 57 shows the corresponding turbine sound in one-third octave bands. This spectrum lacks significant levels at low frequency. This is caused by the absence of the inflow turbulent boundary layer that would be typical of normal installation on the bottom of a river or tidal region. Hence, the spectrum shown would be considered due only to trailing edge excitation. Based on Figure 56, the upper frequency of Figure 57 was limited to 40 kHz due to signal to noise.
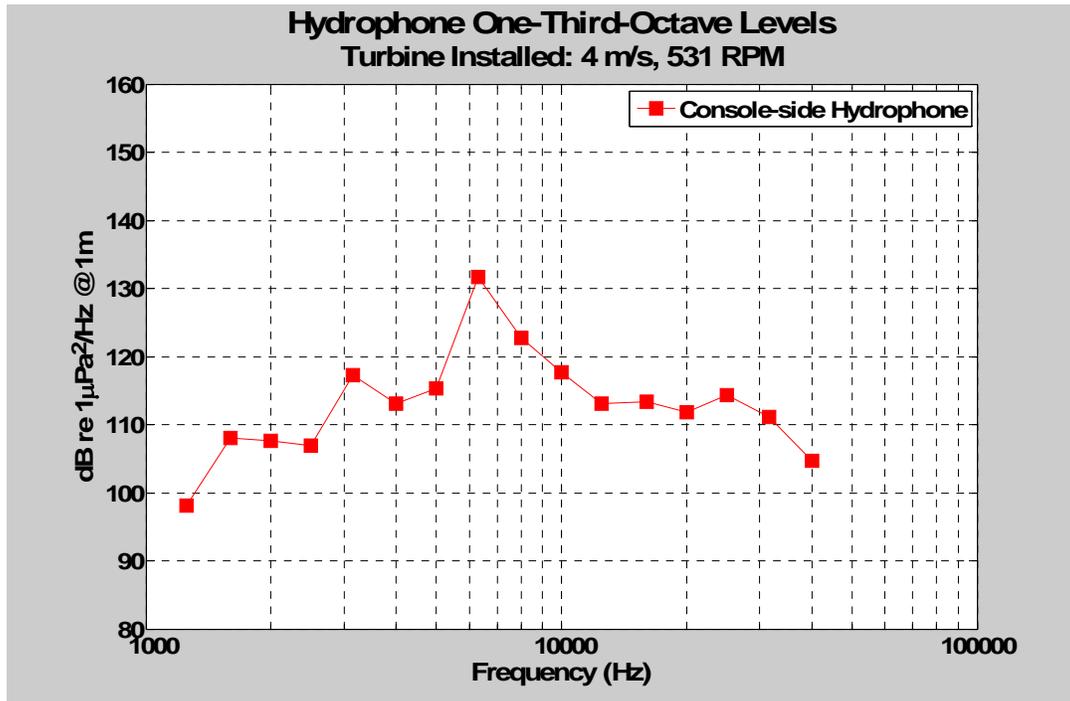
Figure 57. Radiated sound power of turbine in one-third octave levels for 4 m/s and 531 rpm.

Flow Visualization

Mini-tuft and surface paint flow visualization tests were performed at the end of the test program. The mini-tuft flow visualization was performed by gluing small fiber filaments to the tower as shown in Figure 58. The tunnel was brought up to operating conditions and the dynamics of the tufts were recorded on video. In general, the mini-tufts indicated an unsteady separation pattern on the downstream side of the tower. The tufts were oriented in the flow direction along the top of the tower. Nacelle directed flow is observed in the tower wake region (downstream side of the tower) over the inner 50% span of the blade. This inner radius flow did have occasional flow reversal. The outer span flow appeared to be more chaotic with both nacelle and window directed flow oscillations occurring roughly 50% of the time. Figure 59 shows a still image of the mini-tuft behavior at V_x = 5 m/s and a TSR = 4.

Surface paint flow visualization was used to assess the flow field in the close vicinity of the turbine blades. The resulting paint patterns of the skin friction lines aid in the visualization of flow features such as surface (limiting) streamlines and presence of separation. Details of this

testing method including theory, descriptions of its application and interpretation is documented in Zierke, et al. [53]. Basically, oil - based artist paint was mixed with 80w-90 gear oil and applied to the blade surface in small dots or blobs prior to filling the tunnel with water, as shown in Figure 60. The use of multiple colors enables identification of flow patterns and mixing by complex flow structures. After paint application, the tunnel flow is initiated to desired operating conditions quickly. The shear stress in the flow carries the oil-paint mixture establishing a persistent pattern on the surface of the blade. This process typically took a few minutes of operation at the desired test conditions. Once the paint streaklines reached the desired level of "movement", the tunnel was quickly shut down and drained to photograph the paint flow patterns on the model. Figure 61 shows representative photographs of the paint flow patterns observed on the model rotor. The resulting pictures illustrate a well - behaved flow pattern. The flow appeared to be axial and attached along most of the blade span. No excessive separation (lines) were observed in the patterns on the blades. As expected there was a small region of separation near the trailing edge and almost no migration of paint from suction to pressure surface or onto the flatback region of the blade. The provided data base includes all photos taken of the paint flow visualization test as well as the mini-tuft video.
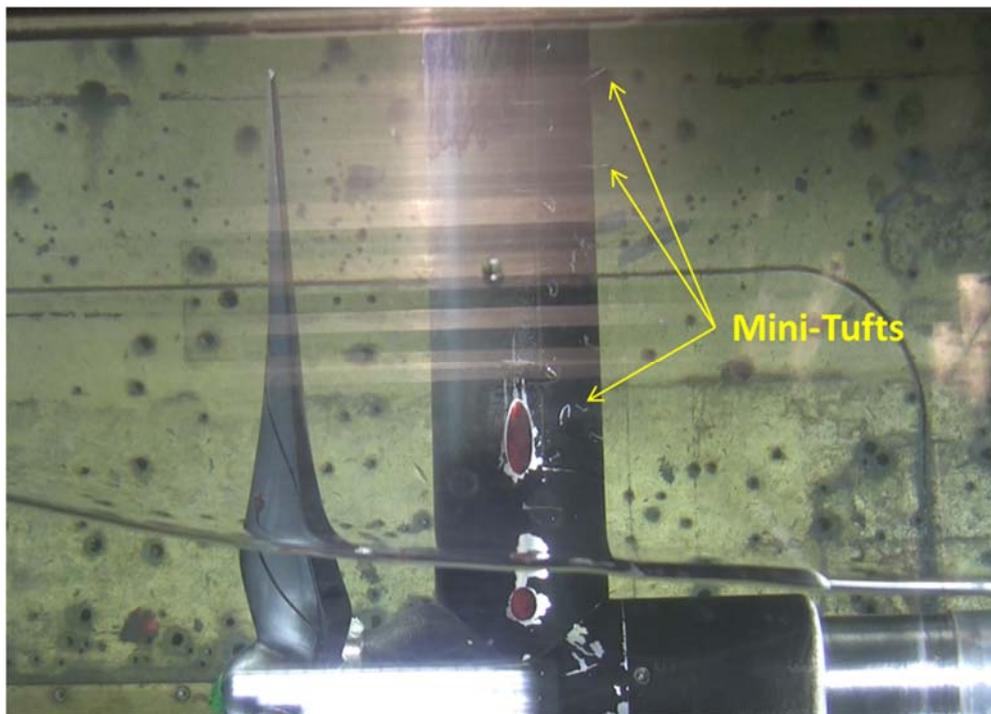
Figure 58. Mini-tuft application on the tower.
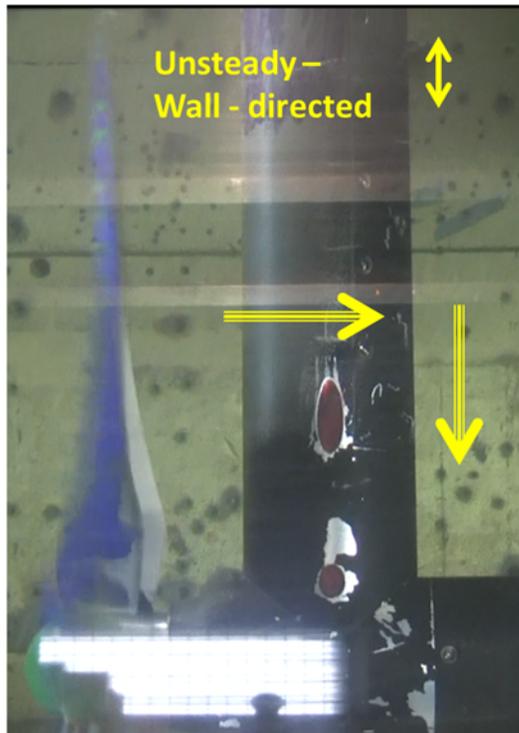
Figure 59. Mini-tuft behavior under flow conditions of V_x=5m/s and TSR=4.
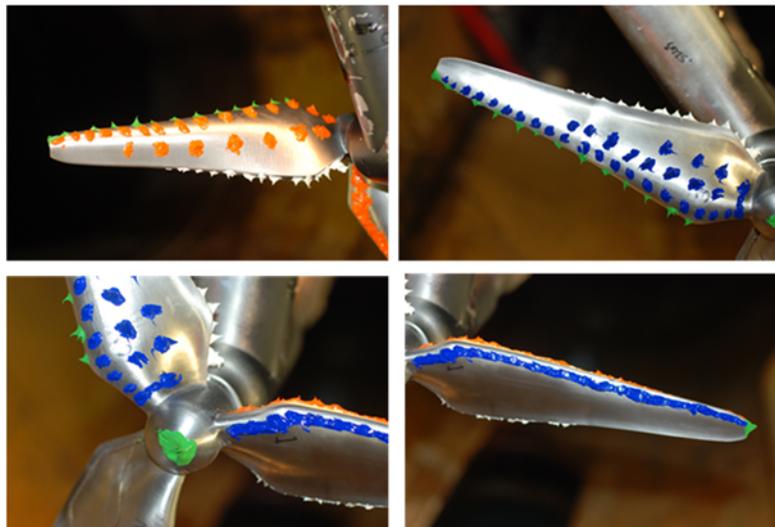
Figure 60. Application of paint/oil mixture for surface flow visualization.

Figure 61. Representative paint flow features on the model rotor after testing at V_x = 5 m/s and TSR = 4.

Uncertainty

General Uncertainty
Data uncertainty was estimated following standard guidelines [53-55].

The random error uncertainty in the higher order velocity statistics can be estimated using the approach of Benedict and Gould [56]. Their results, which focused on a practical means to estimate the uncertainty in turbulence statistics, used results from statistical theory for large samples. Only the contribution of random error to the uncertainty is treated in these estimates. The random error P of an estimate is usually small when the sample size, N, is large. The random error in the estimate of the variance of a velocity component V is given by Benedict and Gould [56] and Garcia, $et\ al.$ [57]:

$$P_{V-variance} = 1.96 \sqrt{\frac{\mu_4 - \left(\sigma_V^2\right)^2}{N}}$$

where μ_4 is the 4th order central moment of the variable V and σ_V^2 is the variance of the sample. The 4th order moment is estimated from the flatness factor result in the velocity component data set, for each data point in the field. To find the uncertainty in the estimate of velocity rms, we use variance = σ_V^2 to propagate the error in the velocity variance through to the velocity rms using:

$$P_{V\text{-variance}} = \vartheta_{rms}P_{rms}$$

where ϑ_{rms} is the sensitivity coefficient, $\vartheta_{rms} = \partial P_{V\text{-}Variance}/\partial\ \sigma_V = 2\sigma_V$. The uncertainty in the velocity component rms estimate is thus:

$$P_{V-RMS} = \frac{1.96}{2\sigma_V} \sqrt{\frac{\overline{u^4} - \left(\overline{u^2}\right)^2}{N}}$$

where u is the component of velocity. Note that this uncertainty is a function of $\overline{u^4}$, the fourth central moment of the velocity. Using a similar analysis, Benedict and Gould [57] show that the Reynolds stress uncertainty due to random error is given by:

$$P_{V-uv} = 1.96 \sqrt{\frac{\overline{u^2v^2} - \left(\overline{uv}\right)^2}{N}}$$

The uncertainty in the mean vorticity can be estimated by propagating the errors in mean velocity and position through the equation used to estimate vorticity:

$$\omega_y = \frac{\Delta u}{\Delta z} - \frac{\Delta w}{\Delta x}$$

The result is given by:

$$\sigma_{\omega_y} = \sqrt{\left(\frac{\sigma_{\Delta u}}{\Delta z}\right)^2 + \left(\frac{\sigma_{\Delta w}}{\Delta x}\right)^2 + \left(\frac{\Delta u}{\Delta z^2}\sigma_{\Delta z}\right)^2 + \left(\frac{\Delta w}{\Delta x^2}\sigma_{\Delta x}\right)^2}$$

The velocity uncertainties are found using the approach given above, while the uncertainties in x and z are assumed to be dominated by the magnification uncertainty.

The post-processing code used these last two expressions to estimate the uncertainties for the velocity standard deviation and Reynolds stress.

LDV
The velocity uncertainty includes contributions from both bias and precision errors associated with the measurement system and the flow. An LDV system measures the velocity of a particle traversing through an alternating pattern of light and dark interference fringes. The spacing between the fringes and dimensions of the probe volume are determined by the transmitting optics of the LDV system and the input laser beam diameter and spacing. The light by a particle moving through this fringe pattern creates an oscillating electrical signal via a photo-detector (photo-multiplier tube). The frequency of the modulation was determined with TSI FSA3500 Signal Processor for each particle passing through the probe volume that generates a signal of sufficient strength. The velocity is proportional to the measured frequency and the proportionality constant is the fringe spacing, D_f.

$$V = f_D * D_f \tag{1}$$

V is the velocity perpendicular to the interference fringes, f_D is the measured Doppler frequency with the frequency shift removed. The fringe spacing, $D_f = \lambda/(2\sin(\kappa))$, is determined by the half angle between the focused laser beams, κ, and the wavelength of light used, λ.

Fringe Spacing and Frequency Uncertainty
Uncertainty error in LDV measured velocities arises from several sources. The fringe spacing and the measured Doppler frequency are possible sources of uncertainty. The fringe spacing is essentially the calibration constant of the instrument. The uncertainty in the measured velocity values due to these factors is estimated from:

$$\sigma_V = \left[\left(\theta_{f_D} \sigma_{f_D} \right)^2 + \left(\theta_{D_f} \sigma_{D_f} \right)^2 \right]^{1/2} \tag{2}$$

The sensitivity coefficients θ_{fD} and θ_{Df} are the partial derivatives of f_D and D_f with respect to V in equation 1:

$$\theta_{f_D} = \partial f_D \Big/ \partial V = D_f; \quad \theta_{Df} = \partial D_f \Big/ \partial V = f_D \tag{3}$$

The fringe spacing was estimated directly by using a rotating disc. The velocity of the surface of the disc is known accurately. The estimated fringe spacing uncertainty is 0.5% of the value. The fringe spacing is listed in Table 5. The difference in the fringe spacing estimates is due primarily to the wavelength given D_f is proportional to wavelength. Other factors affecting the difference in D_f between the two channels include small differences in the spacing and direction of the laser beams input to the lens in both velocity channels and the focal length of the lens at each wavelength will be slightly different due to chromatic aberration. The rotating disk calibration process accounts for these effects.

Normalizing equation (2) by V provides the relative uncertainty equation:

$$\sigma_v\!\big/\!_V = \left[\left(\left\{\sigma_{f_D}\right\}\!\big/\!_{f_D}\right)^2 + \left(\left\{\sigma_{D_f}\right\}\!\big/\!_{D_f}\right)^2\right]^{1/2} \qquad (4)$$

The frequency error is based on the signal processor performance. The manufacturer's stated resolution is 0.05% of reading and $\pm$0.025% of reading uncertainty is used.

Equation (4) was used to compute the uncertainty in V due to the terms equation (1). As one might expect from the numbers the dominant term is the uncertainty in the fringe space and σ_V/V = 0.0050.

Sampling Biases
The probability of obtaining a sample in a short time interval is proportional to the velocity with the LDV system as it was used in the current experiment. This leads to a velocity bias because the sampling process is over weighted toward higher velocities in an unsteady flow. The effects of this bias on the measured statistics depend on the range of velocity fluctuations, the mean value, and the form of the velocity distribution function. A transit time weighting was used as the velocity bias correction and this is the preferred velocity bias correction discussed in the literature. In general, the bias in the mean is expected to be approximately equal the turbulence intensity squared. Previous studies by the author have found this relationship is reasonably accurate. This estimate of the bias is used to quantify uncertainty in this analysis. The measured mean velocity in a flow with a 10% turbulence intensity (local velocity magnitude based intensity) results in a bias in the mean that is $0.1^2 = 0.01$ times the local velocity magnitude. The bias correction would, ideally, reduce this bias to zero in the computed statistics. But a bias correction may not work well all the time and such corrections can over correct. It is assumed the uncertainty in the mean values due to velocity bias is reduced by 2× by using the bias correction. Previous study has shown the bias levels out as turbulence levels exceed 30% and a 10% maximum bias in the mean is expected at such high levels. Therefore, a 5% bias error is maximum that is considered possible after correction. No preferred sign is assumed give a correction can over correct as noted.

Another sampling bias includes gradient effects. No attempt to estimate or correct for gradient bias has been made directly. However, it should be noted that the velocity bias correction has been shown to be an effective gradient bias correction.

Fringe bias is the result of a non-uniform probability of obtaining a velocity measurement from a particle passing through the probe as a function of the particle direction. Frequency shifting reduces fringe bias. Frequency shifting involves altering the frequency of one of the two laser beams in each velocity channel with a Bragg cell. The result is the fringe pattern in the probe

volume is not stationary and the fringes sweep past a fixed point with the shift frequency. Frequency shifting is essential to LDV for other reasons than just fringe bias. Just as velocity bias requires the flow to be unsteady and present a range of velocities, fringe bias requires variation in the flow direction or the potential for the bias is not significant. Increasing the directional variation and velocity in the flow requires greater amounts of frequency shifting to avoid a bias. In the current pipe flow, the axial mean velocity is large relative to the other velocities and the deviation of the flow direction from the mean U vector direction should be small, under 15 degrees. Therefore the potential for fringe bias is small and the frequency shifting used reduces this potential bias further. Based on this assessment, it is assumed fringe bias effects are negligible.

Noise

Noise affects the ability to accurately estimate the Doppler frequency in LDV. The primary noise source is the photomultiplier tubes (PMT). Reflections from surfaces, bubbles or solid particulates in the flow can cause noise that exceeds normal operation. Under normal operation, a noise floor is established by shot noise in the PMT and how the signal processor deals with this noise. For a backscatter LDV, this noise floor is typically around 0.7% and lower turbulence levels (based on the local velocity magnitude) cannot be resolved.

Noise can also contribute to the uncertainty in the mean velocity. Noise can create outliers. Typically, outliers should fall on either side of the mean and, in this case, the mean is not likely to be affected significantly but the precision error, as noted in the next section, will be increased. In general, the mean is a robust parameter in this regard. However, it is possible that outliers may occur on primarily one side of the velocity distribution. Strong reflections, for example, create noise that appears as false zero velocity values. In such cases, the noise will bias the estimated mean value. Unfortunately, it is difficult to quantify the influence of noise in the data in a way that translates into a rigorous or meaningful error bar for either the mean velocity or the velocity fluctuation rms estimates. Fortunately, the data set includes information that can be used to at least flag data points where the noise affects may be significant. The rms is much more susceptible to noise in these instances and will always be falsely increased. The data set includes the velocity minimum and maximum in both velocity channels and the normalized 3rd and 4th order central moments. These higher order moments are the skewness factor and the kurtosis (flatness) factor. In this flow, these factors should not deviate substantially from their Gaussian values. If the flatness value exceeds 4 or the skewness is farther from zero by more than ±1 for the data sampled at a given measurement location, one should consider these data carefully as there could be noise contamination unless high flatness or skewness values may be expected based on flow characteristics. One or two outliers can cause this type of spike in skewness and flatness. In such cases the mean and, often, the rms are not substantially affected – if the data fit the trend well, the estimated mean and rms are probably good estimates. If one considers the velocity maximum and minima in the collection of data taken at a location in question with one or more of these skewness or flatness flags, it is likely that at least one value is too extreme to be realistic and these data should be considered questionable. Outliers can influence Reynolds shear stress estimates reducing the estimated value due to the de-correlated noise.

<u>PIV Uncertainty</u>

The uncertainty in the mean velocity estimate obtained from DPIV measurements has many possible contributors. Random errors and bias errors contribute to the overall uncertainty and each of these depends critically on optical setup (seeding density, illumination uniformity, etc.) as well as the image pair processing algorithm (primarily peak locking). The total uncertainty in the mean velocity is computed in the usual manner:

$$\sigma = [B^2 + P^2]^{1/2}$$

The random error in the mean velocity at each point was computed as $P_{V-mean} = \dfrac{1.96\sigma_V}{\sqrt{N}}$, where N

is the number of valid velocity samples at each point in the field. The bias error estimate for the single velocity sample was used for *B*.

The ITTC 25th Specialist Committee on Uncertainty Analysis published procedure 7.5-01-03-03 [58] and the 26th ITTC Specialist Committee on Detailed Flow Measurements published a committee report[59] on the uncertainty assessment of PIV that is both up-to-date and compliant with industry standards in regards to uncertainty analysis methodologies. The uncertainty in the estimated particle displacements determined by PIV image analysis includes both precision and bias errors. Each velocity component is computed from the displacement estimate using the following relationship:

$$V_i = \Delta s_i * M / \Delta T \text{ where } M \equiv L_o/L_{i.}$$

The laser pulse delay, ΔT, is assumed known with a specific uncertainty and *M* is the image magnification, defined as the ratio of L_o (the object calibration length in test units of length) and L_i (the image calibration length in pixels). The uncertainty in *M* is related to the calibration process. The current PIV uncertainty guide provides procedures for defining the uncertainties in ΔT and *M*. The particle displacement, Δs_i, is typically measured as a statistical mean particle displacement of *N* number of particles in a small interrogation region (IR) of the two double-pulsed images. Many algorithms are available to estimate the mean displacement in an IR ranging from tracking individual particles, to FFTs, to direct spatial cross-correlation. The latter two are the most commonly used. In either case, the displacement in pixels is estimated using the location of the cross correlation peak. Several other important factors, such as resolution error of the displacement engine, peak locking, perspective distortion, and image spatial resolution, may contribute to displacement uncertainty.

The resolution of the PIV correlation algorithm is but one component of the total uncertainty in the displacement measurement. The minimum possible displacement resolution is affected by the ability of the processing algorithm to precisely determine the location of the cross correlation peak. The system vendors typically report displacement resolution error on the order of 1/20 to 1/10 of a pixel, depending on the peak finding algorithm used to process the image data. However, this minimum uncertainty is dependent on the quality of the particle images (geometry, uniformity and brightness), particle image size (pixels), the number of the particles in the IR (particle density), out-of-plane particle motion between laser pulses, and details of analysis

algorithm used. These factors typically increase displacement uncertainty above that often stated by the PIV manufacture and can vary across test installations.

Another contribution to displacement uncertainty arises in biasing peak location estimation. This peak locking bias pulls displacement estimates toward integer pixel values in the correlation map displacement space. For example, it is observed in some cases that displacement estimates obtained for a uniform sub-pixel displacement of 0.5 pixels and 0.5 pixels in the X and Y directions, respectively, show the greatest amount of scatter, compared to other uniform sub-pixel displacements. This displacement error is due to the tendency of the four integer corners to pull the displacement estimates away from the input displacement at the center of the pixel array of the correlation map, as shown in Figure 62. Studies have shown that this peak locking bias error is a function of the sub-pixel particle displacement and particle image size. A small sub-pixel displacement (<0.3 pixels) can be preferentially pulled toward one pixel, while a large sub-pixel displacement (>0.7) can lock the displacement to the next pixel. This effect can have a significant impact on both the mean velocity and higher order statistics.
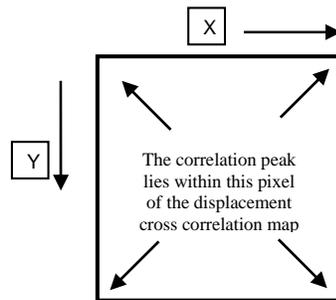
Figure 62. Illustration of the peak-locking effect.

A general guideline suggests that particle image sizes of at least 2 pixels and less than 10 pixels can minimize peak locking [60]. However, it is not always possible to control particle image size due to other constraints on image field-of-view (FOV), magnification, and particle size needed to accurately follow the fluid motion. As a result, the impact of peak locking on displacement uncertainty must be assessed. Particle density has been shown to impact bias and rms displacement errors [60-62]. High particle densities (>10) can significantly reduce rms error. However, peak locking bias errors can increase with increasing particle density and densities of ~ 5 per IR are recommended in the event peak locking bias is a concern.

Investigators have used computer generated synthetic particle images to assess displacement accuracy. The EUROPIV Synthetic Image Generator is a sophisticated generator capable of simulating particle size, seeding density and image intensity. An alternative approach that has been found to work well in quantifying these effects on the displacement uncertainty including the impact of peak locking is to use images acquired during testing to digitally create image pairs with known displacements. This procedure involves generating a pseudo image pair using a MATLAB-based image processing code to displace an acquired image A to a specified displaced location B. This displaced pseudo image B is then analysed using the PIV processing algorithms

used to reduce the data. This procedure includes any effects of the camera and imaging optics, the particle seed and seed density, and the illumination and window distortions (if any). The seed and illumination aspects coupled with the camera response are believed to be critical to the applicability of the results to the experiment. Not included in this pseudo image pair approach are the effects of out-of-plane particle motion and flow gradients. These are factors the can affect the quality of the correlations but are spatial resolution and flow related bias issues and not specific to the correlation algorithms peak finding accuracy.

To assess the contribution of peak locking to both bias and random uncertainty, pseudo image pairs are created over a range of uniform sub-pixel displacements. For each pseudo image pair, the local error between the uniform displacement and the displacement engine estimate is computed, forming a displacement error ensemble for each sub pixel displacement. Performing this analysis over a range of uniform sub-pixel displacements provides a peak locking bias error sensitivity to sub-pixel displacement, allowing for a more general definition of this bias error. This technique also provides the spatial distribution of this error over the 2-D image plane where variations in laser light intensity or image distortion (like barrel distortion or window effects) may impact the magnitude of this bias. This technique does not account for intensity variations between the two laser pulses.

The scatter in the displacement estimates in the pseudo image pair results yields an estimate on the precision error. The size of the interval containing 95% of the estimated displacements, D_{95}, indicates that free of any bias error, a displacement estimate will lay within D_{95} pixels of the true value 95% of the time. The relative significance of the displacement uncertainty is a function of the velocity, the time between laser pulses and the magnification. This is unlike the magnification uncertainty which is a fixed percentage of the velocity regardless of these factors. For example, with a defined velocity and ΔT, the precision displacement uncertainty is larger at a lower M than at a higher M where the measured Δs_i is larger with the higher M then at the lower M.

The scatter in the displacement estimates arises from noise distorted by peak locking bias. The measured pixel displacement (velocity) rms is related to this noise contaminated measured value and the true rms as follows:

$$rms_{MEASURED}^2 - rms_{NOISE}^2 = rms_{TRUE}^2$$

In a high turbulence region, such as in a jet or wake, the noise contamination bias of the rms is fairly inconsequential, but this error can be relatively large at lower turbulence levels. Cases in which the displacements due to turbulence span a range of just a few pixels on the correlation map can experience pixel locking from 16 or 30 integer nodes distributed across the data, as shown in Figure 63. In this case, the peak locking bias effect on the mean and rms is expected to be substantially reduced as these influences should average out. This assessment of underlying noise establishes the noise floor of the system, including imaging, seed and processing below which turbulence levels cannot be measured. It should be noted that other factors such as spatial resolution and peak locking can and do have a large impact on the rms estimates.
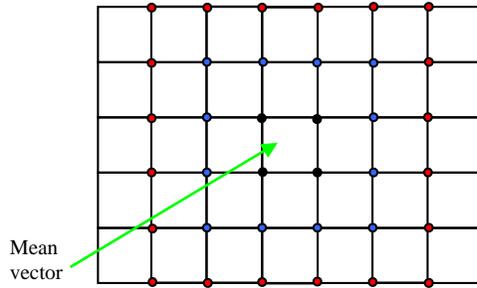
Figure 63. The number of integer displacements influencing the data increases quickly as the data distribution expands beyond one pixel.

Estimating a combined uncertainty due to the bias and scatter in the displacements observed in the pseudo image pair results, assuming a standard error propagation approach, is not valid in all cases. There are two issues. First, the bias and the scatter could be coupled. Second, the results show that the peak locking bias can act systematically and the influence of peak locking is not random such that it will average out or diminish with increased sample size. However, the direction of peak locking bias in either velocity component can be positive or negative and the bias can be a random factor that averages out under the right circumstances.

Propagating bias and scatter using values from the pseudo image analysis is appropriate in high turbulence regions, but should be done with care in low turbulence regions. If the majority of the particle displacements at one location in the flow deviate from the mean displacement by only a small amount, low turbulence, such that the data fall inside of 1 pixel on the correlation map, peak locking bias effects will be severe. In this case, the effects of peak locking do not average out because it repeats on average very well in the data. The result is the possible bias expected in the mean value is as large as the largest possible bias seen in the pseudo image analysis. These two limiting cases can be termed low pixel level turbulence and high pixel level turbulence. In high pixel level turbulence, 16 or more integer displacement nodes can influence the results and peak locking affects are expected to average out.

A common sign of peak locking bias in a vector map is the banding or segmenting of the velocity statistics around pixel displacement values. The probability density function (PDF) of the sub-pixel displacement field will show preferential grouping at integer pixel displacements instead of a relatively flat distribution. The level of peak locking can be estimated by calculating the center of mass of the sub-pixel displacement PDF and then applying the following equation:

$$PL=4*(0.25-PDF_{CenterofMass}) \text{ (Lavision, Inc)}$$

A PL value of 0 implies no peak locking. A value of PL=1 indicates strong peak locking. Peak locking is considered to be relatively weak for PL<0.1. A regular mosaic pattern in the vorticity field computed from the velocity field can also be an indication of peak locking.

The pseudo image pair results can provide some guidance regarding the influence of peak locking on the rms for low pixel turbulence cases. The scatter in the pseudo image pair results due to the precision with which the correlation peak can be located is much like the scatter in the

displacements that would result from low levels of turbulence. A specified displacement at the center of the sub-pixel displacement results in an increase in the rms of the data scatter compared to the mean rms values for all the displacements considered. Displacements near integer locations should reduce calculated rms levels due to peak locking.

Perspective effects can also bias the particle displacement estimates. The section on particle displacement uncertainty above considers only those sources due to the image analysis, not significant distortion of the images. This distortion bias is due to a combination of the change in the viewing angle over the FOV and the thickness of the light sheet. A particle moving from one side of the laser light sheet to the other side between laser pulses with no displacement in the plane of the laser sheet will appear to the camera to have moved in the X and/or Y directions due to perspective effects even though $\Delta X = \Delta Y = 0$. This error is smaller on the axis of the camera or near the center of the FOV due to the smaller receiving collection angle.

In practice, particles at the edges of the light sheet will not be visible and PIV data is weighted toward brighter particles that are nearer to the center of the light sheet. Displacements normal to the light sheet larger than half the sheet thickness should lead to dropouts a large fraction of the time and it is reasonable to assume the maximum perspective effects are about 2X less than the estimates made above using the full light sheet width. Raffel *et al*. (1998) provide a summary of this error. Perspective bias adds a false displacement as seen by the camera when it occurs (away from the center of the FOV). However, the sign of the displacement depends on whether the flow is moving in +Z or −Z normal to the light sheet plane. This out-of-plane motion can be expected to be random with a zero mean and no skew if the flow is symmetric about the light sheet. In this case, the bias in the mean velocity will be zero. The bias will make some velocity fluctuations seem larger than they actually were and the rms values will be biased high as a result. However, rigorously quantifying these effects on the rms is difficult.

The spatial resolution of displacement estimate fields is defined by the size of the interrogation region (IR). Low-pass spatial filtering of the estimated velocity field can occur if the local length scale of the velocity gradients is smaller than the IR size. It is difficult to assess the impact of poor spatial resolution on displacement uncertainty since this impact is dependent on the particle density, flow gradient scale relative to the IR size, and degree of particle spatial homogeneity. A spatially inhomogeneous particle distribution across the IR, or the grouping of particles in a high speed gradient relative to a low speed gradient, can impose a velocity bias in the estimated statistical displacement over the IR. Furthermore, small gradients can impact peak locking bias and rms. Very small gradients relative to the IR size can have minimal impact on bias and rms. However, as the gradient increases in scale, yet still smaller than the size of the IR, bias and rms error increase.

An uncertainty procedure for SPIV would for the most part follow a similar process as defined for planar PIV. The calibration procedure is more complex in SPIV requiring either a multi-plane target or multiple target images with a target displacement. As a result, the estimation of calibration uncertainty can be more involved. Several researchers have been developing calibration techniques focused on reducing calibration error and eliminating the need for a target [61-64]. The dual camera setup will, however, reduce the effect of the perspective error described in section 6.3.4 [65]. In addition, the "averaging" effect of the two cameras in

computing the two in-plane velocity components will in general reduce the statistical uncertainty in these components. The estimation of the uncertainty in the out-of-plane component can be obtained by performing error propagation on stereo-imaging reconstruction equations used to compute the third velocity component. Prasad [66] provides a detailed discussion on the SPIV technique. Lawson and Wu [67, 68] provide a guideline for estimating SPIV error. The third component out-of-plane error can be reduced to slightly higher than the uncertainty in the in-plane components but is typically on the order of 2 to 4 times the in-plane error.

Peak locking will also impact the overall uncertainty in SPIV if it occurs. In a similar fashion to the image displacement technique described above for planar PIV, Elbing *et al*. [69] are developing a dual camera SPIV 3-axis image-displacement technique to estimate SPIV uncertainty and the impact of peak locking.

SUMMARY

ARL Penn State collaborated with Sandia National Laboratories and the University of California at Davis to design, fabricate (at a 1:8.7 scale), and experimentally test a new marine hydrokinetic (MHK) turbine. The turbine design process focused on incorporating advanced design concepts to 1) improve structural performance, 2) reduce sensitivity to surface fouling, 3) improve cavitation performance and 4) incorporate anti-singing trailing edge design for hydro applications. A flat-back foil design was incorporated to improve blade structural response to load while minimizing impact to the blade aero/hydro performance. The main objective of the program was to perform a V&V quality dataset of the scaled turbine at both scale size and flow conditions to maintain an acceptable range of Re # scaling. The currently available history of device testing and data set availability for model validation are lacking in detail and often suffer from Re # scaling deficiencies to offer a strong V&V data set for model validation. A secondary objective of the program was to provide a public database suitable for formal V&V studies in evaluating low-, mid-, and high-fidelity design and analysis codes used for MHK device design.

This V&V dataset includes turbine powering performance characterization, as well as cavitation-inception and cavitation-breakdown performance. Powering data were directly measured with an inline motor-generator and also inferred through a Torque * RPM calculation. All data were acquired with shaft encoder position for phase averaging. Steady state drive shaft loading was measured providing time mean and phase-encoded mean shaft thrust and torque along with the two components of bending moments measured at the rotor to drive shaft attachment plane. Unsteady measurements of driveshaft loading, blade strain, tower pressures, and radiated noise were also measured. Detailed flow field mapping of the rotor inflow, rotor through flow and turbine wake were performed using LDV, planar PIV, and SPIV. The detailed quantitative flow field data were complemented by flow-field visualization using high-speed video and surface-flow visualization using mini tufts and an oil-paint method on the rotor blades, turbine nacelle and downstream turbine tower. These state-of-the-art measurements demonstrate much of the complex physics associated with the flow through an unducted, horizontal-axis turbine.

The test data set including model cad drawings of the turbine and model install in the tunnel will be publically available on a SNL open website for modelers to access in use of a V&V program.

Appendix 1

LDV Variable definition

Table 12. LDV Variable Definition.		
Name	**Meaning**	**Units**
xloc(mm)	Axial location	mm
Theta(deg)	Phase encoder angle 0° aligned with tower. Meaningless in Time averaged and set to 0	deg
R_H2O(mm)	Radial position measured postive outward from hub.	mm
Vz_mean(m/s)	Vertical mean velocity component postive up. Also tangential component positive in clockwise rotation looking upstream. See figure to right.	m/s
Vx_mean(m/s)	Axial mean velocity component	m/s
Vz_min(m/s)	vertical velocity minimum	m/s
Vx_min(m/s)	Axial velocity minimum	m/s
Vz_max(m/s)	vertical velocity maximum	m/s
Vx_max(m/s)	Axial velocity maximum	m/s
Vz_variance(m^2/s^2)	vertical velocity variance	m^2/s^2
Vx_variance(m^2/s^2)	Axial velocity variance	m^2/s^2
Vz_skewness	vertical velocity skewness	
Vx_skewness	Axial velocity skewness	
Vz_kurtosis	vertical velocity flatness	
Vx_kurtosis	Axial velocity flatness	
Vz_TurbInt	vertical velocity TI	
Vx_TurbInt	Axial velocity TI	
Vz_npnts	vertical velocity # points used in statistics	
Vx_npnts	Axial velocity # points used in statistics	
Vz_perc_filt(%)	vertical velocity % noise filtered	
Vx_perc_filt(%)	Axial velocity % noise filtered	
vzvx_cov(m^2/s^2)	Reynolds Stress $v_z v_x$	m^2/s^2
vzvx_MRNormalStress_ max(dynes/cm^2)	Principal maximum normal stress	dynes/cm^2
vzvx_MRNormalStress_ min(dynes/cm^2)	Principal minimum normal stress	dynes/cm^2
vzvx_MRShearStress(dynes/cm^2)	Principal shear stress	dynes/cm^2
vzvx_MRRotationAngle (degrees)	Principal stress angle	deg
Vt (tangential velocity in cylindrical coordinates) : Vt = + or - Vz depending on orientation of LDV probe (see notes in summary sheet) θ is cicumferential or tangential coord measured positive counterclockwise looking upstream. θ=0 located on tower - aligned with tower.		

PIV Variable definition

	Table 13. PIV variable definition.	
Variable Name	**Meaning**	**Units**
Alpha	circumferential degree in cylindrical coords.	radians
Alphadeg	circumferential degree in cylindrical coords.	degrees
Nellipse	# of prinicpal stress levels used in elliptic noise filtering	
PSNmax12	Max principle normal stress, channels 1&2	m^2/s^2
PSNmax13	Max principle normal stress, channels 1&3	m^2/s^2
PSNmax32	Max principle normal stress, channels 3&2	m^2/s^2
PSNmin12	Min principle normal stress, channels 1&2	m^2/s^2
PSNmin13	Min principle normal stress, channels 1&3	m^2/s^2
PSNmin32	Min principle normal stress, channels 3&2	m^2/s^2
PSS12	Principle Shear stress, channels 1&2	m^2/s^2
PSS13	Principle Shear stress, channels 1&3	m^2/s^2
PSS32	Principle Shear stress, channels 3 & 2	m^2/s^2
Radius	Radius in cylindrical coords	mm
Ufilt_unc_tot	Velocity mean channel 1 uncertainty	m/s
Ufiltstd_unc	Velocity STD channel 1 uncertainty	m/s
Vfilt_unc_tot	Velocity mean channel 2 uncertainty	m/s
Vfiltstd_unc	Velocity STD channel 2 uncertainty	m/s
Vrfilt	Processed Radial Velocity component mean	m/s
Vrfiltstd	Processed Radial Velocity component STD	m/s
Vtfilt	Processed Tangential/Circumferential Velocity component mean	m/s
Vtfiltstd	Processed Tangential/Circumferential Velocity component STD	m/s
Vxfilt	Processed Axial Velocity component mean	m/s
Vxfiltstd	Processed Axial Velocity component STD	m/s
Vyfilt	Processed Y Velocity component mean	m/s
Vyfiltstd	Processed Y Velocity component mean	m/s
Vzfilt	Processed Z Velocity component mean	m/s
Vzfiltstd	Processed Z Velocity component STD	m/s
Wfilt_unc_tot	Velocity mean channel 3 uncertainty	m/s
Wfiltstd_unc	Velocity STD channel 3 uncertainty	m/s
Xfilt	Processed X coordinate	mm
Xscale	X scale factor for processing	mm
Yfilt	Processed Y coordinate	mm
Yscale	Y scale factor for processing	mm
Zfilt	Processed Z coordinate	mm

count	# of ensembles used to compute statistics	1/s
dudxfilt	du/dx gradient in measured coordinates	1/s
dudyfilt	du/dy gradient in measured coordinates	1/s
dvdxfilt	dv/dx gradient in measured coordinates	1/s
dvdyfilt	du/dy gradient in measured coordinates	1/s
dwdxfilt	dw/dx gradient in measured coordinates	1/s
dwdyfilt	dw/dy gradient in measured coordinates	1/s
inputParameters	used by matlab processign routine to read Davis raw data files	
ufiltavg	Channel 1 velocity mean	m/s
ufiltflat	Channel 1 velocity flatness	
ufiltskew	Channel 1 velocity skewness	
ufiltstd	Channel 1 velocity rms	m/s
uvfilt	Channel 1 & 2 Reynolds shear stress	$(m/s)^2$
uvfilt_unc	Channel 1 & 2 Reynolds shear stress uncertainty	$(m/s)^2$
uwfilt	Channel 1 & 3 Reynolds shear stress	$(m/s)^2$
uwfilt_unc	Channel 1 & 3 Reynolds shear stress uncertainty	$(m/s)^2$
vfiltavg	Channel 2 velocity mean	m/s
vfiltflat	Channel 2 velocity flatness	
vfiltskew	Channel 2 velocity skewness	
vfiltstd	Channel 2 velocity rms	m/s
vorticityfilt	Channel 1 & 2 vorticity calculation	1/s
vorticityfilt_unc	Channel 1 & 2 vorticity calculation uncertainty	1/s
wfilt	Channel 3 velocity	
wfiltavg	Channel 3 velocity mean	m/s
wfiltflat	Channel 3 velocity flatness	
wfiltskew	Channel 3 velocity skewness	
wfiltstd	Channel 3 velocity rms	m/s
wvfilt	Channel 2 & 3 Reynolds shear stress	$(m/s)^2$
wvfilt_unc	Channel 2 & 3 Reynolds shear stress uncertainty	$(m/s)^2$
xfilt	measured x coordinate	mm
yfilt	measured y coordinate	mm
zfilt	measured z coordinate	mm

lower case variables (x, y, z) or U, V, W correspond to measured variables in camera / calibration coordinates (highlighted in yellow).		
Upper case variables (X, Y, Z, Radius, Alpha); Vx, Vr, Vy, Vz, Vt, Processed variables transformed to rotor coordinate system (highlighted in light blue).		
filt label on variables indicates elliptic or histogram noise filtering was performed --> Xfilt, Ufilt etc.		
Measured Coords:	chn 1 --> x, U	This corresponds to Y or Radius, Vy or Vr. Tower is on positive Y side at Z=0.

	Chn 2 --> y, V	This corresponds to Z or Alpha, Vz or Vt. Note Alpha is defined postiive in clockwise direction looking upstream (rotor rotation direction)
	Chn 3 --> z, W	This corresponds to axial coordinate X, VX

Analog Signal Variable definition

The analog signal data files include both SI and English units.

Table 14. Analog signal variable definition – Time averaged data – Low acquisition rate system		
Variable Name	**Units**	**Notes**
RunNumber	ND	run number from test
TurbineDiameter	mm	Rotor diameter
WaterTemperature	F	Water temp.
DyneSpeed	RPM	Dynamometer shaft speed
DyneTorque	ft-lb	Dynamometer shaft torque
DynePower	hp	Direct dynamometer shaft power to grid
CSTotal	psia	Keil probe total pressure console side
RSTotal	psia	Keil probe total pressure road side
P_30	psia	Wall static pressure @ 0.762 m (30")
P_54	psia	Wall static pressure @ 1.371 m (54")
P_80	psia	Wall static pressure @ 2.032 m (80")
P_66_CU	psia	Wall static pressure @ 1.68 m (66") console upper
P_66_RU	psia	Wall static pressure @ 1.68 m (66") road upper
P_111	psia	Wall static pressure @ 2.82 m (111")
RPM	RPM	Shaft speed
Density	slug/ft^3	water density
Viscosity	ft^2/s	water kinematic viscosity
VaporPressure	psia	water vapor pressure
ShaftPosition	deg	shaft encoder position
P_T	psia	mean total pressure
P_S	psia	mean wall static pressure @ 1.68 m (66")
Vinf	fps	Reference velocity @ 1.68 m (66")
Vinf_mps	mps	Reference velocity @ 1.68 m (66")
V_tunnel	fps	Reference velocity @ 0.254 m (10")
Vtunnel_mps	mps	Reference velocity @ 0.254 m (10")
sigma	ND	cavitation number
TSR	ND	Tip speed ratio
Q	ft-lb	ARL shaft torque
C_Q	ND	Torque coefficient (arl sensor)
T	lb	ARL thrust sensor
C_T	ND	Thrust coefficient (arl sensor)

P	hp	Direct dynamometer shaft power to grid
C_P	ND	Power coefficient
Q_Nm	N-m	ARL shaft torque
DyneTorque_Nm	N-M	Dynamometer torque
npnts	ND	# points in stats.
P_10	psia	Wall static pressure @ 0.254 m (10")
P_88	psia	Wall static pressure @ 2.235 m (88")
Qdyne_RPM	HP	Power Torque*rpm (dynamometer sensor)
Q_RPM	HP	Power Torque*rpm ARL sensor)
CP_Qdyn_rpm	ND	Power coefficient (Torque*rpm (Dyno sensor - Vtunnel)
CP_q_RPM	ND	Power coefficient (Torque*rpm ARL sensor)
CQ_dyne	ND	Torque Coefficient (dyno sensor - Vtunnel)
CT_zero_corr	ND	Thrust coefficient zero correction (Vtunnel)
modelPressCorr	lbs	Thrust model pressure correction
CT_modelPresCorr	ND	Thrust coefficient for model press corr. Thrust (Vtunnel)
CT_modelPresCorr_V80	ND	Thrust coefficient for model press corr. Thrust (V80)
CP_Qdyn_rpm_Vinf	ND	Power coefficient (Vinf)
Vel80	fps	Velocity @ 2.032 m (80")
CP_Qdyn_rpm_V80	ND	Power coefficient (V80)
Vel66	fps	Velocity @ 1.68 m (66")
Vel30	fps	Velocity @ 0.762 m (30")
Vel54	fps	Velocity @ 1.371 m (54")
Vel111	fps	Velocity @ 2.82 m (111")
Vel10	fps	Velocity @ 0.254 m (10")
Vel88	fps	Velocity @ 2.235 m (88")
tau	ND	Vel111/V_tunnel
U_3/U_2	ND	Used in blockage correction - eigenvalue solver
A/C	ND	Used in blockage correction - eigenvalue solver
Eqn A.4- Eqn A.2=0	ND	Used in blockage correction - eigenvalue solver
U_1 /U_2	ND	Used in blockage correction - eigenvalue solver
U_T/U_2	ND	Used in blockage correction - eigenvalue solver
U_1/U_T	ND	Used in blockage correction - eigenvalue solver
U_T/U_F	ND	Blockage correction factor
C_P_F	ND	Blockage corrected Power Coef.
C_T_F	ND	Blockage corrected thrust Coef.
TSR_F	ND	Blockage corrected TSR
U3/UT	ND	Used in blockage correction - eigenvalue solver
Tau-U3/UT	ND	Error minimized in blockage corr. Solver

Variable Name	Units	Notes
Angle	deg	encoder phase angle
TurbineDiameter	ft	Rotor diameter
TurbineArea	ft^2	Rotor area
WaterTemperature	F	Water temp.
DyneSpeed	RPM	Dynamometer shaft speed
DyneTorque	ft-lbs	Dynamometer shaft torque
DynePower	hp	Direct dynamometer shaft power to grid
P_delta	psid	Pitot probe delta pressure ==> 0.254 m (10")
CSTotal	psia	Keil probe total pressure console side
RSTotal	psia	Keil probe total pressure road side
P_30	psia	Wall static pressure @ 0.762 m (30")
P_54	psia	Wall static pressure @ 1.371 m (54")
P_80	psia	Wall static pressure @ 2.032 m (80")
P_66_CU	psia	Wall static pressure @ 1.68 m (66") console upper
P_66_RU	psia	Wall static pressure @ 1.68 m (66") road upper
P_111	psia	Wall static pressure @ 2.82 m (111")
RPM	RPM	Shaft speed
Density	slug/ft^3	water density
Viscosity	ft^2/s	water kinematic viscosity
VaporPressure	psia	water vapor pressure
ShaftPosition	deg	shaft encoder position
P_T	psia	mean total pressure
P_S	psia	mean wall static pressure @ 1.68 m (66")
Vinf	fps	Reference velocity @ 1.68 m (66")
Vinf_mps	mps	Reference velocity @ 1.68 m (66")
V_tunnel	fps	Reference velocity @ 0.254 m (10")
Vtunnel_mps	mps	Reference velocity @ 0.254 m (10")
sigma	ND	cavitation number
TSR	ND	Tip speed ratio
Q	ft-lbs	ARL shaft torque
C_Q	ND	Torque coefficient (arl sensor)
T	lbf	ARL thrust sensor
C_T	ND	Thrust coefficient (arl sensor)
P	hp	Direct dynamometer shaft power to grid
C_P	ND	Power coefficient
Q_Nm	N-m	ARL shaft torque
DyneTorque_Nm	N-m	Dynamometer torque
P_10	psia	Wall static pressure @ 0.254 m (10")

Table 15. Analog signal variable definition – Phased averaged data – Low and high acquisition rate system combined.

P_88	psia	Wall static pressure @ 2.235 m (88")
Qdyne_RPM	hp	Power Torque*rpm (dynamometer sensor)
Q_RPM	hp	Power Torque*rpm ARL sensor)
CP_Qdyn_rpm	ND	Power coefficient (Torque*rpm (Dyno sensor - Vtunnel)
CP_q_RPM	ND	Power coefficient (Torque*rpm ARL sensor)
CQ_dyne	ND	Torque Coefficient (dyno sensor - Vtunnel)
CT_zero_corr	ND	Thrust coefficient zero correction (Vtunnel)
modelPressCorr	lb	Thrust model pressure correction
CT_modelPresCorr	ND	Thrust coefficient for model press corr. Thrust (Vtunnel)
CT_modelPresCorr_V80	ND	Thrust coefficient for model press corr. Thrust (V80)
CP_Qdyn_rpm_Vinf	ND	Power coefficient (Vinf)
Vel80	fps	Velocity @ 2.032 m (80")
CP_Qdyn_rpm_V80	ND	Power coefficient (V80)
Vel66	fps	Velocity @ 1.68 m (66")
Vel30	fps	Velocity @ 0.762 m (30")
Vel54	fps	Velocity @ 1.371 m (54")
Vel111	fps	Velocity @ 2.82 m (111")
Vel10	fps	Velocity @ 0.254 m (10")
Vel88	fps	Velocity @ 2.235 m (88")
tau	ND	Vel111/V_tunnel
SS_npnts	ND	Steady State number of ensembles in stats
PTower40	psia	Unsteady tower pressure @ 42% span
PTower70	psia	Unsteady tower pressure @ 74% span
PTower100	psia	Unsteady tower pressure @ 106% span
PTower110	psia	Unsteady tower pressure @ 117% span
TAccel_x	g	Tri-axial accelerometer
TAccel_y	g	Tri-axial accelerometer
TAccel_z	g	Tri-axial accelerometer
c_PTower40	ND	Unsteady pressure coef. Tower pressure @ 42% span
c_PTower70	ND	Unsteady pressure coef. Tower pressure @ 74% span
c_PTower100	ND	Unsteady pressure coef. Tower pressure @ 106% span
c_PTower110	ND	Unsteady pressure coef. Tower pressure @ 117% span
ShaftMomA	ft-lbs	Shaft mom-cell A
ShaftMomB	ft-lbs	Shaft moment-cell B
ShaftMomAFilt	ft-lbs	high -pass (> 2Hz) filtered shaft moment - A
ShaftMomBFilt	ft-lbs	high -pass (> 2Hz) filtered shaft moment - B

Q_ftlbs	ft-lbs	ARL Torque cell
T_lbs	lbf	ARL thrust cell
StrainMid1	strain	Blade strain rosette 1 - mid span
StrainMid2	strain	Blade strain rosette 2 - mid span
StrainMid3	strain	Blade strain rosette 3 - mid span
StrainMid_p	strain	Blade Principal strain P - mid span
StrainMid_q	strain	Blade Principal strain Q - mid span
StrainHub1	strain	Blade strain rosette 1 - 25% span
StrainHub2	strain	Blade strain rosette 2 - 25% span
StrainHub3	strain	Blade strain rosette 2 - 25% span
StrainHub_p	strain	Blade Principal strain P - 25% span
StrainHub_q	strain	Blade Principal strain Q - 25% span
StressMid_p	psia	Blade Principal Stress P - mid span
StressMid_q	psia	Blade Principal Stress Q - mid span
StressHub_p	psia	Blade Principal Stress P - 25% span
StressHub_q	psia	Blade Principal Stress Q - 25% span
PhiMid_pq	deg	Principal strain angle - mid span
PhiHub_pq	deg	Principal strain angle - 25% span
Dyne_npnts	ND	Unsteady points per encoder bin angle

Table 16. Analog signal variable definition – formulas.		
Variable Name	**Formula String**	**Units**
Density	rho	slugs/ft^2
Viscosity	gnu	ft^2/sec
VaporPressure	pvap	psia
ShaftPosition	EncoderPosition	deg
P_T	(CSTotal+RSTotal)/2	psia
P_S	(P_66_CU+P_66_RU)/2	psia
Vinf	12*sqrt(abs(P_T-P_S)/(0.5*rho))	fps
Vinf_mps	Vinf/3.28084	mps
V_tunnel	12*sqrt(abs(P_delta)/(0.5*rho))	fps
Vtunnel_mps	V_tunnel/3.28084	mps
V_80	12*sqrt(abs(P_T-P_80)/(0.5*rho))	fps
V_80_mps	V_80/3.28084	mps
sigma	144*(P_S-pvap)/(0.5*rho*Vinf^2)	ND
TSR	pi*RPM*PropDiameter/60/Vinf	ND
Q	D117386/ShaftTorqueThrust_sens	ft-lbf
C_Q	Q/0.25/rho/PropArea/PropDiameter/Vinf^2	ND
T	D116625_3/ShaftTorqueThrust_sens	lbf
C_T	T/0.5/rho/PropArea/Vinf^2	ND

P	DynePower	HP
C_P	550*P/0.5/rho/PropArea/Vinf^3	ND
Q_Nm	Q*1.35582	N-m
DyneTorque_Nm	DyneTorque*1.35582	N-m
Qdyne_RPM	DyneTorque*RPM/5252	HP
Q_RPM	Q*RPM/5252	HP
CP_Qdyn_rpm	550*-1*Qdyne_RPM/0.5/rho/PropArea/V_tunnel^3	ND
CP_q_RPM	550*-1*Q_RPM/0.5/rho/PropArea/V_tunnel^3	ND
CQ_dyne	DyneTorque*-1/0.25/rho/PropArea/PropDiameter/V_tunnel^2	ND
CT_zero_corr	T*-1/0.5/rho/PropArea/V_tunnel^2	ND
modelPressCorr	(P_S-P_80)*3.977	lbf
CT_modelPresCorr	(T-modelPressCorr)*-1/0.5/rho/PropArea/V_tunnel^2	ND
CT_modelPresCorr_V80	(T-modelPressCorr)*-1/0.5/rho/PropArea/V_80^2	ND
CP_Qdyn_rpm_Vinf	550*-1*Qdyne_RPM/0.5/rho/PropArea/Vinf^3	ND
Vel80	12*sqrt(abs(P_T-P_80)/(0.5*rho))	fps
CP_Qdyn_rpm_V80	550*-1*Qdyne_RPM/0.5/rho/PropArea/Vel80^3	ND
Vel66	12*sqrt(abs(P_T-P_S)/(0.5*rho))	fps
Vel30	12*sqrt(abs(P_T-P_30)/(0.5*rho))	fps
Vel54	12*sqrt(abs(P_T-P_54)/(0.5*rho))	fps
Vel111	12*sqrt(abs(P_T-P_111)/(0.5*rho))	fps
Vel10	12*sqrt(abs(P_T-P_10)/(0.5*rho))	fps
Vel88	12*sqrt(abs(P_T-P_88)/(0.5*rho))	fps
tau	Vel111/V_tunnel	ND

Appendix 2
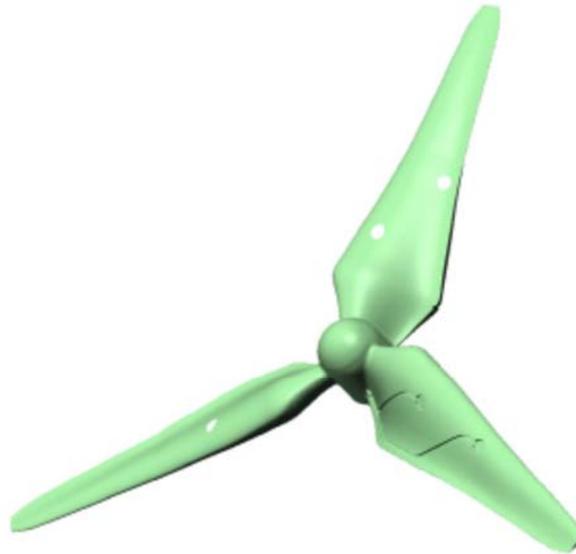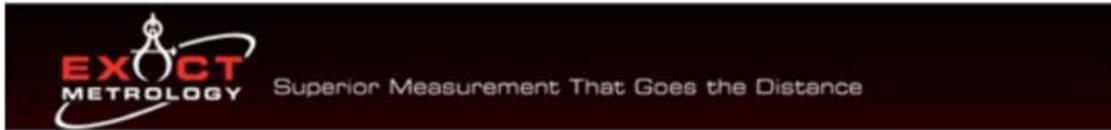
Prepared For: Penn State
                      Richard S. Meyer
                      (814) 865-9634
                      rsm2@arl.psu.edu

Prepared By: Matthew Martin
                      513-831-6620
   matthewm@exactmetrology.com

Part Inspected: 146452

**Inspection Device Used:** Breuckmann

Report Units: Inches

Table Type	Data Color Map (Reference Surface)
Cmp Object(s)	12A388CBS.stl
Ref	146452.x_t
Alignment	best-fit to surfaces (3)

#Points	490372
Mean	-0.003
StdDev	0.013

REFERENCES

1   Johnson, E, Fontaine, A. A., Jonson, M. L., Meyer, R. S., Straka, W. A., Young, S. A., van Dam, C. P., Shiu, H. and Barone, M.," A1:8.7 scale water tunnel test of an axial flow water turbine," Proceedings of the 1rst Marine Energy Technology Symposium, METS13, Washington Dc, 2013.
2   U.S. Department of Energy Water Power Program, http://www1.eere.energy.gov/water/hydrokinetic/, accessed January 2, 2013.
3   Johnstone, C. M., Pratt, D., Clarke, J. A., Grant, A. D., 2013, "A techno-economic analysis of tidal energy-technology," *Renewable Energy*, 49, pp. 101-106.
4   Hernandez-Sanchez, B. A., 2011, "Biofouling and corrosion monitoring of MHK technology," *SAND2011-2568C*.
5   Miller, D., Mandell, J. F., Samborsky, D. D., Hernandez-Sanchez, B. A., Griffith, D. T., 2012, "Performance of composite materials subjected to salt water environments," *53rd AIAA/ASME/ASCE/AHS/ASC Structures, Structural Dynamics, and Materials Conference*, Honolulu, HI, USA, April 23-26, pp. AIAA-2012-1575.
6   Copping, A. E., Cada, G., Roberts, J., Bevelhimer, M., 2010, "Accelerating ocean energy to the marketplace – environmental research at the U.S. Department of Energy national laboratories," *3rd International Conference on Ocean Energy*, October 6.
7   Yang, Z., Wang, T., Copping, A. E., 2013, "Modeling tidal stream energy extraction and its effects on transport processes in a tidal channel and bay system using a three-dimensional coastal ocean model," *Renewable Energy*, 50, pp. 9.
8   Kadiri, M., Ahmadian, R., Bockelmann-Evans, B. Rauen, W., Falconer, R., 2012, "A review of the potential water quality impacts of tidal renewable energy systems," *Renewable and Sustainable Energy Reviews*, 16(1), pp. 329-341.
9   Jeffrey, H., Sedgwick, J., 2011, "ORECCA European offshore renewable energy roadmap," *ORECCA Project*.
10   Arvesen, A., Hertwich, E. G., 2012, "Assessing the life cycle environmental impacts of wind power: A review of present knowledge and research needs," *Renewable and Sustainable Energy Reviews*, 16(8), pp. 5994-6006.

11 Powles, S.J.R., "Effects of tower shadow on the dynamics of a horizontal-axis wind turbine," *Wind Eng.*, v7n1, pp26-42, 1983.

12 Thresher, R.W., Wroght, A.D., and Hershberg, "A computer analysis of wind turbine blade dynamic loads," *J. Solar Energy Eng.,* v108n1, pp17-25, 1986.

13 Wang, T. and Coton, F.N., "An unstgeady aerodynamic model for HAWT performance including tower shadow effects," *Wind Eng.*, v23n5, pp 255-268, 1999.

14 Wang, T. and Coton, F.N., "A high resolution tower shadow model for downswind wind turbines," *Wind Eng.*, v89, pp873-892, 2001.

15 Butterfield, C.P., Musial, W. P., Scott, G.N. and Simms, D.A., "NREL combined experiment final report-Phase II," NREL/TP-442-4807, 1992.

16 Ocean Renewable Power Company, http://www.orpc.co, accessed January 2, 2013.

17 Salter, S. H., 2012, "Are Nearly all Tidal Stream Turbine Designs Wrong?," *4th International Conference on Ocean Engineering*, October 17, Dublin, Ireland.

18 Bernitsas, M. M., Raghavan, K., Ben-Simon, Y., Garcia, E. M. H., 2008, "VIVACE (Vortex Induced Vibration Aquatic Clean Energy): A New Concept in Generation of Clean and Renewable Energy From Fluid Flow," J. *Offshore Mech. Arct. Eng.*, vol. 130, no. 4, p. 041101.

19 Khan, M. J., Bhuyan, G., Iqbal, M. T., Quaicoe, J. E., 2009, "Hydrokinetic Energy Conversion Systems and Assessment of Horizontal and Vertical Axis Turbines for River and Tidal Applications: A Technology Status Review," *Applied Energy*, vol. 86, no. 10, pp. 1823–1835.

20 Ecomerit Technologies, http://www.ecomerittech.com/aquantis.php, January 2, 2013.

21 Bahaj, A. S., Molland, A. F., Chaplin, J. R., Batten, W. M. J., 2007, "Power and thrust measurements of marine current turbines under various hydrodynamic flow conditions in a cavitation tunnel and a towing tank," *Renewable Energy*, 32, pp. 407-426.

22 Somers, D. M., "S830, S831, and S832 Airfoils: November 2001-November 2002," NREL/SR-500-36339, Aug. 2005.

23 Timmer, W. A. and van Rooij, R. P. J. O. M., "Summary of the Delft University Wind Turbine Dedicated Airfoils," 8 Copyright © 2012 by ASME Journal of Solar Energy Engineering, vol. 125, p. 488, 2003.

24 Fuglsang, P. and Bak, C., "Development of the Risø Wind Turbine Airfoils," Wind Energy, vol. 7, no. 2, pp. 145-162, Apr. 2004.

25 Arndt, R. E. A., "Cavitation in Fluid Machinery and Hydraulic Structures," *Annual Review of Fluid Mechanics*, vol. 13, pp. 273-328, 1981.

26 Blake, W. K. and David, D. C., *Aero-Hydroacoustics for Ships*. Bethesda, MD: David W. Taylor Naval Ship Research and Development Center, 1984.

27 Carlton, J., *Marine Propellers and Propulsion*. Oxford: Butterworth-Heinemann, 1994.

28 Heskestad, G. and Olberts, D. R., "Influence of Trailing-Edge Geometry on Hydraulic-Turbine-Blade Vibration Resulting from Vortex Excitation," *American Society of Mechanical Engineers -- Transactions -- Journal of Engineering for Power Series A*, vol. 82, no. 1, pp. 103-110, 1960.

29 Drela, M., "XFOIL: An Analysis and Design System for Low Reynolds Number Airfoils," presented at the Conference on Low Reynolds Number Airfoil Aerodynamics, University of Notre Dame, 1989.

30 Buning, P. G., Jesperson, D. C., Pulliam, T. H. and et. al., "OVERFLOW User's Manual, Version 1.8aa." NASA Langley Research Center, Apr-2003.

31 Shiu, H., van Dam, C. P., Johnson, E., Barone, M., Phillips, R., Straka, W., Fontaine, A., and Jonson, M., 2012, "A Design of a Hydrofoil Family for Current-Driven Marine-Hydrokinetic Turbines," *Proceedings of the 20th International Conference on Nuclear Engineering and ASME 2012 Power Conference*, July 30 – August 3, Anaheim, CA, USA.

32 Phillips, R. S., 2012, "Cavitation Assessment and Hydrodynamic Performance Characteristics of a Marine Hydrokinetic Turbine Foil Design, M.S. Thesis, The Pennsylvania State University.

33 Jonson, M. L. and Eaton, J. E., 2011, "Turbine Trailing Edge Specification for Marine Hydrokinetic Devices," Penn State University Applied Research Laboratory TR 11-001.

34 Standish, K. J. and van Dam C. P. 2003, "Aerodynamic Analysis of Blunt Trailing Edge Airfoils," *Journal of Solar Energy Engineering*, 125(4), pp. 479-487.

35 Barone, M., "Preliminary Design of a Reference Marine Hydrokinetic Turbine," Sandia National Laboratories, internal report, May 2010.

36 Abbott, I. H., **Theory of Wing Sections, Including a Summary of Airfoil Data**, [Corr. version. New York: Dover Publications, 1959.

37 Wortmann, F. X., "A Critical Review of the Physical Aspects of a Airfoil Design at Low Mach Number," in *Motorless Flight Research, 1972*, 1973, vol. 2315.

38 Eppler, R., *Airfoil Design and Data*. Berlin; New York: Springer-Verlag, 1990.

39 van Rooij, R. P. J. O. M. and Timmer, W. A., "Roughness Sensitivity Considerations for Thick Rotor Blade Airfoils," *Journal of Solar Energy Engineering*, vol. 125, no. 4, pp. 468-478, Nov. 2003.

40 Kermeen, R. W., "Water Tunnel Tests of NACA 4412 and Walchner Profile 7 Hydrofoils in Noncavitating and Cavitating Flows," online at http://resolver.caltech.edu/CaltechAUTHORS:KERhydrolabrpt47-5, accessed Mar. 2012, Feb. 1956.

41 Knapp, R. T., "Force and Cavitation Characteristics of the NACA 4412 Hydrofoil," online at http://resolver.caltech.edu/CaltechAUTHORS:KNAhydrolabrptND-19, accessed Mar. 2012, Jun. 1944.

42 Standish, K. J. and van Dam, C. P., "Aerodynamic Analysis of Blunt Trailing Edge Airfoils," *Journal of Solar Energy Engineering*, vol. 125, no. 4, pp. 479-487, Nov. 2003.

43 Baker, J. P. Mayda, E. A. and van Dam, C. P., "Experimental Analysis of Thick Blunt Trailing-Edge Wind Turbine Airfoils," *Journal of Solar Energy Engineering*, vol. 128, no. 4, pp. 422-431, Nov. 2006.

44 Chow, R. and van Dam, C. P., "Computational Investigations of Blunt Trailing Edge and Twist Modifications to the Inboard Region of the NREL 5 MW Rotor," *Wind Energy*, in print, 2012.

45 Grasso, F., "Development of Thick Airfoils for Wind Turbines," presented at the 50th AIAA Aerospace Sciences Meeting, Nashville, TN, 2012.

46 Burton, T., Sharpe, D., Jenkins, N., Bossanyi, E., 2001, "Wind Energy Handbook," *John Wiley & Sons*, Hoboken, NJ, USA, pp. 60, 86-87.

47 A. A. Fontaine, J. T. Ellis, T. M. Healy, J. Hopmeyer, and A. P. Yoganathan, "Identification of Peak Stresses in Cardiac Prostheses: A Comparison of Two-Dimensional versus Three-Dimensional Principal Stress Analyses," *American Society Artificial Internal Organs Journal* 42:154-163, 1996.

48 Petrie, H.L., Samimy, M. and Addy, A.L., "Laser Doppler velocity bias in separated turbulent flows," Exp. Fluids, Volume 6, Issue 2, pp 80-88, 1988.

49 Edwards, R. V.; Jensen, A. S. "Particle sampling statistics in laser anemometers: sample-and-hold systems and saturable systems," J. Fluid Mech. 133, 397–411, 1983.

50 Benedict, L.H., Nobach, H. and Tropea, C., "Estimation of turbulent velocity spectra from laser Doppler data," *Meas. Sci. & Tech.*, 11, 1089-1104, 2000.

51 TSI Inc. WWW.TSI.COM.

52 Fontaine,A. A., Ellis, J. T. Healy, T. M. Hopmeyer, J. and Yoganathan, A. P. "Identification of Peak Stresses in Cardiac Prostheses: A Comparison of Two-Dimensional versus Three-Dimensional Principal Stress Analyses," *American Society Artificial Internal Organs Journal* 42:154-163, 1996.

53 Coleman, H. W. and Steele, W. G., 1989, *Experimentation and Uncertainty Analysis for Engineers*, Published by J. Wiley and Sons, Inc.

54 Guide to the Expression of Uncertainty in Meas. (GUM), 2004, ISO GUM Suppl 1.

55 ITTC Recommended Procedures and Guidelines, "Testing and Extrapolation Methods, General Uncertainty Analysis in EFD Uncertainty Assessment Methodology," 7.5-02-01-01, www.ittc.sname.org, 1999.

56 Benedict, L. H. and Gould, R. D., 1996, "Towards Better Uncertainty Estimates for Turbulence Statistics," *Exp. Fluids*, 22, pp 129-136.

57 Garcia, C.M., Jackson, P.R., and M.H. Garcia, "Confidence intervals in the determination of turbulence parameters," *Experiments in Fluids*, 40, 514-522, 2006.

58 ITTC Recommended Procedures and Guidelines, "Uncertainty Analysis Particle Image Velocimetry," 7.5-01-03-03, www.ittc.sname.org, 2008.

59 Atsavapranee, P, Day, A., Felli, M, Fontaine, A.A., Kawamura, T., Perelman, O., Sampson, R., and Zhao, F., "The Specialist Committee on Detailed Flow Measurements: Final Report and Recommendations to the 26th ITTC," Proc. of the 26th ITTC, Brazil, 2011.

60 Foucaut, J. M., Miliat, B., Perenne, N., and Stanislas, M., 2003, "Characterization of Different PIV Algorithms using the EUROPIV Synthetic Image Generator and Real Images From a Turbulent Boundary Layer," EUROPIV 2 Workshop, Zaragosa, Spain

61 Raffel, M., Willert, C. E., Kompenhans, J., "Particle Image Velocimetry: A Practical Guide," Springer Verlag, 1998.

62 Gui L. and Wereley, S. T., 2002, "A correlation based continuous window shift technique to reduce peak locking effect on digital image evaluation, Exp. Fluids, Vol. 32, pp. 506-517.

63 LaVision, Inc.

64 Grizzi, S., Pereira, F., and Di Felice, F., 2010, "A Simplified, Flow-Based Calibration Method for Stereoscopic PIV," Exp Fluids, Vol. 48, pp. 473-486.

65 Prasad, A. K. and Adrian, R. J., 1993, "Stereoscopic Particle Image Velocimetry Applied to Liquid Flows," Exp. Fluids, Vol. 15, pp. 49-60.

66 Prasad, K., 2000, "Stereoscopic Particle Image Velocimetry," Exp. Fluids, Vol. 29, pp. 103-116.

67 Lawson, N. and Wu, J., 1997a, "Three-Dimensional Particle Image Velocimetry: Error Analysis of Stereoscopic Techniques," Meas. Sci. Tech., Vol. 8, pp. 894-900.

68 Lawson, N. and Wu, J., 1997b, "Three-Dimensional Particle Image Velocimetry: Experimental Error Analysis of a Digital Angular Stereoscopic System," Meas. Sci. Tech., Vol. 8, pp. 1455-1464.

69 Elbing, B. R., Petrie, H.L., and Fontaine, A. A., 2001, "Articial Shifting of Stereo PIV Images for Uncertainty Estimation," Manuscript in process.

Distribution List (detached from report)

Distribution List for ARL Penn State Technical Report 13-002 entitled "A 1:8.7 Scale Water Tunnel Verification & Validation Test of an Axial Flow Water Turbine," by A. A. Fontaine, W. A. Straka, R. S. Meyer, and M. L. Jonson dated 1 August 2013.

Sandia National Laboratories
PO 5800
Albuquerque, NM 87185-0825
Attn: Matthew F. Barone

Sandia National Laboratories
PO 5800
Albuquerque, NM 87185-1124
Attn: Chris C. Chartrand

Sandia National Laboratories
PO 5800
Albuquerque, NM 87185-1124
Attn: Ryan G. Coe

Sandia National Laboratories
PO 5800
Albuquerque, NM 87185-1124
Attn: Budi Gunawan

Sandia National Laboratories
PO 5800
Albuquerque, NM 87185-1124
Attn: Daniel L. Laird

Sandia National Laboratories
PO 5800
Albuquerque, NM 87185-1124
Attn: Carlos Michelen

Sandia National Laboratories
PO 5800
Albuquerque, NM 87185-1124
Attn: Vincent S. Neary

Applied Research Laboratory
The Pennsylvania State University
PO Box 30
State College, PA 16804-0030
Attn: Arnold A. Fontaine

Applied Research Laboratory
The Pennsylvania State University
PO Box 30
State College, PA 16804-0030
Attn: William A. Straka

Applied Research Laboratory
The Pennsylvania State University
PO Box 30
State College, PA 16804-0030
Attn: Richard S. Meyer

Applied Research Laboratory
The Pennsylvania State University
PO Box 30
State College, PA 16804-0030
Attn: Michael L. Jonson